High-resolution optical analyses of IP_3-evoked Ca^{2+} signals

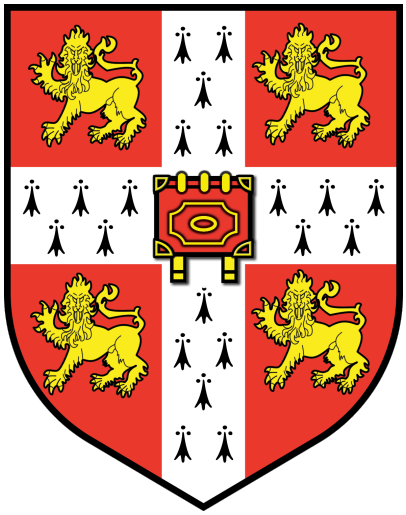

Stefania Mataragka

Department of Pharmacology

University of Cambridge

Wolfson College

A dissertation submitted for the degree of

Doctor of Philosophy

September 2018

Preface

The work presented in this dissertation was performed, unless otherwise stated, solely by the author in the Department of Pharmacology, University of Cambridge between October 2015 and September 2018. This thesis does not exceed the word limit approved by the Biology Degree Committee and is not substantially the same as any other that has been submitted for a degree, diploma or other qualification at any establishment.

Στην πολυαγαπημένη μου μαμσίτα.

Acknowledgments

My greatest thanks go to my supervisor, Prof. Colin W. Taylor, for his continuous encouragement and excellent support during my years in Cambridge. Under his guidance I was able to bring my research project to fruition. I would also like to thank my colleague, Dr Babu Thillaiappan, for his eagerness to discuss many aspects of my project and for his unwavering help and support. I wish to thank Peace Atakpa, Dr Vera Konieczny, Dr Margit Muller and Dr Raul Lagos Cabre, for their advice and friendship. I would like to extend my thanks to everyone in the lab for creating a welcoming and stimulating environment. I would also like to thank the Biotechnology and Biological Sciences Research Council (BBSRC) for funding my studies. Last but not least, I would like to thank my family (Mrs. Ioulia Kampani, Mr. Theodoros Mataragkas, Mrs. Eleni Kampani and Mrs. Melek Mataragka) for their unconditional love and support and my partner Mr. Vangelis Pappas.

Publications

Mataragka S & Taylor CW (2018) All three IP_3 receptor subtypes generate Ca^{2+} puffs, the universal building blocks of IP_3-evoked Ca^{2+} signals. J Cell Sci 131(16)

Atakpa P, Thillaiappan NB, Mataragka S, Prole DL, & Taylor CW (2018) IP_3 Receptors Preferentially Associate with ER-Lysosome Contact Sites and Selectively Deliver Ca^{2+} to Lysosomes. Cell Rep 25(11):3180-3193 e3187.

Abstract

Ca^{2+} is a universal intracellular messenger that regulates many cellular responses. Most cells express inositol 1,4,5-trisphosphate receptors (IP_3R) that mediate Ca^{2+} release from the endoplasmic reticulum (ER) when they bind IP_3 produced after activation of cell-surface receptors. Vertebrate genomes encode three closely related subtypes of IP_3R (IP_3R1-3). High-resolution optical analyses have revealed a hierarchy of IP_3-evoked Ca^{2+} signals that are thought to arise from the co-regulation of IP_3Rs by IP_3 and Ca^{2+}. The smallest events ('blips') report the opening of single IP_3Rs, Ca^{2+} 'puffs' report the almost simultaneous opening of a few clustered IP_3Rs, and as stimulus intensities increase further Ca^{2+} signals propagate regeneratively as Ca^{2+} waves. The aim of this study was to establish whether all three IP_3R subtypes can generate Ca^{2+} puffs.

I first used a haploid cell line (HAP1 cells) to generate, using CRISPR/Cas9, a line lacking all endogenous IP_3Rs. However, for analyses of Ca^{2+} puffs, I used HEK cells that had been engineered, using CRISPR/Cas9 to disrupt endogenous genes, to express single IP_3R subtypes. Local Ca^{2+} signals evoked by flash-photolysis of caged-IP_3 were recorded using Cal520 and total internal reflection fluorescence (TIRF) microscopy in human embryonic kidney (HEK) cells. The Flika algorithm was used, and validated, for automated detection of Ca^{2+} puffs and to measure their properties.

IP_3 evoked Ca^{2+} puffs in wild-type HEK cells and in cells expressing single IP_3R subtypes. In wild-type cells, the Ca^{2+} signals invariably propagated regeneratively to give global increases in cytosolic [Ca^{2+}]. This occurred less frequently in cells expressing single IP_3R subtypes, commensurate with their lower overall levels of IP_3R expression. The properties of the Ca^{2+} puffs, including their rise and decay times, durations, the size of the unitary fluorescence steps as channels closed channel during the falling phase, and the estimated number of active IP_3Rs in each Ca^{2+} puff, were broadly similar in each of the four cell lines. The latter observation suggests that despite lower overall levels of IP_3R expression (~30%) in cells with single subtypes relative to WT cells, there is a mechanism that ensures formation of similarly sized IP_3R clusters. The only significant differences between cell lines were the slower kinetics of the Ca^{2+} puffs evoked by IP_3R2,

which may suggest dissociation of IP_3 from its receptor contributes to the termination of Ca^{2+} puffs.

My results demonstrate, for the first time, that all three IP_3R subtypes can generate Ca^{2+} puffs. I conclude that Ca^{2+} puffs are fundamental building blocks of all IP_3-evoked Ca^{2+} signals.

Table of Contents

Abbreviations

2-APB	2-aminoethoxydiphenyl borate
2D	2-dimensional
ACh	Acetylcholine
AM	Acetoxymethyl ester
ARC	Arachidonic acid-regulated Ca^{2+} channels
ARM	Armadillo solenoid fold
ATP	Adenosine triphosphate
BAPTA	1,2-Bis(O-aminophenoxy)ethane-N,N,N',N'-tetraacetic acid
bp	Base pair
BSA	Bovine serum albumin
$[Ca^{2+}]$	Ca^{2+} concentration
$[Ca^{2+}]_c$	Cytosolic free Ca^{2+} concentration
CaMKII	Ca^{2+}-CaM-dependent protein kinase II
Cas	CRISPR-associated genes
CCh	Carbachol
CICR	Ca^{2+}-induced Ca^{2+} release
CLM	Cytosol-like medium
CPA	Cyclopiazonic acid
CRISPR	Clustered regularly interspaced short palindromic repeats
CRISPRi	CRISPR interference
crRNA	Non-coding CRISPR RNA
cryo-EM	Single-particle electron cryomicroscopy
DAG	Diacylglycerol
dCas9	Nuclease-deficient Cas9
DMNB	4,5-Dimethoxy-2-nitrobenzyl
DMSO	Dimethyl sulfoxide
DSB	Double-stranded break
DTT	Dithiothreitol
E-C	Excitation-contraction
EDTA	Ethylenediaminetetraacetic acid
EGTA	Ethylene glycol-bis(β-aminoethyl ether)-N,N,N',N'-tetraacetic acid
ER	Endoplasmic reticulum
ET-1	Endothelin-1

F	Fluorescence
F/F_0	Fluorescence divided by F_0
F_0	Resting fluorescence
FBS	Foetal bovine serum
F_{max}	Maximal fluorescence signals
F_{min}	Minimal fluorescence signals
FRAP	Fluorescence recovery after photobleaching
GDP	Guanosine 5'-diphosphate
GFP	Green fluorescent protein
GPCR	G-protein coupled receptor
GTP	Guanosine 5'-triphosphate
HBS	HEPES-buffered saline
HD	α-helical domain
HDR	Homology directed repair
HEK	Human embryonic kidney
HEK 3-KO	HEK293 cells devoid of IP_3R1/ IP_3R2/ IP_3R3 expression
HNH	Histidine-asparagine-histidine
HRP	Horseradish peroxidase
IBC	IP_3-binding domain
ILD	Intervening lateral domain
IP_3	Inositol 1,4,5-trisphosphate
IP_3R	Inositol 1,4,5-trisphosphate receptor
KO	Knock out
LNK	helical linker domain
MCU	Mitochondrial Ca^{2+} uniporter
NCX	Na^+/Ca^{2+} exchanger
NHEJ	Non-homologous end joining
ORF	Open reading frame
PAM	Protospacer adjacent motif
PBS	Phosphate-buffered saline
PCR	Polymerase chain reaction
PIP_2	Phosphatidylinositol 4,5-bisphosphate
PLC	Phospholipase C
PM	Plasma membrane

PMCA	Plasma membrane Ca^{2+} ATPase
RFU	Relative fluorescence units
ROC	Receptor-operated channel
ROI	Region of interest
RT-PCR	Reverse transcription polymerase chain reaction
RYR	Ryanodine receptor
SAC	Stretch-activated channel
SERCA	Sarco-endoplasmic reticulum ATPase
sgRNA	Single guide RNA
SMOC	Second messenger-operated channel
SOC	Store-operated channel
SOCE	Store-operated Ca^{2+} entry
STIM	Stromal interaction molecule
TALEN	Transcription activator-like effector nuclease
TBS	Tris-buffered saline
TMD	Transmembrane domain
TIRF	Total internal reflection fluorescence
TIRFM	Total internal reflection fluorescence microscopy
tracrRNA	Trans-activating crRNA
TRPC	Canonical transient receptor potential channels
VOC	Voltage-operated channel
ZFN	Zinc finger nucleases
β-TF	β-trefoil domain

Chapter 1: Introduction

1.1 Overview of Ca^{2+} signalling

1.1.1 Basic principles of Ca^{2+} signalling

Ca^{2+} is a universal intracellular messenger that binds to proteins (e.g. calmodulin) and regulates a plethora of cellular responses including development, fertilization, cell proliferation, transcription, contraction, secretion, learning and memory and apoptosis (Clapham, 1995, Berridge et al., 2000). How can one single intracellular messenger mediate so many responses and yet maintain specificity? The regulation of all these biological functions is due to the versatility of the signalling mechanism. Generally, Ca^{2+} signals are local changes in Ca^{2+} concentration ($[Ca^{2+}]$) that persist around the mouths of open channels, due to the presence of Ca^{2+} buffers, which slow the diffusion of Ca^{2+} in the cytoplasm (Clapham, 1995). The $[Ca^{2+}]$ near the mouth of an open channel can be as high as hundreds of micromolar (Shuai and Parker, 2005, Parekh, 2008), and can quickly dissipate within nanometer distances. The downstream effectors that bind Ca^{2+} such as Ca^{2+}-CaM-dependent protein kinase II (CaMKII) are often located close to the channel (Wu et al., 2006). Therefore, the position of Ca^{2+} release channels, the intrinsic properties of the channel and the amplitude, speed and spatiotemporal patterning of the signal are important for shaping cellular responses (Berridge et al., 2000).

1.1.2 Mechanisms of Ca^{2+} transport

The cytosolic free Ca^{2+} concentration ($[Ca^{2+}]_c$) is low (100nM) and activation of cells leads to an increase in $[Ca^{2+}]_c$ up to ~1000nM measured globally, which is necessary to initiate downstream functions (Berridge et al., 2000). Changes in $[Ca^{2+}]_c$ are mediated by either channels or pumps expressed in the endoplasmic reticulum (ER) (free $[Ca^{2+}]$ ~ 100μM) (Solovyova and Verkhratsky, 2002) or the plasma membrane (PM). Once Ca^{2+} has carried out its signalling activity, it is rapidly extruded from the cytoplasm by various pumps and exchangers to restore resting conditions (Pozzan et al., 1994, Blaustein and Lederer, 1999). This is an essential step for fine-tuning intracellular Ca^{2+} homeostasis, as prolonged high

$[Ca^{2+}]_c$ in the cytoplasm can have toxic effects and lead to apoptosis (Clapham, 2007). The most important extrusion mechanisms are the plasma membrane Ca^{2+} ATPase (PMCA) and the Na^+/Ca^{2+} exchanger (NCX). PMCA is powered to actively extrude Ca^{2+} into the extracellular space by the hydrolysis of adenosine triphosphate (ATP) (Carafoli, 1991). NCX uses the electrochemical gradient of Na^+ across the PM to remove Ca^{2+} from the cytoplasm. During each NCX cycle, three Na^+ ions enter the cell and one Ca^{2+} ion is removed from the cell against its concentration gradient (Brini and Carafoli, 2011). Ca^{2+} uptake back into the intracellular Ca^{2+} stores is mediated via sarco-endoplasmic reticulum ATPases (SERCA) (Pozzan et al., 1994). Organelles such as lysosomes (Christensen et al., 2002), mitochondria via the mitochondrial Ca^{2+} uniporter (MCU) (Baughman et al., 2011, Kamer and Mootha, 2015) and the Golgi apparatus (Dolman and Tepikin, 2006) are able to rapidly sequester Ca^{2+} during the Ca^{2+} signal and release it during the recovery phase.

Ca^{2+} can be introduced into the cytoplasm for signal transduction from either of the two largest Ca^{2+} pools, the ER or the extracellular space (Clapham, 1995). Different families of Ca^{2+} channels mediate uptake of Ca^{2+} from the extracellular space and are classified based on their mode of activation. The first family of Ca^{2+} channels are stretch-activated channels (SACs), which open in response to mechanical deformation (Sackin, 1995). The second family of Ca^{2+} channels are voltage-operated channels (VOCs). They are found in excitable cells and are activated in response to membrane depolarisation. Once activated, VOCs can mediate the release of neurotransmitters or induce muscle contraction (Catterall, 2011). VOCs are the fastest Ca^{2+} channels and can conduct approximately a million Ca^{2+} ions every second (Clapham, 2007). L-type Ca^{2+} channels belong to the VOC family; they are highly expressed in striated muscle and mediate muscle contraction (Striessnig et al., 2014). Another family of Ca^{2+} channels are receptor-operated channels (ROCs), which are mostly expressed on secretory cells and at synapses (Bootman et al., 2001). ROCs activation occurs in response to agonist binding on their extracellular domain (Bootman et al., 2001). An example of a ROC is the P2X receptor which is activated in response to ATP (Bootman et al., 2001). Another family of Ca^{2+} channels are second messenger-operated Ca^{2+} channels (SMOCs). SMOCs open upon binding of an intracellular messenger to

their cytosolic site. Typical examples of SMOCs are canonical transient receptor potential channels (TRPC), some of which are activated by diacylglycerol (DAG) (Gees et al., 2012); and arachidonic acid-regulated Ca^{2+} channels (ARC), which are activated by arachidonic acid (Thompson and Shuttleworth, 2013). The last family of Ca^{2+} channels are store-operated channels (SOCs). In response to loss of Ca^{2+} from the ER, SOCs can mediate the uptake of Ca^{2+} from the extracellular space, a process known as store-operated Ca^{2+} entry (SOCE). The most important components of SOCE are the stromal interaction molecules (STIM1 and STIM2) and the PM channel Orai1 (Liou et al., 2005, Roos et al., 2005). STIM1 is a Ca^{2+}-sensor that resides within the ER membrane. When Ca^{2+} is lost from its luminal EF-hands, STIM1 oligomerises and diffuses within the ER membrane to activate PM Orai channels in ER-PM junctions. The C-terminal cytosolic domain of oligomerised STIM1 allows it to bind directly to Orai1, the subunit that forms the Ca^{2+}-permeable channel, leading to channel gating and Ca^{2+}-entry (Wang et al., 2014, Prakriya and Lewis, 2015).

1.1.3 Ca^{2+} release from intracellular stores

The major family of Ca^{2+} channels expressed in the ER are inositol trisphosphate receptors (IP_3R) (Foskett et al., 2007), which mediate Ca^{2+} release in response to inositol trisphosphate (IP_3) binding (Berridge and Irvine, 1984). The generation of IP_3 is catalysed by phospholipase C (PLC), which hydrolyses the membrane lipid, phosphatidylinositol 4,5-bisphosphate (PIP_2), into IP_3 and DAG (Berridge, 1993, Newton et al., 2016). Many PM receptors can activate PLC, but the most common belong to the family of G-protein-coupled receptors (GPCR). GPCRs are a family of receptors with a characteristic seven transmembrane helix structure. Binding of an appropriate agonist, such as acetylcholine (ACh), to a GPCR catalyses the activation of a G-protein. Activation of a G-protein is achieved by shedding of guanosine diphosphate (GDP) from the Gα subunit and binding of guanosine-5'-triphosphate (GTP) to the same site. This probably allows the dissociation of the G-protein into its constituent subunits, $G\alpha_q$-GTP and Gβγ, which regulate effector systems (Foreman et al., 2011). The β isoforms of PLC can be stimulated by the $G\alpha_q$-GTP subunit of G_q and βγ subunits (Alberts, 2008). IP_3 produced by the hydrolysis of PIP_2 can diffuse through the cytosol and bind

to the N-terminal of the IP_3R, to open the channel and release Ca^{2+} (Seo et al., 2012) **(Figure 1.1)**.

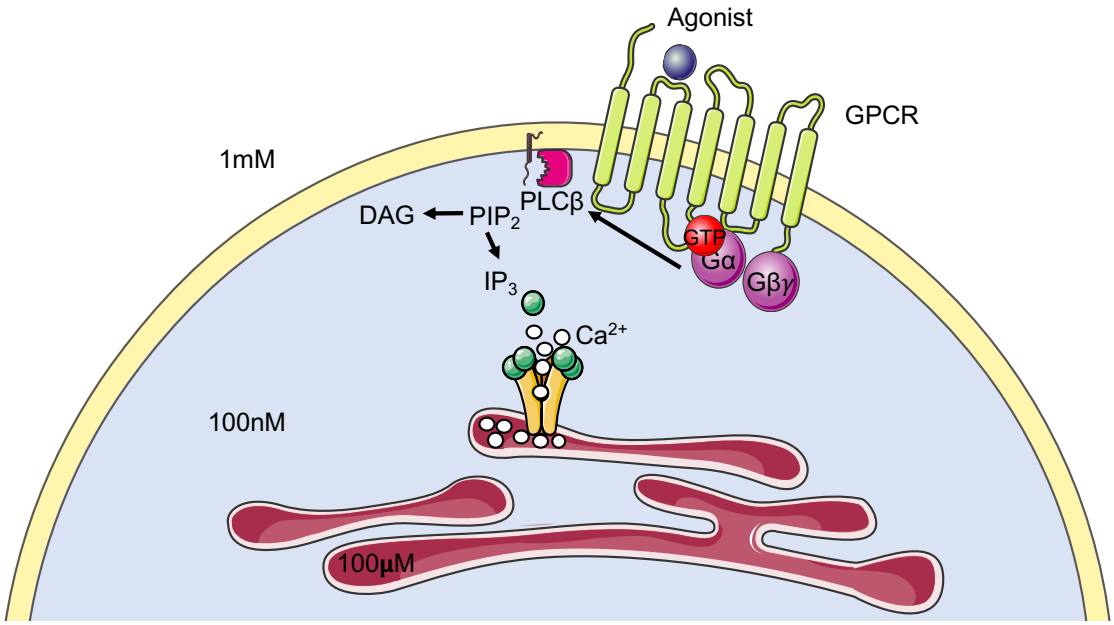

Figure 1.1: IP_3-evoked Ca^{2+} release. Signalling components required for IP_3-evoked Ca^{2+} release initiated by binding of an extracellular agonist to a GPCR.

Opening of IP_3Rs is regulated by both IP_3 and Ca^{2+} (Taylor and Laude, 2002). Binding of IP_3 to the IP_3R primes the channel to respond to Ca^{2+} (Taylor and Tovey, 2012) which can either activate or inhibit IP_3-evoked Ca^{2+} release (Iino, 1990, Taylor and Laude, 2002). Using high-resolution optical techniques, it has been made possible to visualise IP_3-evoked Ca^{2+} signals in intact cells loaded with Ca^{2+} indicators. At low IP_3 concentrations, Ca^{2+} signals arising from a single channel have been identified ('Ca^{2+} blips'). Ca^{2+} blips are short events that last a few milliseconds and are very localised (Parker and Yao, 1996) (**Figure 1.2A**). Opening of the channel will rapidly increase the [Ca^{2+}] near the mouth of the open channel, but will quickly diffuse away. If the IP_3 concentration is higher, Ca^{2+} released from a single channel will be able to activate neighbouring channels in a single IP_3R cluster. The concerted opening of more than one IP_3Rs in a cluster is known as a 'Ca^{2+} puff' (Demuro and Parker, 2004, Parker et al., 1996, Yao et al., 1995, Smith and Parker, 2009, Bootman et al., 1997b) (**Figure 1.2B**), and the process by which Ca^{2+} release from one channel activates a neighbouring channel is known as calcium-induced Ca^{2+}-release (CICR).

Ca^{2+} blips and puffs may act locally or provide the building blocks for larger Ca^{2+} signals. For example, IP_3-evoked Ca^{2+} puffs in astrocytes enable astrocyte-neuronal communication by regulating glutamate exocytosis (Grosche et al., 1999, Berridge, 2006). Additionally, IP_3-evoked Ca^{2+} puffs near the nuclear envelope of ventricular myocytes activate CaMKII, which in turn phosphorylates type II histone deacetylase 5, leading to transcriptional activation (Wu et al., 2006). At even higher stimulation levels, local events become more frequent and activate more IP_3Rs in distant clusters, leading to a Ca^{2+} wave **(Figure 1.2C)** (Parker and Yao, 1991, Sun et al., 1998, Marchant and Parker, 2001, Bootman et al., 1997a). Ca^{2+} waves are long lasting (few seconds) and can be regenerative. As stimulus intensity increases, Ca^{2+} waves become more frequent (Thurley et al., 2011). Ca^{2+} waves carry very specific signalling information as a function of their frequency and amplitude. For example, gene expression in RBL cells is tuned to the frequency of Ca^{2+} oscillations (Li et al., 1998) and the amount of growth hormone released by rat pituitary gonadotrophs depends on Ca^{2+} oscillation frequency (Stojilkovic et al., 1992). Understanding the mechanisms that underlie the recruitment of local and global IP_3-evoked Ca^{2+} signals is an important step towards understanding how extracellular stimuli use Ca^{2+} signals to control cellular activity.

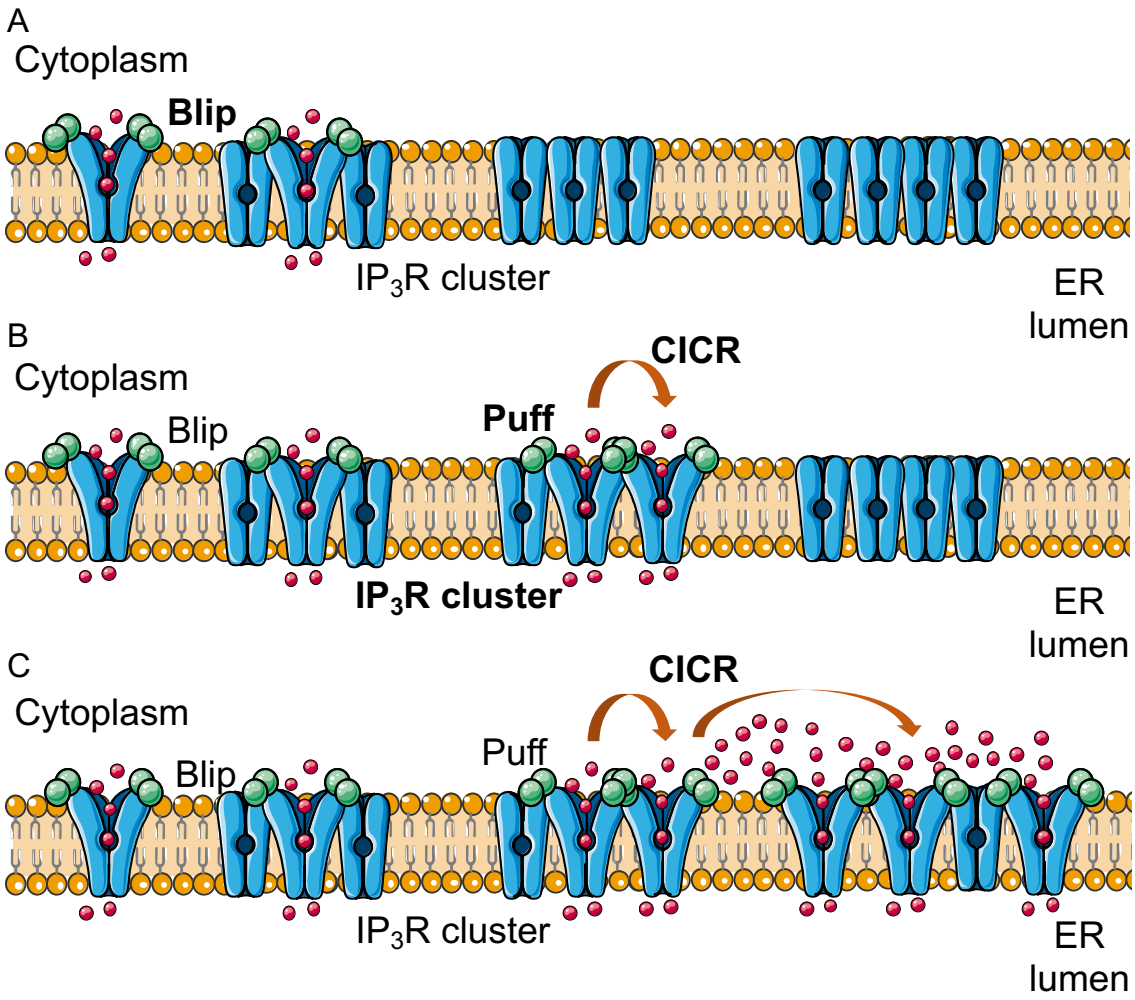

Figure 1.2: Hierarchical organisation of Ca^{2+} signalling. The Ca^{2+} signalling system is hierarchically organised. It comprises local Ca^{2+} signals **(A)** blips and **(B)** puffs that can act locally or as building blocks for global signals such as Ca^{2+} waves **(C)** (Bootman et al., 1997b). IP_3 and Ca^{2+} are shown as green and red spheres, respectively.

Another family of proteins that is closely related to IP_3Rs are ryanodine receptors (RYR) (Foskett et al., 2007). RYRs are expressed in many cell types, but they are the primary Ca^{2+} release channels in striated muscle. RYR1 is highly expressed in skeletal muscle (Fill and Copello, 2002). Membrane depolarisation causes a conformational change in L-type Ca^{2+} channels, which then open RYR1 by physical coupling, leading to muscle contraction (Fill and Copello, 2002). RYR2 is expressed in cardiac muscle and is involved in its excitation-contraction (E-C) coupling. It is activated by Ca^{2+} entering through L-type Ca^{2+} channels (Fill and Copello, 2002). RYR3 is also expressed in striated muscle, but at low levels (Fill and Copello, 2002). Ca^{2+} is the primary activator of all three RYR subtypes (RYR1-3) and their activity can be modulated by caffeine and ATP (Fill and Copello, 2002, Berridge et al., 2000). Similar to Ca^{2+} signals evoked by IP_3Rs, signals mediated by RYRs have a hierarchical structure (Berridge et al., 2000). At low stimulation levels, analogous to Ca^{2+} blips, small Ca^{2+} events occur from a single RYR channel ('quark') (Lipp and Niggli, 1998). At higher stimulus intensity, Ca^{2+} release from a single RYR can activate its immediate neighbours leading to the concerted opening of more than one channels ('spark') (Cheng et al., 1993). At the highest stimulation levels, Ca^{2+} release from a group of RYRs can activate neighbouring RYR clusters leading to a Ca^{2+} wave (Berridge et al., 2000). However, during E-C coupling the near-simultaneous activation of RYRs by membrane depolarisation is primarily responsible for the named biological response. The focus of this thesis is IP_3-mediated Ca^{2+} release so from now on I will only focus on IP_3Rs.

1.2 IP_3R structure

IP_3Rs are ubiquitously expressed in animal cells (Chapter 4) and are mainly localised in the ER to mediate IP_3-evoked Ca^{2+} release (Fujino et al., 1995, Sharp et al., 1999, Patterson et al., 2004, Berridge and Irvine, 1984, Ehrlich and Watras, 1988). There is evidence, however, of IP_3-mediated Ca^{2+} entry from the PM (Dellis et al., 2006) and intracellular organelles such as secretory vesicles (Yoo, 2011), the Golgi (Pinton et al., 1998) and the nucleus (Gerasimenko et al., 1995, Echevarria et al., 2003, Cardenas et al., 2005).

The IP_3R family consists of three genes (*itpr1, itpr2* and *itpr3*) that encode three IP_3R proteins (IP_3R1, IP_3R3 and IP_3R3) (Furuichi et al., 1989, Taylor et al., 1999). The IP_3R protein is large, and consists of approximately 2700 amino acid residues (300kDa). IP_3R diversity is increased by assembly of these monomers into homo- or hetero-tetrameric channels (Maeda et al., 1991, Nucifora et al., 1996, Monkawa et al., 1995) and by alternative splicing (Taylor et al., 2004, Foskett et al., 2007). For example, three different splice variants have been identified for IP_3R1 thus far (SI-III). The diversity of the channel is further increased by the presence of phosphorylation and glycosylation sites which may alter channel conformation (Baker et al., 2017). These combinations create enormous possibilities when the channel is formed. The exact function of different subtypes and whether Ca^{2+} puffs are the elementary building blocks of signals mediated by homotetrameric receptors are not known. The next section will discuss structural similarities shared by the three subtypes, while the distribution and function of each subtype will be covered in Chapter 4.

The IP_3R is a mushroom-shaped integral membrane protein (20nm wide) (**Figure 1.3A**), with 90% of the structure, including the N-and C-terminal regions of the protein, located in the cytosol (Foskett et al., 2007, Fan et al., 2015). Irina Serysheva's group used single-particle electron cryomicroscopy (cryo-EM) to yield a near-atomic resolution structure of IP_3R1 purified from rat cerebellum (Fan et al., 2015) (**Figure 1.3A).** Fan and colleagues proposed that each IP_3R subunit has ten key structural components arranged around a central axis. The N-terminal domain consists of two β-trefoil domains (β-TF; residues 1-436), which includes the β-TF1 domain (also known as the suppressor domain) and part of the IP_3-binding domain (IBC). Absence of the β-TF1 domain does not prevent IP_3-binding, but it abolishes Ca^{2+} release (Uchida et al., 2003). The IBC comprises β-TF2 and part of the first armadillo solenoid fold (ARM). The three ARM domains (ARM1-3; residues 437-2192), including an α-helical domain (HD) that connects ARM1 to ARM2 form the regulatory region of the channel. The ARMs contain binding sites, for posttranslational modifications and IP_3R-binding proteins, that allosterically regulate the channel (Patterson et al., 2004). The amino acid sequence of the three IP_3R subtypes is variable in these regions and may underline differences in properties between the three IP_3R subtypes (Baker et al.,

2017). An intervening lateral domain (ILD; residues 2193-2272) links the ARM domains to the transmembrane domain (TMD; residues 2273-2600). TMD1-4 are proposed to help stabilise heterotetrameric channels (Joseph et al., 1997). TMD5-6 provide the molecular determinants for oligomerisation (Galvan et al., 1999), and interact in a right-handed bundle to form the Ca^{2+}-conducting pore (90% sequence similarity across the three IP_3R subtypes) in the centre of the channel. A helical linker domain (LNK; 2601-2680) links the TMDs to the C-terminus of the channel **(Figure 1.3B** and **C)** (Fan et al., 2015).

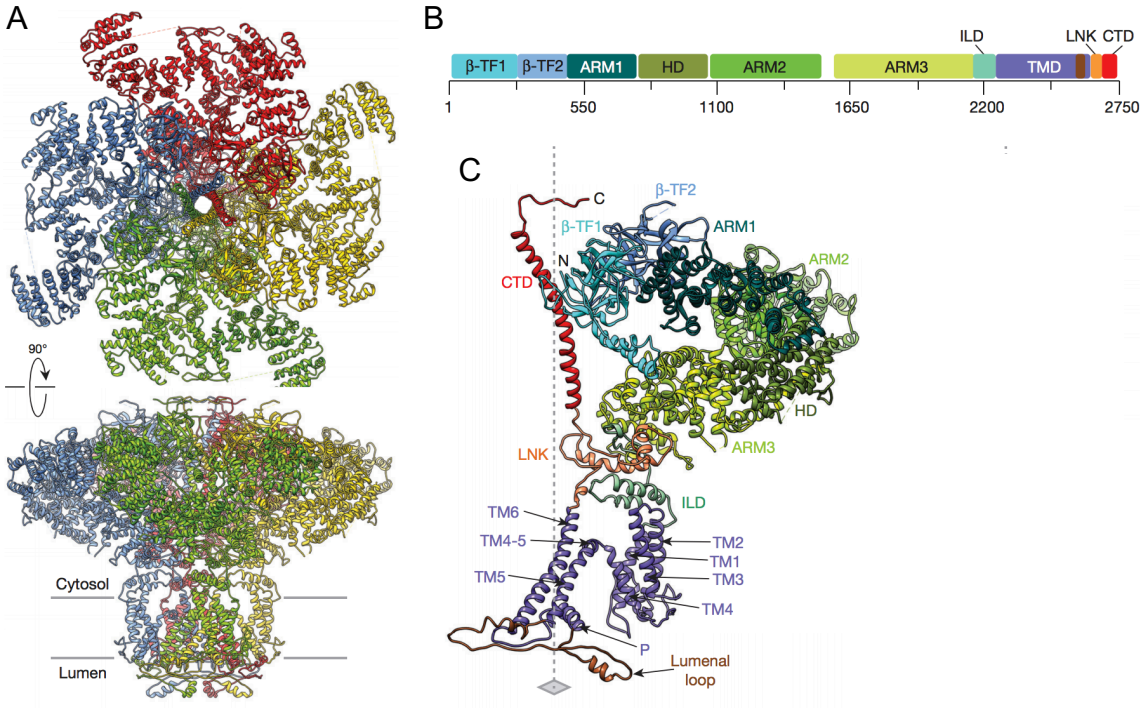

Figure 1.3: Near-atomic resolution of rat IP_3R1. (A) View down the axis from the cytosolic side (top) and membrane view (bottom) of IP_3R1 purified from rat cerebellum. **(B)** Illustrates the key structural domains of an IP_3R1 subunit. **(C)** Individual IP_3R1 subunit. The figure is reproduced from (Fan et al., 2015).

Binding of four IP_3 molecules to the IBCs leads to a conformational change that re-arranges the tetrameric channel, leading to pore opening (Rossi et al., 2009, Seo et al., 2012, Alzayady et al., 2016). Earlier studies suggested that there is a direct association between the IBC and the TMD (Yoshikawa et al., 1999, Boehning and Joseph, 2000). However, based on the structure proposed by Irina

Serysheva's group the distance between the IBC and the Ca^{2+}-conducting pore of the channel is large. It is, therefore, hard to contemplate a direct link between the two domains. Fan and colleagues show that the C-terminal domain sits in close association with the N-terminal domain (**Figure 1.3C**), and they suggest that the C-terminal domain might 'sense' IP_3 binding and transmit it to the TMD. A recent study by Mikoshiba's group suggests that a 21-amino acid sequence ('leaflet'; residues 2195-2215, the ILD in Serysheva's structure) is essential to transmit IP_3-dependent conformational changes. Transfection of IP_3R1 lacking these residues abolished IP_3-evoked Ca^{2+} release in Neuro1a cells, whereas transfection of IP_3R1 lacking the last 50 C-terminal residues increased IP_3-evoked Ca^{2+} release compared to the control (full length IP_3R1). This finding suggests that the C-terminal domain is not essential for channel gating, but may have a regulatory role (Hamada et al., 2017). In addition, they also suggest that IP_3 binding to the channel is communicated to the TMDs in three steps. Firstly, IP_3-binding induces a local conformational change. Secondly, there is a large-scale change in channel conformation and thirdly the leaflet moves to allow Ca^{2+}-release (Hamada et al., 2017). Using cryo-EM, Paknejad and Hite 2018 resolved the structure of human IP_3R3 in the presence and absence of IP_3 (Paknejad and Hite, 2018). In the presence of IP_3, they identified five IP_3R3 conformations. The first conformation includes small conformational changes in the IBC and the other four conformations occur throughout the channel, suggesting that there is a network of interactions between IP_3R3 subunits that mediate gating of the channel (Paknejad and Hite, 2018). These studies provide us with a better understanding of how IP_3-dependent channel gating occurs, but the exact interactions remain elusive.

Opening of IP_3Rs is regulated by both IP_3 and Ca^{2+} (Taylor and Laude, 2002), but the structural basis of Ca^{2+} regulation has not been resolved. There are several Ca^{2+}-binding sites that may be located either within the IP_3R itself or to an IP_3R regulatory protein (Taylor et al., 2004). It has been proposed that there is at least one activating (high affinity) and one inhibitory Ca^{2+} site (low affinity) (Bosanac et al., 2004). The location of the Ca^{2+}-binding sites is unknown. Paknejad and Hite 2018 also investigated the structure of human IP_3R3 in the presence of Ca^{2+} (2mM) (Paknejad and Hite, 2018). They propose the existence

of two Ca^{2+}-binding domains, one located at the interphase between HD and ARM2 (CD Ca^{2+}) and the other located in the cavity formed by ILD and ARM3 (JD Ca^{2+}) (**Figure 1.4**) (Paknejad and Hite, 2018). The JD Ca^{2+} site matches a Ca^{2+}-binding site identified in rabbit RYR (des Georges et al., 2016). By resolving the channel structure in the presence of Ca^{2+} and either low or high IP_3, Paknejad and Hite 2018 show that Ca^{2+} binding occurs independently of IP_3-binding, as both Ca^{2+}-sites are occupied both in the presence of absence of IP_3. They propose that CD Ca^{2+} and JD Ca^{2+} sites stabilise the structure of the channel and separate the cytosolic domains (Paknejad and Hite, 2018).

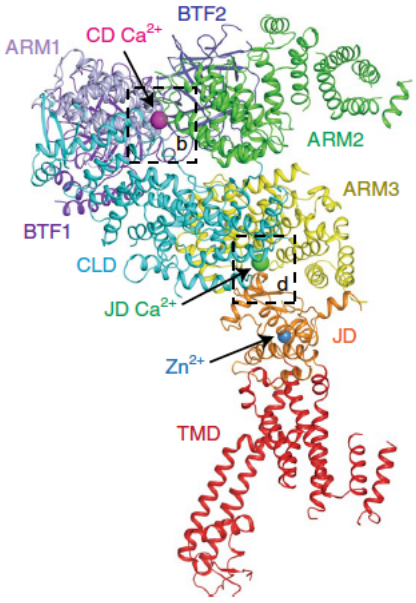

Figure 1.4: Cryo-EM structure of a human IP_3R3 subunit in the presence of 2mM Ca^{2+}. The two proposed Ca^{2+} domains are shown on the IP_3R3 subunit. The ILD domain is abbreviated as JD on this structure. The figure is reproduced from (Paknejad and Hite, 2018).

1.3 High-resolution functional analyses of IP_3Rs

The IP_3R gating mechanism has been investigated in single-channel recordings of IP_3Rs in artificial bilayers and patch-clamp recordings from the nuclear membrane. The use of artificial lipid bilayers provides a means of measuring IP_3R activity by recording currents moving across the lipid bilayer. With this technique, however, IP_3R-binding proteins that may modulate the channel are lost (Foskett et al., 2007). Patch-clamp recordings allow the measurement of currents flowing

through channels with high temporal resolution (Gandini et al., 2014). Most IP_3Rs are expressed in the ER, where patch-recordings are not readily obtainable. A more practicable approach is patch-clamping of IP_3Rs from nuclei isolated from cells (Boehning et al., 2001). While, the native membrane environment is preserved using this technique, the luminal and cytosolic IP_3-binding proteins that regulate channel activity are lost. Findings using single-channel recordings relating to the gating of the three IP_3R subtypes will be described in Chapter 4.

The development of sensitive Ca^{2+} indicators in combination with recent advances in optical techniques have permitted the imaging of Ca^{2+} flux through channel clusters and even through individual channels (Smith et al., 2009a). Ca^{2+} indicators are fluorescent probes that greatly enhance their fluorescence upon binding Ca^{2+} (Lock et al., 2015b) (Chapter 3). Indicators derived from engineered proteins are also widely used, and allow genetically encoded indicators to be directed to specific subcellular locations by targeting sequences (Tong et al., 2012).

The combination of Ca^{2+} indicators with total internal reflection fluorescence microscopy (TIRFM), permits fluorescence recordings from attoliter volumes around open channels (Smith and Parker, 2009). When light passes through two transparent media with different refractive indices, it will be both reflected and diffracted. TIRFM is based on the principle that when light encounters the media at a specific angle (θ) it will be completely reflected. This phenomenon is known as total internal reflection, and creates an electromagnetic wave that decays over short distances (100-200nm). The electromagnetic wave excites only fluorophores close to the interface (Axelrod, 2001). Fluorophores located further from the interface are not excited so the captured images have low background fluorescence and high signal-to-noise ratio. When working with intact cells, TIRFM is effectively restricted to examining the cytosol within 100-200nm of the PM (Mattheyses et al., 2010) (**Figure 1.5**).

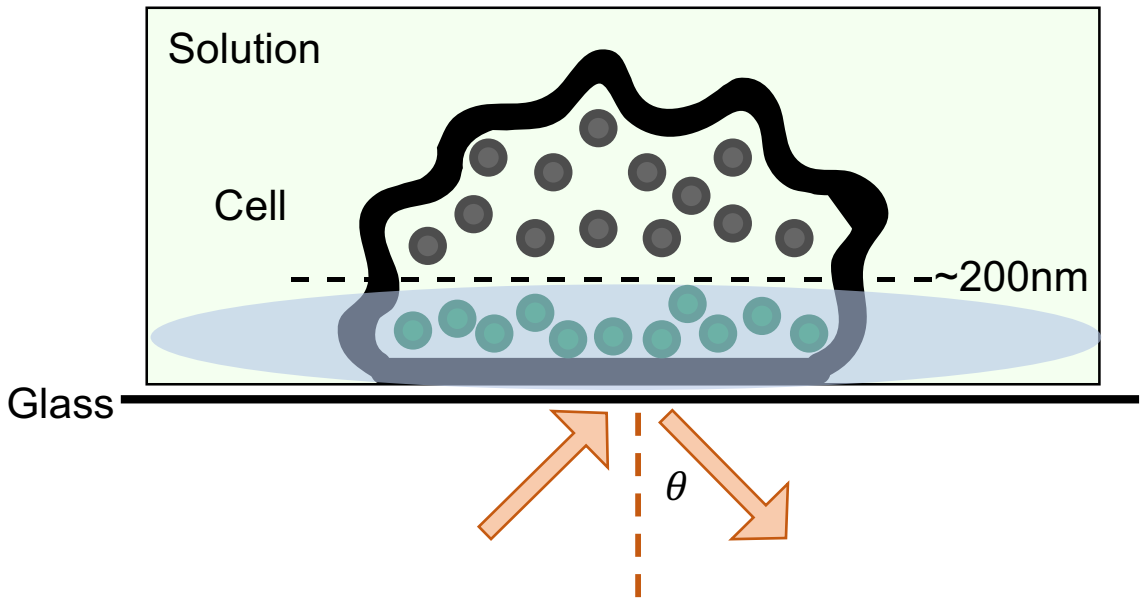

Figure 1.5 Principles of TIRFM. Arrows represent the light path and θ is the critical angle for TIRF to occur. The evanescent wave (blue) excites fluorophores close to the PM (green spots), fluorophores sitting more than ~200nm from the interface are not excited (grey spots). TIRFM can be used to study cellular events close to the PM.

For many applications, including analysis of IP_3-evoked Ca^{2+} signals, these near-PM events are those of most interest (Smith et al., 2009a, Ellefsen and Parker, 2018). By combining TIRFM with fluorescent Ca^{2+} indicators (usually fluo 8 or Cal520) and a Ca^{2+} buffer to restrict the diffusion of Ca^{2+} (EGTA), it has been possible to image the opening of single Ca^{2+} channels located near the PM (Wiltgen et al., 2010). This has been described as 'optical patch-clamping' (Parker and Smith, 2010). The same methods, with flash photolysis of caged IP_3, have been used to examine the openings of single and clustered IP_3Rs. These studies were initially performed by Ian Parker and his colleagues (Smith et al., 2009a), primarily in SH-SY5Y cells. I have used these methods for my analysis of IP_3-evoked Ca^{2+} puffs (Chapters 3 and 4). IP_3-evoked Ca^{2+} puffs will be discussed in Chapter 3.

1.3.1 How are Ca^{2+} puffs terminated?

IP_3 binding to IP_3Rs opens and primes IP_3Rs to respond to Ca^{2+} (Taylor and Laude, 2002). Activation of one channel creates a positive feedback loop of CICR

and propagating Ca^{2+} waves (Taylor and Tovey, 2012). CICR has to be terminated to maintain control of Ca^{2+} signalling and prevent cytotoxicity. What is the mechanism that terminates Ca^{2+} puffs?

Various termination mechanisms have been considered, including inhibition of IP_3Rs by cytosolic Ca^{2+}, regulation of IP_3R gating by Ca^{2+} in the lumen of the ER, or allosteric interactions between channels (Wiltgen et al., 2014). Functional studies using TIRFM that have resolved the gating of individual channels during puffs suggest that channel closings are interdependent (Wiltgen et al., 2014). During these studies, puffs were categorised in five separate groups depending on their shape during the falling phase. One of the groups is defined by the abrupt termination of puffs, namely “square” puffs. The abrupt decrease during the falling phase suggests that multiple channels close simultaneously, supporting the idea that channel closings are not random.

What is the inhibitory signal between IP_3Rs within a cluster? Given that $[Ca^{2+}]_c$ can rise to several tens of micromolar near the mouths of open channels (Shuai and Parker, 2005, Parekh, 2008), it is thought that Ca^{2+}-dependent inhibition might be the common signal that terminates puff “firing” (Ullah et al., 2012). Several theoretical studies support this view (Swillens et al., 1999, Hinch, 2004, Groff and Smith, 2008, Ullah et al., 2012). However, all theoretical studies have a common limitation; namely, the modelling is based on poorly characterised parameters, e.g. spacing of channels, influence of intracellular buffers. If Ca^{2+} inhibition was the cause of puff termination, we would expect high rates of channel closings during the peak of a puff, which would decline when fewer channels are open. This is not the case during “square” puffs where synchronised channel closings are observed. Whether Ca^{2+}-dependent inhibition terminates the explosive positive feedback induced by CICR is unclear.

Ca^{2+} depletion from the ER has also been proposed to play a role during event termination. This could be mediated either by low Ca^{2+} efflux from the ER (not enough to sustain CICR) or through modulation of channel gating by Ca^{2+}-binding sites located in the luminal part of IP_3Rs. The first mechanism tends to be favoured (Fraiman and Dawson, 2004, Foskett et al., 2007). Despite this,

several observations made using “optical patch-clamp“ techniques argue against this (Smith and Parker, 2009, Wiltgen et al., 2014). These include equal magnitude step-wise decreases in fluorescence during the falling phase of a puff, which correspond to closings of individual channels. If a decrease in Ca^{2+} efflux was the termination mechanism, we would expect a decrease in magnitude during individual channel closures. Another observation that argues against this mechanism is the existence of abnormally long puffs, where termination mechanisms seemed to fail. In comparison to “normal” puffs, which last several hundred milliseconds, these puffs showed a sustained Ca^{2+} release for several seconds. This suggests that Ca^{2+} depletion from the ER during the timecourse of “normal” puffs is minimal and not likely to be an important mechanism in puff termination. From all these studies, we can conclude that channel closings are not completely random and that puff termination is to some extent Ca^{2+}-independent. The exact mechanisms of puff termination are still unresolved.

1.3.2 Do active IP_3Rs cluster or are they immobile?

There are still crucial questions concerning the architecture and stability of IP_3R clusters and their diffusional mobility. These are important to resolve as the spatial organisation of IP_3Rs ultimately determines the cellular response (Berridge et al., 2000). Several studies based on nuclear patch-clamp recordings (Rahman and Taylor, 2009, Rahman et al., 2009) and fluorescence recovery after photobleaching (FRAP) propose that IP_3Rs are mobile (Ferreri-Jacobia et al., 2005, Pantazaka and Taylor, 2011). IP_3R1 and IP_3R3 diffuse with a similar diffusion coefficient within the ER membrane. Interestingly, IP_3R2 is less mobile compared to the other two subtypes and displays different mobilities between different subcellular regions (Pantazaka and Taylor, 2011).

Several studies using live cell imaging of IP_3R dynamics or overexpression of tagged IP_3Rs, propose that IP_3Rs cluster in response to IP_3. This phenomenon was first reported by Wojcikiewicz’s group in 1998. The authors used immunostaining techniques before and after stimulation of cell-surface receptors to report the clustering of IP_3Rs in the ER. The experiments were carried out in multiple cell lines and suggested that IP_3R clustering occurs within 10min of

stimulation and persists for 30 to 60min depending on the cell line (Wilson et al., 1998). Mikoshiba's group used live imaging of COS-7 cells overexpressing green fluorescent protein (GFP)-IP_3R1 to show that IP_3R1 is mobile within the ER, and clusters in response to ATP stimulation. Clustering was proposed to be IP_3-dependent as inhibition of PLC abolished GFP-IP_3R1 clustering. Interestingly, however, a more detailed look revealed that IP_3-evoked Ca^{2+} signals occurred within 15s of ATP stimulation, while GFP-IP_3R1 clusters only became apparent after 50s (Tateishi et al., 2005). IP_3-evoked Ca^{2+} signals in endothelial cells overexpressing GFP-IP_3R3 show clustering of IP_3Rs. The peak of IP_3R clustering occurred ~25s after stimulation and persisted for ~75s. Although IP_3R2 clustering was not observed in this study, they suggest that the higher affinity of IP_3R2 for IP_3 mediates clustering of IP_3R2 at basal levels of IP_3 (Geyer et al., 2015). These studies may not, however, reflect the behaviour of native IP_3Rs.

The Taylor lab used patch-clamp recording of nuclear IP_3Rs to suggest that IP_3 caused the clustering of IP_3Rs and to show that clustered IP_3Rs differed from lone IP_3Rs in their sensitivity to IP_3. Native IP_3Rs in the nuclear membrane were shown to be randomly distributed (1μm apart), but in response to IP_3 the distribution of IP_3Rs changed. While the total number of IP_3R remained the same, some patches had an increased number of IP_3Rs and others had none. This suggests that IP_3Rs clustered in response to IP_3 (within 2.5s of stimulation). It was also proposed that IP_3 can retune the sensitivity of IP_3Rs to facilitate the hierarchical recruitment of Ca^{2+} events (Rahman and Taylor, 2009, Rahman et al., 2009). The studies by Rahman and Taylor, however, may not faithfully report the behaviour of IP_3Rs in the mammalian ER since they were conducted in avian nuclei.

Despite these experiments, functional studies report the recruitment of puff sites seconds after IP_3 stimulation (Smith et al., 2009a), which raises the following question: If IP_3R clustering is a dynamic process occurring over tens of seconds, how can we observe puffs within a few seconds (Shuai and Parker, 2005, Smith and Parker, 2009)? As there is no marker to distinguish functional from non-functional IP_3Rs, Ian Parker's group has extensively studied the dynamics of Ca^{2+} signalling indirectly, by analysing the IP_3-evoked Ca^{2+} signals they mediate.

Functional studies show that Ca^{2+}-release sites remain immobile over many minutes (Dargan and Parker, 2003, Smith et al., 2009a, Thomas et al., 1998)

Using TIRFM, Smith et al. monitored the localisation of Ca^{2+} signals after photolysis of caged IP_3. They (Smith et al., 2009b) suggested that if IP_3Rs clustered in response to IP_3, successive Ca^{2+} puffs at a given site would increase in amplitude. They showed that this is not the case, suggesting that there is no IP_3R clustering. In addition, by fitting a 2-dimensional (2D) Gaussian function to fluorescence images of Ca^{2+} blips for the duration of the Ca^{2+} event, they were able to determine their location. They reported that the position of successive Ca^{2+} blips at a particular Ca^{2+} site did not change (<300nm) throughout the recording time (~10s) (Smith et al., 2009b). Thus, they concluded that there is no IP_3-regulated clustering of IP_3Rs in intact cells. Another study by the same group takes advantage of superresolution imaging to precisely localise channel position by monitoring the position of IP_3-evoked Ca^{2+} events. In agreement with (Smith et al., 2009b), they show that ~33% of Ca^{2+} blip sites are immobile and estimate their diffusion coefficient to be less than $0.003\mu m^2s^{-1}$. Similarly to Ca^{2+} blips, they also report that Ca^{2+} puff sites are static (Wiltgen et al., 2010).

So why do Ca^{2+} puff sites appear to be immobile (Smith et al., 2009a, Wiltgen et al., 2010), while IP_3Rs appear to be mobile (Rahman and Taylor, 2009, Pantazaka and Taylor, 2011)? One possibility is that the stimulus (flash photolysis of IP_3) used during functional studies did not sufficiently elevate IP_3 concentration to induce channel clustering, although that seems unlikely. A more plausible explanation could be that the cells contain two different IP_3R populations. One IP_3R subset cytoskeletally anchored together in pre-formed clusters with high sensitivity to IP_3, and a second subset of mobile IP_3Rs that are either functionally unresponsive or only respond to sustained Ca^{2+} elevations (Smith et al., 2009a). Resolving these apparently conflicting lines of evidence would benefit from recording of IP_3-evoked Ca^{2+} signals from cells in which the distribution of native IP_3Rs can be simultaneously monitored.

Another study by the Taylor lab takes advantage of gene-editing technologies (discussed in Chapter 2, but with a focus on CRISPR/Cas9) to

endogenously tag IP_3R1 in HeLa cells with GFP. They show that there are two populations of native IP_3Rs (GFP-tagged IP_3R1). The first population is mobile and diffuses within the ER membrane and the second population of IP_3Rs is immobile. Interestingly, the two different populations of IP_3Rs do not mix. Thillaiappan et al. used TIRFM to record Ca^{2+} signals in HeLa cells with GFP-tagged IP_3R1. They showed that IP_3-evoked Ca^{2+} signals are mediated exclusively by immobile IP_3Rs (Thillaiappan et al., 2017). This study probably resolves the conflicting lines of evidence regarding the clustering of IP_3Rs, but it raises further questions: What is the signal that licenses only a specific subset of IP_3Rs to respond to IP_3? What is the role of functionally-silent IP_3Rs?

1.3.3 Why is it important to have multiple IP_3R subtypes?

Different IP_3R subtypes have been implicated in regulating different cellular responses. Do these differences arise due to the differential distribution of IP_3R subtypes or from fundamental differences in their behaviour? These issues will be discussed in Chapter 4.

1.4 Aims of this study

The aim of my project was to determine whether Ca^{2+} puffs are the universal building blocks of all IP_3-evoked Ca^{2+} signals and to define any differences between the Ca^{2+} signals evoked by IP_3R subtypes (Chapter 4). Towards this aim, I characterised two different mammalian systems in which IP_3Rs were knocked out using gene-editing technologies (Chapter 2) and validated a python based programme (Ellefsen et al., 2014) that allowed me to automate my analysis of IP_3-evoked Ca^{2+} signals (Chapter 3).

Chapter 2: Characterisation of CRISPR-edited HAP1 and HEK cells devoid of IP_3Rs

2.1 Introduction

2.1.1 Cell systems for the study of IP_3Rs

To answer questions regarding the activity of IP_3R channels composed of a single subtype, it is necessary to develop either systems that express a single IP_3R subtype or a 'null background' system in which single IP_3R subtypes can be expressed and characterised. The first approach is better suited to address the contribution of single endogenously expressed IP_3R subtypes in shaping elementary Ca^{2+} signals. The second approach would allow the effects of manipulating the structure and/or expression levels of IP_3Rs on elementary Ca^{2+} signals to be addressed. In mammalian cells, one IP_3R subtype usually predominates, but there are currently no mammalian cell lines endogenously expressing a single IP_3R subtype while being completely devoid of the other two. Hitherto, the only available cells that lack IP_3Rs are avian DT40 cells, in which the genes for all three IP_3R subtypes have been disrupted (Sugawara et al., 1997). These cells have been useful as a 'null background' for expression of mammalian IP_3Rs, but their cytoplasm is restricted to a narrow rim around the nucleus. This makes DT40 cells unsuitable for analyses of elementary Ca^{2+} signals by TIRFM.

2.1.2 Gene-editing technologies

The human genome consists of approximately three billion nucleotides that are organised in chromosomes and reside almost entirely in the nucleus. Each chromosome in the genome may contain hundreds to thousands of genes, with the total number of gene encoding proteins being ~30,000 (Human Genome Project, 2013). Gene-editing technologies allow the introduction of specific point mutations (such as insertions and deletions) or insertion of exogenous DNA sequences. The aim of most gene-editing technologies is to enable the study of cell phenotypes created by the disruption of protein-coding genes (Thurtle-Schmidt and Lo, 2018).

A number of genome-editing technologies have emerged recently, including zinc finger nucleases (ZFN) (Urnov et al., 2010), transcription activator-like effector nucleases (TALEN) (Bedell et al., 2012, Wright et al., 2014) and clustered regularly interspaced short palindromic repeats/Cas systems (CRISPR) (Ran et al., 2013b). The first two technologies involve the tethering of endonuclease catalytic domains to DNA-binding proteins to generate double-stranded breaks (DSB) at specific DNA regions. However, the generation of these proteins for specific DNA targets is expensive and time-consuming (Cai et al., 2016). Unlike the first two gene-editing techniques, CRISPR is solely based on the use of guide RNAs with the ability to guide a nuclease to a specific region in the genome (Ran et al., 2013b). Designing and incorporating guide RNA sequences in an appropriate delivery system, usually a plasmid, is both inexpensive and time-efficient, making CRISPR the most desirable tool for precise gene editing. In contrast to ZFNs and TALENs, an added advantage of CRISPR is that it allows multiplex gene alterations (Cong et al., 2013).

Overall, CRISPR has been described as highly efficient, flexible and specific for the gene editing of multiple cell types and organisms (Ran et al., 2013b). Hitherto, CRISPR/Cas9 has been used for gene editing of mammalian cell lines and numerous organisms in which such experiments were not possible in the past, including animal models such as zebrafish, *Drosophila* and mice (Ceasar et al., 2016), pathogenic prokaryotes such as *Mycobacterium tuberculosis* (Choudhary et al., 2015), yeast such as *Saccharomyces cerevisiae* (Ronda et al., 2015, Jakociunas et al., 2015) and plants such as *Arabidopsis* (Li et al., 2013). Thus, CRISPR/Cas9 can be used to generate mammalian cell lines either expressing single IP_3R subtypes or cell lines devoid of IP_3Rs.

2.1.3 CRISPR is the adaptive immune response of bacteria and archaea

Ishino et al. fortuitously discovered a family of unusual DNA repeats in the *Escherichia coli* genome (Ishino et al., 1987) and Mojica et al. in 2000 detected similar sequences in multiple prokaryote genomes. These sequences were found to be unique in comparison to other repeated motifs in the genome, as they were always organised in clusters and interspaced by sequences of constant length (spacers) (Mojica et al., 2000).

CRISPR/Cas loci are present in ~90% of archaeal genomes and in ~50% of bacterial genomes (Bhaya et al., 2011, Deveau et al., 2010, Horvath and Barrangou, 2010) with *Methanocaldococcus jannaschii* having the record number of 18 different CRISPR loci constituting more than 1% of the genome (Lillestøl et al., 2006). Within a single locus, CRISPR repeat sequences are highly conserved (Jansen et al., 2002, Horvath and Barrangou, 2010), and the number of spacer sequences in a single locus can range from as few as one to several hundred, but most loci contain approximately 50 (Bhaya et al., 2011, Horvath and Barrangou, 2010, Horvath et al., 2009).

The function of CRISPR loci when they were first discovered in *E. coli* and multiple prokaryotes was unclear. The interest in them resurfaced when they were re-discovered in a comparative genomic study of prokaryote strains used in the fermentation industry. The genomic analysis between different strains of *Streptococcus thermophiles*, a prokaryote used in the production of yoghurt and cheese, revealed a highly variable genomic locus (Jansen et al., 2002). The locus containing highly repetitive sequences, interspaced by spacers, was located adjacent to a set of genes (Haft et al., 2005) that were later named CRISPR-associated (*cas*) genes and discovered to have roles in the acquisition of spacer sequences, target interference and expression of non-coding CRISPR RNAs (crRNA) (Thurtle-Schmidt and Lo, 2018). Based on the similarity of the functional domain of Cas proteins to known helicases, nucleases and polymerases, it was originally suggested that the CRISPR locus is involved in chromosomal rearrangement and DNA repair (Makarova et al., 2002).

The observation that spacer sequences matched genomic regions belonging to extrachromosomal elements, such as bacteriophages (Bolotin et al., 2005, Pourcel et al., 2005, Mojica et al., 2005), prompted three independent groups to correctly hypothesise that spacer regions are traces of past invasions that enable immunity against invaders (Bolotin et al., 2005, Pourcel et al., 2005, Mojica et al., 2005), possibly by a mechanism resembling RNA interference (Makarova et al., 2006). The role of spacer sequences in conveying immunity to invading DNA was substantiated later in studies in which spacer content was modified by genetic engineering. Addition of spacers whose sequence matched

protospacers in foreign genomic material led to immunity, and deletion of spacers led to phage susceptibility (Barrangou et al., 2007). These reports were confirmed in mutant *Streptococcus thermophiles* strains, where phage-resistant mutants gained novel spacer sequences matching protospacers in the phage genome (van der Ploeg, 2009). Overall, these studies confirm the hypothesis that bacteria can integrate phage genomic sequences into their CRISPR locus to convey cellular memory of past invaders. The mechanism of spacer selection and its incorporation into the CRISPR locus is still unclear (Bolotin et al., 2005). Considering that it would be costly to microbes to maintain a long array of spacer sequences, they have developed systems to delete old spacer sequences (Horvath et al., 2008, Barrangou et al., 2007).

2.1.4 The type II CRISPR/Cas9 system from *Streptococcus pyogenes*

Several CRISPR/Cas systems have been identified, with each system using different Cas proteins and mechanisms to generate the RNA that guides the nuclease. The type II CRISPR/Cas9 system belonging to *Streptococcus pyogenes* has been adapted for gene editing due to the simplicity of its components. It requires only two RNA components and a single Cas9 protein, SpCas9, which can mediate both the generation of CRISPR RNAs and targeting of the invader's genomic material (Garneau et al., 2010, Thurtle-Schmidt and Lo, 2018).

The type II CRISPR locus from *S. pyogenes* encodes a crRNA array, a trans-activating crRNA (tracrRNA) and other elements such as the SpCas9 nuclease and other Cas proteins. The CRISPR locus is transcribed to generate a long RNA molecule containing alternating repeat sequences interspaced by spacers (crRNA). The tracrRNA, which is transcribed from an upstream locus, hybridises to the crRNA. The double-stranded RNA hybrid matures into multiple crRNA:tracrRNA complexes, each containing a single spacer sequence. SpCas9 then associates with a crRNA:tracrRNA hybrid forming a CRISPR ribonucleoprotein capable of recognising the protospacer sequence preceded by the protospacer adjacent motif (PAM). Different nucleases recognise different PAM motifs, but SpCas9 specifically recognises the 5´–NGG–3´ PAM sequence (where N is any nucleotide) **(Figure 2.1)**.

Arg1333 and Arg1335 in SpCas9 are the two critical arginine residues that interact with the guanine nucleotides on the PAM sequence located on the anti-sense strand (Jinek et al., 2012). This interaction repositions the DNA so that the 5´DNA phosphate on the PAM sequence binds to the phosphate-lock loop in Cas9 to initiate unwinding of DNA (Jinek et al., 2012). This allows Watson-Crick base pair recognition between the protospacer and the guide creating an R loop, where DNA cleavage occurs by SpCas9. The histidine-asparagine-histidine (HNH) domain and the RuvC-like domain on SpCas9 nick the complementary and non-complementary strand, respectively, on the genome (Gasiunas et al., 2012, Jinek et al., 2012). The DSB event occurs 3 base pairs (bp) upstream of the PAM site, resulting in blunt-end cleavage of the DNA (Jinek et al., 2012). Occurrence of the DSB silences viral or phage DNA, making the host resistant to infection **(Figure 2.1 and Figure 2.2A)**.

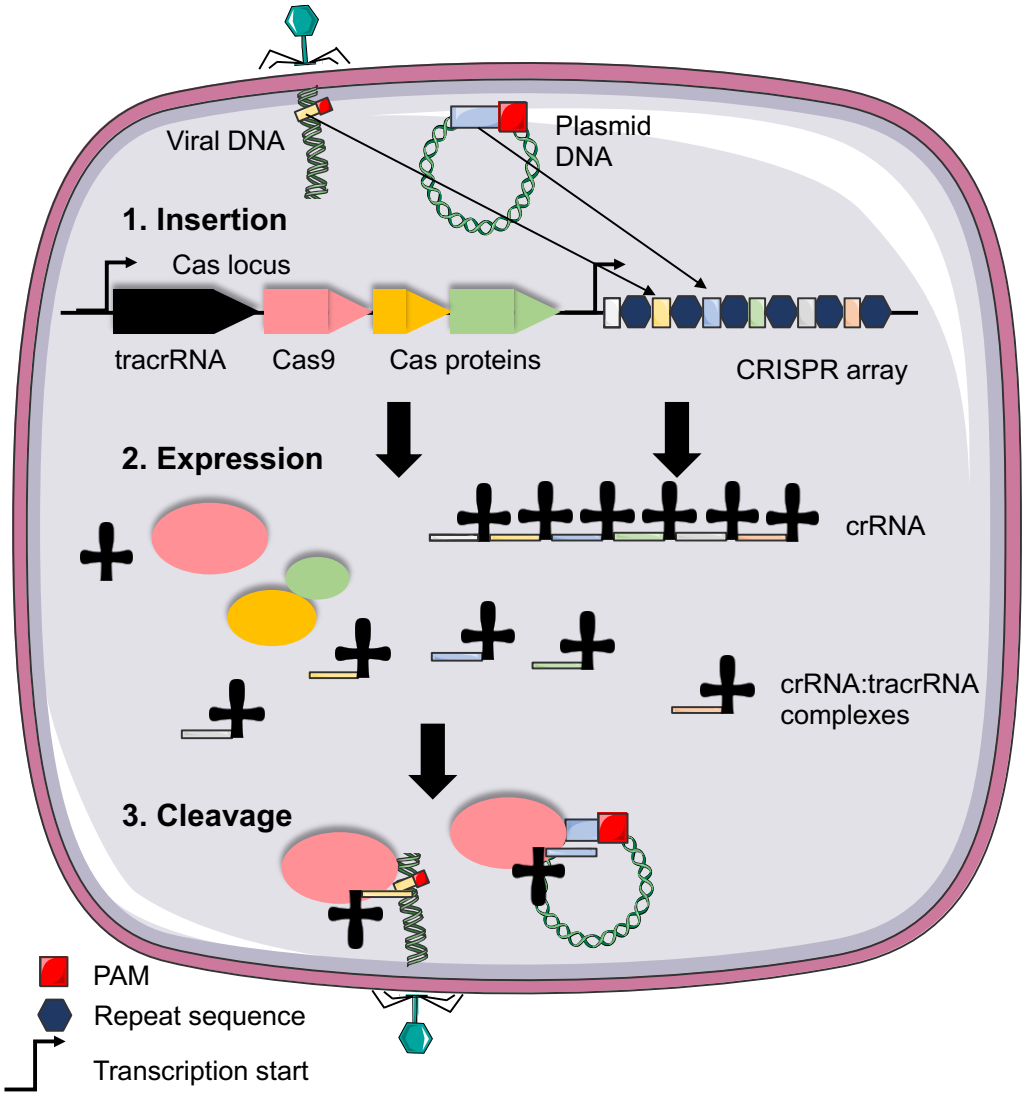

Figure 2.1: Features of the *Streptococcus pyogenes* type II CRISPR/Cas9 system. Stage 1: Spacer insertion into the CRISPR locus. Specific sequences preceded by a PAM motif are identified on the genome of a virus, plasmid or phage and inserted into the leading end of the CRISPR locus. The Cas proteins, tracrRNA and the nuclease, (SpCas9 in *S. pyogenes*), are encoded by the *cas* locus. The CRISPR array consists of a long chain of repeated sequences (dark blue) interspaced by short sequences of a defined length (multicoloured). Stage 2: CRISPR locus expression. crRNA is transcribed from the leading end and cleaved into smaller complexes, and the product then hybridises with tracrRNA (black hairpin structure). Stage 3: The mature complex guides the nuclease to the foreign genetic material. SpCas9 recognises the PAM motif on the target and the nuclease is activated. When the DSB occurs, the foreign DNA is silenced and the host is immune to the invader. The figure was redrawn from Bhaya et al. (2011).

Cleavage of the invading genomic sequence is not initiated if there are mismatches between the spacer sequence and the 3´end of the protospacer in the target sequence, or if there are mutations in the PAM motif (Sternberg et al., 2014). In such cases, the invader's genomic sequence is not silenced and the host is susceptible (Bhaya et al., 2011, Garneau et al., 2010, Deveau et al., 2010, Deveau et al., 2008). Mutations near the 5´end of the protospacer are more tolerated, and despite several mismatches between the guide and the protospacer, cleavage of foreign genomic material may take place (Cong et al., 2013, Jinek et al., 2012, Sapranauskas et al., 2011, Garneau et al., 2010).

2.1.5 Adaptation of the bacterial immune system for precise gene editing

The invention of single guide RNA (sgRNA) by Jinek et al. revolutionised the gene-editing field as the process of programming the nuclease to specific locations in the genome was greatly facilitated (Jinek et al., 2012). To enable easy and specific genome modifications, the engineered sgRNA must have two critical features. At the 5´end, a 20 bp nucleotide target sequence that targets the nuclease to the desired genomic locus, and at the 3´end a double-stranded structure that allows Cas9 binding. These two features create a versatile two-component system that can target any DNA sequence adjacent to a PAM site (Doudna and Charpentier, 2014, Jinek et al., 2012). Hitherto, the RNA-guided Cas9 nuclease from the type II CRISPR/Cas9 system has been proven to be an easily programmable tool that can create a DSB at a specific genomic region (Ran et al., 2013b, Doudna and Charpentier, 2014, Jinek et al., 2013, Cong et al., 2013, Mali et al., 2013) (**Figure 2.2B**).

The cell responds to the DSB by recruiting either of the two DNA repair mechanisms: non-homologous end joining (NHEJ) or homology-directed repair (HDR). In the absence of a repair template, NHEJ is favoured, which usually creates indel mutations in the form of bp insertions or deletions. If these mutations are located within the open reading frame (ORF) of a protein, they can lead to a premature stop codon. Thus, NHEJ can be harnessed to generate gene knock-outs (KO). In the presence of a repair template, HDR may be used as an alternative to NHEJ. This pathway can be harnessed for the generation of precise

modifications such as endogenously tagging a protein (Ran et al., 2013b) (**Figure 2.2C**).

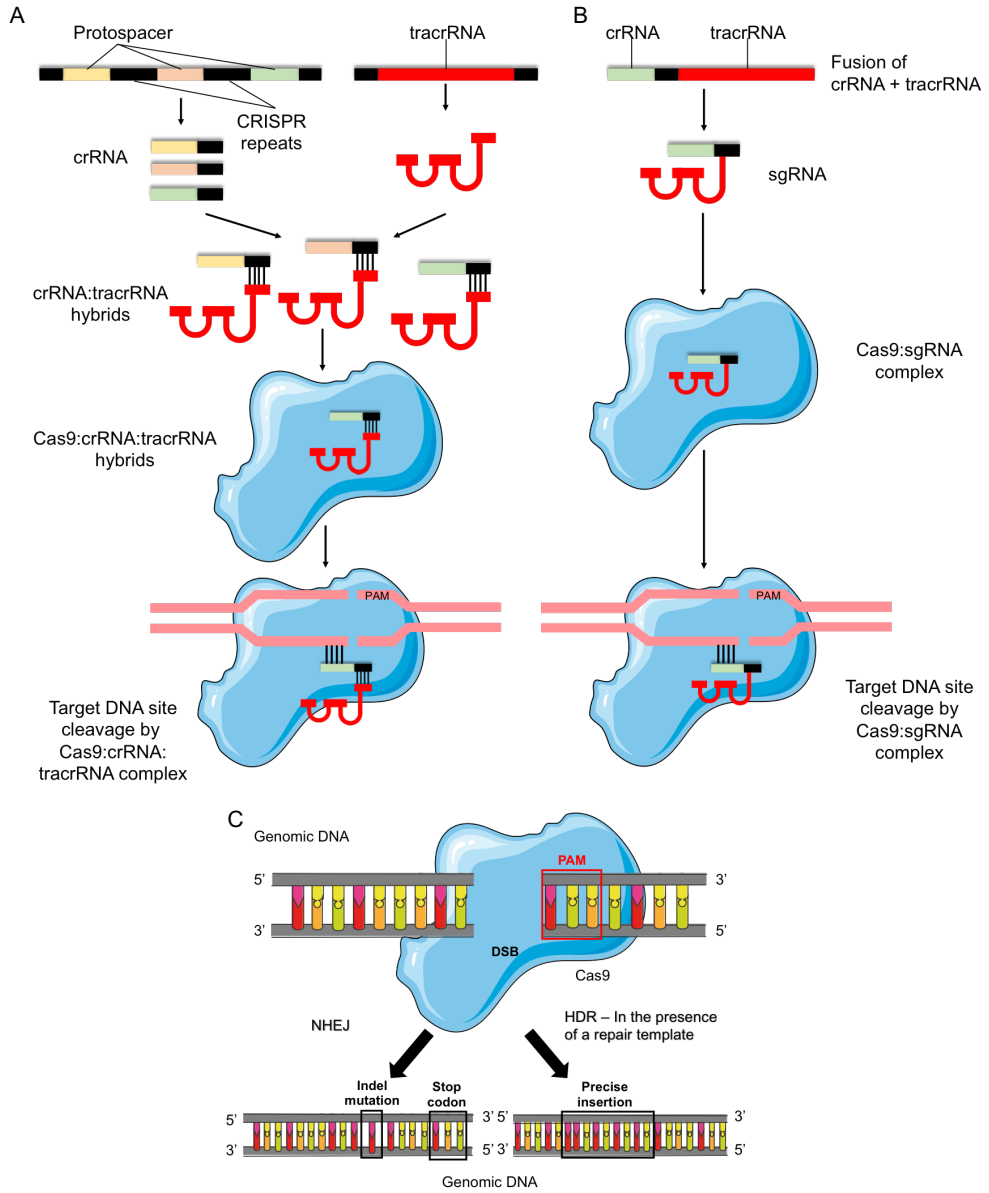

Figure 2.2: CRISPR/Cas9 harnesses the DNA repair mechanism to introduce precise genomic alterations. (A) Shows a naturally occurring CRISPR system, similar to Figure 2.1 **(B)** Shows the most widely used engineered CRISPR/Cas system. The system uses a sgRNA, which is a fusion between a crRNA and part of tracrRNA. The sgRNA associates with Cas9 and recognises the target sequence adjacent to a PAM, inducing a DSB. **(C)** Cas9 introduces a DSB, which is then repaired by NHEJ or in the presence of a repair template by HDR. NHEJ leads to the introduction of indel mutations and a premature stop codon, leading to gene disruption. HDR uses the repair template to introduce a precise insertion in the genome. Panels A and B were redrawn

from (Sander and Joung, 2014) and panel C was redrawn from (Ran et al., 2013b).

2.1.6 Advances in the CRISPR/Cas toolkit

The first versions of CRISPR provided specific genomic edits, but suffered from substantial off-target effects (Cradick et al., 2013, Fu et al., 2013). An early alternative to SpCas9 was the use of CRISPR nickases such as Cas9D1A, which are only able to mediate single-strand breaks. Targeting two DNA nickases to adjacent PAMs using two different sgRNAs can then create a DSB at the desired region. This is conditional upon both nickases simultaneously creating single-strand breaks at their respective targets. This method may reduce off-target activity by 50- to 1500- fold (Ran et al., 2013a). New Cas9 orthologs such as CPF1 (Zetsche et al., 2015), high-fidelity Cas9 (Kleinstiver et al., 2016) and enhanced specificity Cas9 (Slaymaker et al., 2016) were recently developed to minimise the chances for off-target effects and potentially eliminate them.

As an alternative to direct gene silencing, it is also possible to target gene regulatory regions to either activate or repress transcription. For example, nuclease-deficient Cas9, (dCas9), tagged with transcription factors cannot cleave DNA, but can be used to enhance gene expression upon interaction with regulatory regions (Qi et al., 2013, Larson et al., 2013, Gilbert et al., 2013, Konermann et al., 2015). CRISPR interference (CRISPRi) is a reversible gene repression system that works by blocking transcription activation via the creation of methylation marks enforcing gene repression. CRISPRi was shown to be more efficient than gene KOs introduced by indel mutations in the protein coding sequence as effects like incomplete loss-of-function or hypomorphic alleles are avoided (Mandegar et al., 2016).

2.1.7 CRISPR/Cas9 editing in HAP1 cells

CRISPR/Cas9 been proven to be a very versatile tool that can be used to genetically edit most model organisms (Ran et al., 2013b). It has been used in cultured cell lines to study loss-of-function by endogenous gene knock-outs. This process can be more challenging in diploid or polyploid model systems. Haploid systems are an attractive alternative as only one gene needs to be knocked out

to obtain a loss-of-function phenotype. HAP1 cells are a near-haploid human cell line (disomic only for a part of chromosome 15), which derives from the male chronic myelogenous leukemia cell line KBM-7 (Carette et al., 2011).

2.1.8 Aims of this Chapter

The aim of the work described in this chapter were to use gene-editing methods to develop and characterise mammalian cells devoid of all IP_3R (3-KO). Towards that aim, my objectives were:

1. To work with the Horizon Discovery Group to generate and characterise HAP1-KO (single KO, double KO and 3-KO) cell lines.
2. To establish a human embryonic kidney (HEK) 3-KO cell line using HEK cells devoid of IP_3R3, generated by Dr. V. Konieczny and N. Hoffman, as my starting point. From this point, I will refer to the cells lacking IP_3R3 as VK HEK IP_3R3-KO and their parental cell line as VK HEK WT.

During the course of my work another group published work reporting production of HEK 3-KO cells devoid of IP_3Rs (Alzayady et al., 2016). In light of this development, my additional objectives were revised to:

3. To validate HEK 3-KO cells generated by Alzayadi et al. (2016).
4. Establish the relative expression of IP_3R subtypes in HEK WT cells and cells expressing a single IP_3R subtype.

2.2 Materials and Methods

2.2.1 Materials

Gibco® DMEM/F-12 GlutaMAX™, Gibco® IMDM, TrypLE express, penicillin/streptomycin, Mag-fluo-4-AM, oligonucleotides, primers, Donkey anti-Rabbit IgG H&L (Alexa Fluor® 488), Donkey Anti-Rabbit IgG H&L (Alexa Fluor® 647), MagicMark™ XP, Spectra™ Multicolor Broad Range Protein Ladder, Tris-acetate SDS running buffer, 3-8% Tris-acetate PAGE (polyacrylamide gel electrophoresis) gels, and iBLOT transfer kit were from ThermoFisher (Paisley,

UK). Adenosine 5´-triphosphate disodium salt hydrate (ATP), histamine dihydrochloride, carbamylcholine chloride (carbachol, CCh), saponin, ethylenediaminetetraacetic acid (EDTA), cOmplete EDTA-free protease inhibitor cocktail, Trypan Blue, Poly-L-lysine, dimethyl sulfoxide (DMSO), Pluronic F-127, foetal bovine serum (FBS), Tween-20, dithiothreitol (DTT), Triton X-100, carbenicillin and Tris base were from Sigma-Aldrich (Poole, Dorset, UK). Fluo-8-AM was from Stratech Scientific (Suffolk, UK). Lysogeny broth was purchased from Formedium (Hunstanton, Norfolk, UK). Agarose, and α-select gold efficiency competent *E. coli* were from Bioline Ltd (London, UK). ECL prime Western blotting detection reagent was from SLS (Nottingham, UK). TransIT-LT1 transfection reagent was from Mirus Bio (Madison, WI, USA). QIAquick gel extraction kit, QIAprep spin miniprep, FastLane Cell cDNA Kit, QuantiTect Reverse Transcription Kit, and maxiprep kit were from Qiagen (Crawley, West Sussex, UK). ClonaCell-TCS medium was purchased from Stem Cell Technologies (Waterbeach, Cambridge, UK). Cyclopiazonic acid (CPA) was purchased from Tocris (Bristol, UK) and D-myo-inositol 1,4,5-trisphosphate (IP_3) hexapotassium salt was from Enzo Life Sciences (Exeter, UK). EZ-PCR mycoplasma kit was from Geneflow (Lichfield, UK). Q5® High-Fidelity DNA Polymerase was from New England Biolabs (Hitchin, UK). Restriction enzymes were from Fermentas Life Sciences (York, UK). All plasticware used for cell culture was from Greiner Bio-One (Stonehouse, UK). DC™ Protein Assay was from Bio-Rad (Watford, Hertfordshire, UK). pX330-U6-Chimeric_BB-CBh-hSpCas9 was a gift from Feng Zhang (Addgene plasmid # 42230) (Cong et al., 2013, Ran et al., 2013b).

2.2.2 Cell culture

VK HEK WT and VK HEK IP_3R3-KO cells were cultured in Dulbecco's modified Eagle's medium/Ham's F12 (DMEM) with GlutaMAX and supplemented with 10% FBS. CRISPR-edited HEK cells expressing a single IP_3R subtype (HEK IP_3R1, HEK IP_3R2 and HEK IP_3R3), HEK 3-KO and the parental HEK WT cell line from which they derive, were from Kerafast (Boston, MA, USA). Gene-edited HeLa cells, in which IP_3R1 was endogenously tagged with GFP (Thillaiappan et al., 2017), were cultured in Dulbecco's modified Eagle's medium/Ham's F12 (DMEM) with GlutaMAX and supplemented with 10% FBS.

HAP1 cells were cultured in Iscove's modified Dulbecco's medium (IMDM) with penicillin/streptomycin and 10% FBS. Table 1 describes the HAP1 cells generated by the Horizon Discovery Group and their associated mutations.

All cells were maintained in a humidified air at 37°C with 5 % CO_2. Cells were passaged when they reached ~80 % confluence. The medium was removed and cells were detached using TrypLE express. When the cells detached, they were re-suspended in medium and centrifuged at 600 xg for 5 min. The old medium was aspirated and cells were seeded in a new flask usually at a 1:10 dilution. Details on how many cells were seeded in each experiment are provided in subsequent sections. The cells were routinely screened for mycoplasma infection to ensure that all cells used were mycoplasma-free.

	Cell line	IP_3R	Mutation
HAP1 Parental	WT		N/A
HAP1 Single KO	IP_3R1 KO-1	IP_3R1	7 bp deletion in exon 4
	IP_3R1 KO-2	IP_3R1	2 bp deletion in exon 4
	IP_3R2 KO-1	IP_3R2	10 bp deletion in exon 2
	IP_3R2 KO-2	IP_3R2	23 bp deletion in exon 3
	IP_3R2 KO-3	IP_3R2	17 bp deletion in exon 3
	IP_3R2 KO-4	IP_3R2	2 bp deletion in exon 2
	IP_3R3 KO-1	IP_3R3	1 bp deletion in exon 3
HAP1 Double KO	$IP_3R1/2$ KO	IP_3R1 IP_3R2	23 bp deletion in exon 4 10 bp deletion in exon 2
	$IP_3R1/3$ KO	IP_3R1 IP_3R3	7 bp deletion in exon 4 1 bp deletion in exon 3
	$IP_3R2/1$ KO	IP_3R2 IP_3R1	8 bp deletion in exon 2 7 bp deletion in exon 4
	$IP_3R2/3$ KO	IP_3R2 IP_3R3	11 bp deletion in exon 2 1 bp deletion in exon 3
	$IP_3R3/1$ KO	IP_3R3 IP_3R1	19 bp deletion in exon 3 7 bp deletion in exon 4
	$IP_3R3/2$ KO	IP_3R3 IP_3R2	4 bp deletion in exon 3 10 bp deletion in exon 2
HAP1 Triple KO	$IP_3R3/1/2$ KO	IP_3R3 IP_3R1 IP_3R2	1 bp deletion in exon 3 23 bp deletion in exon 4 10 bp deletion in exon 2
	$IP_3R1/3/2$ KO	IP_3R1 IP_3R3 IP_3R2	7 bp deletion in exon 4 4 bp deletion in exon 3 10 bp deletion in exon 2

Table 2.1 List of HAP1 cell lines used. The code used to define each cell line reports the sequence in which IP_3R genes were disrupted (i.e $IP_3R1/2$ KO denotes a cell line with IP_3R1 disrupted before IP_3R2.

2.2.3 Disruption of IP_3R genes using CRISPR/Cas9 in HEK cells

To generate a HEK cell line devoid of IP_3Rs, I double transfected VK HEK IP_3R3-KO cells with two constructs, one that would disrupt IP_3R1 and another that would disrupt IP_3R2. I used two constructs that targeted IP_3R1 so each construct was double-transfected with the construct targeting IP_3R2.

1.6×10^5 VK HEK IP_3R3-KO cells were seeded in each well of a 6-well plate. After 24h cells were transfected with 4µg of CRISPR plasmid DNA using the TransIT®-LT1 transfection reagent. 24h after transfection, the cells were detached and counted. 200 cells were plated in each well of a 6-well plate in ClonaCell-TCS medium for clonal selection. The cells were maintained in humidified air at 37°C with 5 % CO_2 until single colonies were visible. The colonies were expanded and tested for the expression of IP_3R1. Any clones in which IP_3R1 appeared to be absent using western blotting, were blotted for IP_3R2.

2.2.4 Western blotting

Cells were lysed in cold RIPA buffer (1mM Tris HCl, 15mM NaCl, 0.5mM EDTA, 0.1% Triton X-100, pH 7.5) with protease inhibitors. The samples were sonicated for 30s, incubated on ice for 30min and supernatants were collected after centrifugation (900xg, 15min, 4°C). A DC™ Protein Assay kit, with bovine serum albumin (BSA) as standard, was used to determine the protein concentration of the lysates. The cytoplasmic extract cytoplasmic extract was electrophoresed in NuPAGE® Novex® 3-8% Tris-acetate protein gels and transferred to a PVDF membrane using iBlot. MagicMark™ XP and Spectra™ Multicolor Broad Range Protein Ladder were used. Membranes were blocked in Tris-buffered saline (TBS: 50mM Tris-HCl, 150mM NaCl, pH 7.6, 0.2% Tween-20, 5% w/v BSA) for 1h. The membrane was then rinsed in TBS and incubated for 12h at 4°C with the primary antibody (Table 2.2) diluted in TBS. The membrane was then washed three times for 10min with TBS, and then incubated for 1h with the secondary antibody (Table 2.2). This was followed by three 10min washes in TBS. Finally, the membrane was incubated with ECL Western blotting detection reagents prior to development using a Syngene PXi chemiluminescence detection system (Cambridge, UK).

Antibody	Dilution	Receptor	Recognition site	Manufacturer/Supplier
AbC	1:500	IP_3R (common)	Affinity-purified, N-terminal, residues 65-75	Poccono Rabbit Farm and Laboratory Inc. (Canadensis, PA, USA)
Ab1	1:1000	IP_3R1	C-terminal, antigen surrounds Met2750	#3763 Cell Signaling Technology (Leiden, The Netherlands)
Ab2	1:1000	IP_3R2	Affinity-purified, C-terminal, residues 2685-2701	Poccono Rabbit Farm and Laboratory Inc.
Ab3	1:1000	IP_3R3	N-terminal	#610312, BD Biosciences, (Wokingham, UK)
S1	1:1000	IP_3R1	C-terminal, residues: 2732-2748	Poccono Rabbit Farm and Laboratory Inc.
S2	1:1000	IP_3R2	C-terminal, residues 2685-2701	Poccono Rabbit Farm and Laboratory Inc.
S16	1:1000	IP_3R (common)	N-terminal residues	Poccono Rabbit Farm and Laboratory Inc.
β-actin	1:50000	N/A	N/A	#3700, Cell Signaling Technology
Anti-mouse IgG-HRP	1:5000	N/A	N/A	sc-516102, Insight Biotechnology Ltd (Wembley, UK)
Anti-rabbit IgG-HRP	1:5000	N/A	N/A	sc-2357, Insight Biotechnology Ltd

Table 2.2: Antibodies used

2.2.5 Immunostaining of HEK 3-KO and HeLa GFP-IP_3R1 cells

Cells (50,000) were seeded on imaging dishes (section 3.2.1). After 24 hours, the cells were washed with Phosphate-buffered saline (PBS) and fixed using paraformaldehyde (4% in PBS, 20min). Cells were then permeabilised using Triton (0.25% in PBS, 5min), blocked using BSA (5% w/v in PBS, 1h) and incubated with AbC (Table 2.2) (1:500 in PBS with 3% w/v BSA, 4°C, overnight, shaking). After three PBS washes, the cells were incubated with the secondary antibody in PBS with 3% w/v BSA (1:5000 donkey anti-rabbit IgG (Alexa Fluor® 488) in HEK 3-KO cells and 1:5000 donkey anti-rabbit IgG (Alexa Fluor® 647) in HeLa GFP-IP_3R1 cells). The samples were imaged using TIRFM (the microscope is described in section 3.2.3).

2.2.6 Reverse transcription polymerase chain reaction (RT-PCR) of *itpr1* mRNA

HEK WT and HEK 3-KO cells were seeded on a 24-well plate (10^4 cells/well) and grown to confluence. After genomic DNA elimination, cDNA synthesis was carried out using FastLane Cell cDNA kit according to the manufacturer's protocol. The obtained cDNA was used in a PCR reaction using Q5® High-Fidelity DNA polymerase. The primers are listed in Table 2.3. The reaction was set up according to the manufacturer's instructions.

Primer Pair	Orientation	Sequence	Location	Expected Size
1	Forward	CTCAGGAAGCCGTCCAAAGA	Spans exons 55 - 59	592
	Reverse	CTGGTTGTTGTGGGTTGACA		
2	Forward	GCTGCTGATGTGCATTGTCA	Spans exons 55-59	599
	Reverse	TCTGCTTCCTTTGTTCTGTCA		

Table 2.3: Primers used to amplify *itpr1* mRNA. Primers were designed using Primer-Blast online software and blasted to ensure that they are specific.

The samples were run on a 1% agarose gel to determine whether there is a PCR product.

2.2.7 Measurement of $[Ca^{2+}]_c$

Measurements of $[Ca^{2+}]_c$ were carried out as previously described (Tovey et al., 2006). HEK293 cells (50,000 per well) were seeded in poly-L-lysine-coated black full-area 96-well plates and grown to confluence (48h). Cells were washed with Hepes-buffered saline (HBS) which has the following composition: 135mM NaCl, 5.9mM KCl, 1.2mM $MgCl_2$, 1.5mM $CaCl_2$, 11.6mM HEPES and 11.5mM D-glucose, adjusted to pH 7.3 with NaOH. Cells were loaded with the Ca^{2+} indicator fluo-8, by incubation of 2μM fluo-8-AM in HBS with 0.02% pluronic acid for 1h in the dark. The cells were washed and incubated in the dark with HBS to allow de-esterification of the indicator. After 30min, HBS was replaced with new HBS to remove any excess dye in the medium. A FlexStation 3 fluorescence plate-reader (MDS Analytical Devices, Wokingham, UK) was used to record fluorescence.

Experiments were performed at 20°C in HBS, and fluo-8 fluorescence (excitation at 494nm, emission at 516nm) was measured every 1.44s in response to addition of CCh, ATP, histamine or caffeine. Maximal (F_{max}) and minimal (F_{min}) fluorescence signals were determined at the end of the experiment by addition of 10mM $CaCl_2$ in HBS with 0.1% Triton (F_{max}) or 10mM 1,2-bis(O-aminophenoxy)ethane-N,N,N',N'-tetraacetic acid (BAPTA) in Ca^{2+}-free HBS with 0.1% Triton (F_{min}). Fluorescence signals (F) were calibrated to $[Ca^{2+}]_c$ using the following equation: $[Ca^{2+}]_c = K_d \times \frac{F - F_{min}}{F_{max} - F}$, where K_d = 389nM. Responses are reported as $\Delta[Ca^{2+}]_c$, where $\Delta[Ca^{2+}]_c = [Ca^{2+}]_{c,peak} - [Ca^{2+}]_{c,baseline}$.

2.2.8 Ca^{2+} release from permeabilised cells

A confluent T75 flask of cells was loaded with the low-affinity Ca^{2+} indicator Mag-Fluo-4. Cells were loaded by incubation with 20μM Mag-Fluo-4-AM in HBS containing 1mg/ml BSA and 0.02% (v/v) pluronic acid, on a rocking platform at 20°C. After 1h, cells were resuspended in cytosol-like medium (CLM) without Ca^{2+} (Ca^{2+}-free CLM) with the following composition: 140mM KCl, 20mM NaCl, 1mM ethylene glycol bis(β-aminoethyl ether)-N,N,N',N'-tetraacetic acid (EGTA),

2mM $MgCl_2$ and 20mM PIPES, pH 7.0. The cells were permeabilised using 10µg/ml saponin (2-3 min at 37°C). Once permeabilisation was observed using Trypan Blue staining, cells were centrifuged (600xg for 2min) and resuspended in 2.75ml Mg^{2+}-free CLM (140mM KCl, 20mM NaCl, 1mM EGTA, 375µM $CaCl_2$ and 20mM PIPES, pH 7.0). 45µl of the permeabilised cells were plated per well on a black half-area 96-well plate and the plate was then centrifuged at 300xg for 2min. Mag-Fluo-4 (excitation at 485nm, emission at 525nm) fluorescence was recorded every 1.44s at 20°C using a FlexStation 3 fluorescence plate reader. MgATP (1.5mM) was used to stimulate Ca^{2+} uptake from the intracellular stores, and after 2min, IP_3 was added in combination with the SERCA inhibitor CPA (10µM).

Results are reported in relative fluorescence units (RFU) and as percent Ca^{2+} release from the fully loaded intracellular stores using the following equation: % Ca^{2+} release = 100 x $\frac{t_2-t_3}{t_2-t_1}$, where t_1=baseline RFU, t_2=RFU after stimulation with MgATP and t_3=RFU after stimulation with IP_3. From previous work, it has been established that when the intracellular stores are full, Mag-fluo-4 is not saturated. Therefore, Mag-fluo-4 fluorescence can be used to report Ca^{2+} release from the stores without further calibration (Laude et al., 2005, Tovey et al., 2006).

2.3 Results and Discussion

My work began with HEK cells in which CRISPR/Cas9 had already been used to endogenously disrupt the IP_3R3 gene (*itpr3*). I aimed to disrupt the genes for the remaining IP_3R subtypes. Secondly, Horizon Discovery Group (a life-science company) was commissioned to provide HAP1 cells with all IP_3R genes disrupted. I was actively involved in the progress towards that aim, mainly by being responsible for the characterisation of the KO cell lines. Because, the work on both cell types was performed in parallel, results obtained from each set of experiment were often used to guide the parallel analyses.

2.3.1 Characterisation of HAP1 cells

HAP1 cells in culture have fibroblast-like morphology **(Figure 2.3A)**, which agrees with previous reports (Essletzbichler et al., 2014). The cells respond to ATP with an increase in $[Ca^{2+}]_c$ in a concentration-dependent way, but are insensitive to histamine and CCh **(Figure 2.3B & C)**. In addition, caffeine which activates RYRs did not evoke a Ca^{2+} signal **(Figure 2.3B & C)**. Others in the lab have reported that HAP1 cells are hard to transfect. With HAP1 cells shown to be amenable to analyses of Ca^{2+} signals, the decision to proceed with the generation of triple KO cells was taken.

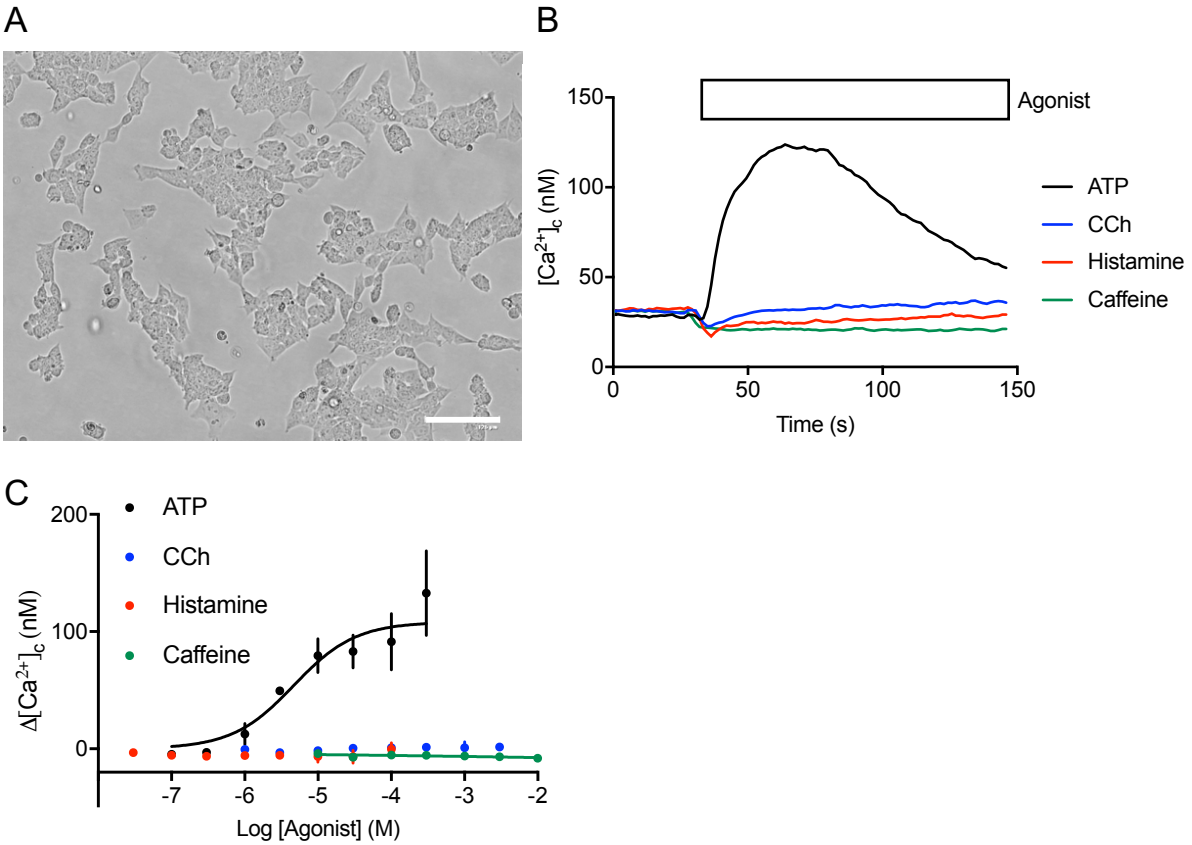

Figure 2.3: HAP1 cells have a fibroblast-like morphology and respond to ATP. (A) Wild-type HAP1 cells in culture. Scale bar is 125µm. **(B)** Populations of HAP1 cells were incubated in HBS and were stimulated with either ATP (300µM), CCh (3mM), histamine (100µM) or caffeine (10mM). Results show the mean $[Ca^{2+}]_c$ traces of four (three for caffeine) replicates within a single experiment (*n* = 1). **(C)** Shows the concentration dependent effects of the indicated ligands on the peak increase in $[Ca^{2+}]_c$ ($\Delta[Ca^{2+}]_c$). Data are means (each value is the mean of four experimental replicates) ± s.e.m. from independent experiments (*n* = 3 for ATP, CCh and Histamine and *n* = 2 for caffeine).

2.3.2 Characterisation of HAP1 cells engineered to lack IP_3Rs

The first round of CRISPR/Cas9 editing in HAP1 cells provided me with three independent cell lines. Each cell line was treated with a sgRNA targeting a single IP_3R subtype. The Horizon Discovery Group during their screening process (PCR amplification and Sanger sequencing) established that each cell line had genomic edits for a single IP_3R subtype.

Using subtype-specific antibodies, it was shown that the IP_3R3 KO-1 (Table 2.1) cell line retained expression of IP_3R1 and IP_3R2 (**Figure 2.4A & B**) while it lacked its cognate subtype (**Ab3**, Table 2.2) (**Figure 2.4C**). Similarly, using an anti-IP_3R2 antibody (**S2**, Table 2.2), IP_3R2 KO-1 (Table 2.1) appeared to have a faint band in its cognate KO (**Figure 2.4B**) and retained expression of the other two subtypes (**Figure 2.4A & C**). Given that the antibody had not been affinity purified yet, it was possible that the very faint band might be non-specific.

Using a C-terminal anti-IP_3R1 antibody (**S1,** Table 2.2), it appeared that the edited IP_3R1 KO-1 cell line (Table 2.1) retained expression of IP_3R1 (**Figure 2.4A**). At this stage, there was no reason to doubt the specificity of the S1 antibody as its specificity had been established in DT40 cells expressing only a single mammalian IP_3R subtype (Saleem et al., 2012). Therefore, it was deduced that either a wrong cell line was shipped that did not match the sequenced cell line or that the IP_3R1 KO-1 cell line was not monoclonal, with wild-type cells polluting and gradually overtaking the KO cells during cell culture.

The results so far suggest that HAP1 cell lines without IP_3R3 (IP_3R3 KO-1) and possibly without IP_3R2 (IP_3R2 KO-1) had been successfully generated. I certified the latter using an affinity-purified anti-IP_3R2 antibody (**Ab2**, Table 2.2), which clearly demonstrated successful disruption of the IP_3R2 gene in four different clones of IP_3R2-KO cells (**Figure 2.5**). However, there were serious concerns surrounding the effectiveness of the IP_3R1 KO.

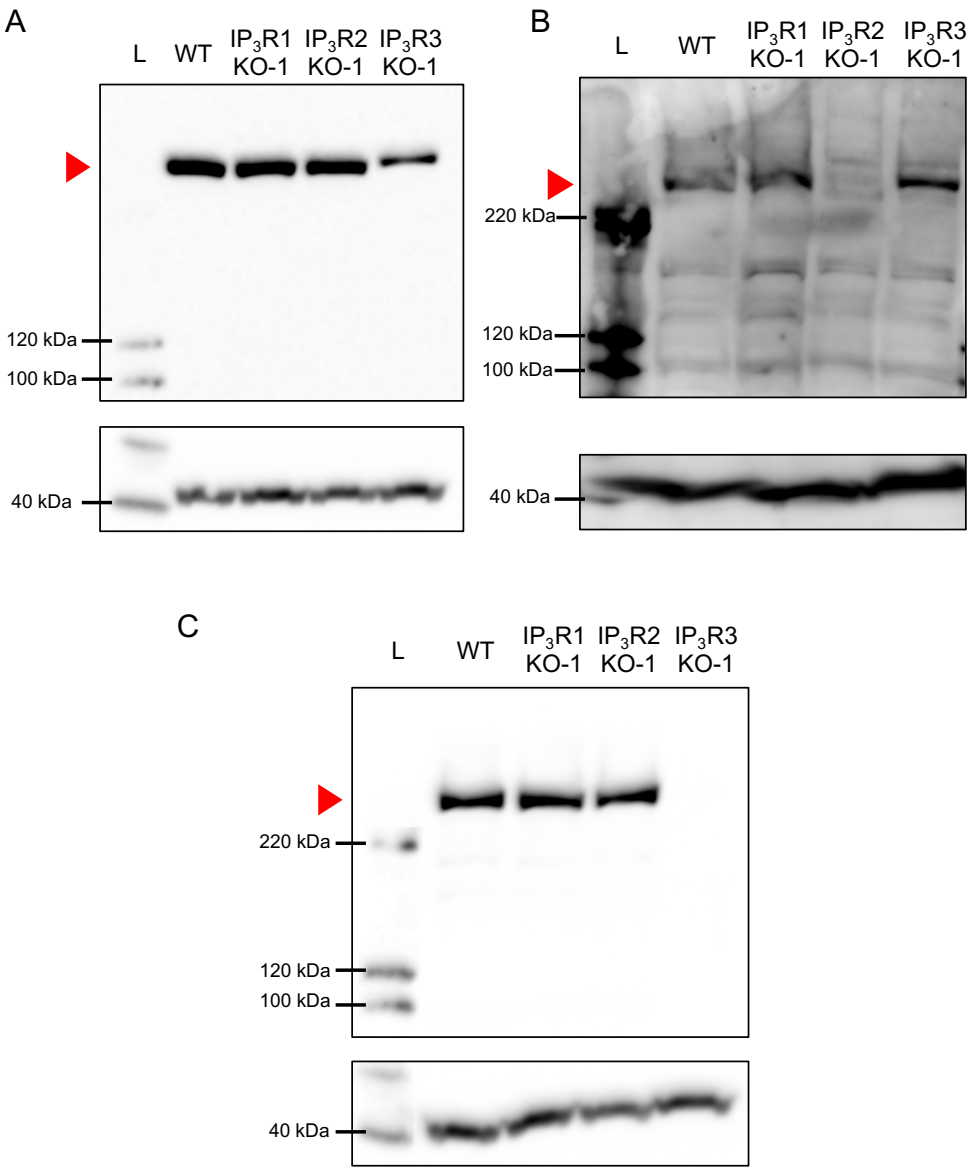

Figure 2.4: The HAP1 IP_3R3 KO cell line lacks its cognate subtype. Lysate supernatants from three HAP1 cell lines, each endogenously disrupted for a single IP_3R. Lysates (40μg) from gene-edited HAP1 cells (IP_3R1-KO-1, IP_3R2-KO-1 and IP_3R3-KO-1, Table 2.1) and the parental HAP1 WT cell line were analysed by Western blotting. Cell lysates were blotted using **(A)** an anti-IP_3R1 antibody (S1, 1:1000, Table 2.2), **(B)** an anti-IP_3R2 antibody (S2, 1:1000, Table 2.2) and **(C)** an anti-IP_3R3 antibody (Ab3, 1:1000, Table 2.2). Red arrows indicate position of IP_3Rs. M_r markers (L) and β-actin blots (low panels) are also displayed. Results in panels A and C are representative of three independent experiments (*n* = 3). Results in panel B are from one experiment, but were later confirmed with an affinity-purified antibody (**Figure 2.5**).

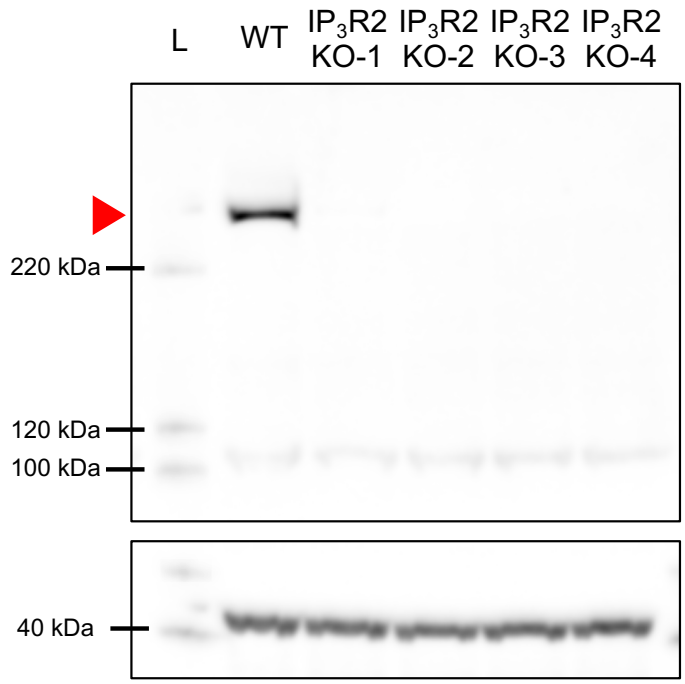

Figure 2.5: An affinity-purified antibody shows disruption of the IP_3R2 gene in four independent IP_3R2-KO cell lines. Lysates from four independent cell lines in which the IP_3R2 gene had been disrupted using CRISPR/Cas9. 40μg of WT, IP_3R2-KO-1, IP_3R2-KO-2, IP_3R2-KO-3, IP_3R2-KO-4 lysates were analysed by Western blotting. Blots were performed using an affinity-purified anti-IP_3R2 antibody (Ab2, 1:1000, Table 2.2). Red arrows indicate position of IP_3Rs. M_r markers (L) and β-actin blots (low panels) are also displayed. Results are representative of three independent experiments (*n* = 3).

An independent IP_3R1-KO clone was generated using the same sgRNA used for the generation of the clone tested in **Figure 2.5**, but it was shown to have a different mutation in the genome (Table 2.1). Screening with the same subtype-specific antibody (S1) suggested that both independent KO cell lines express IP_3R1 **(Figure 2.6A)**. The possibility that the first clone had been polluted with WT cells was excluded by these data. A possible explanation for the latest results might be the presence of C-terminal fragments. This explanation cannot be excluded from the current gels as the native IP_3R protein is so large that it is impossible to detect loss of a few amino acid residues at the N-terminus of the

protein. These fragments may exist if there are alternative start sites within the transcribed mRNA. This possibility has been reported for other gene-edited proteins and may suffice to study a loss-of-function phenotype (Chua et al., 2012, Fukushima et al., 2012). This, however, is not the case for IP_3Rs as C-terminal fragments might assemble with full-length protein rendering results uninterpretable. A second explanation may be that the S1 antiserum in HAP1 cells lacks specificity for IP_3R1. This is plausible, as there had been no prior opportunity to assess its specificity in HAP1 cells. To exclude the latter, a new antibody (Ab1) was obtained that recognises a similar region to S1 on the C-terminus of IP_3R1 (Table 2.2).

To determine whether the conflicting data between Western blot analysis and genome sequencing may be attributed to antibody specificity, all single IP_3R1-KO clones were blotted with Ab1. The blots obtained with Ab1 suggested that IP_3R1 is absent from the cognate KO cell lines (**Figure 2.6B)**. Considering the results obtained with HEK cells (section 2.3.3) it was concluded that IP_3R1 is absent from all IP_3R1 KO cell lines.

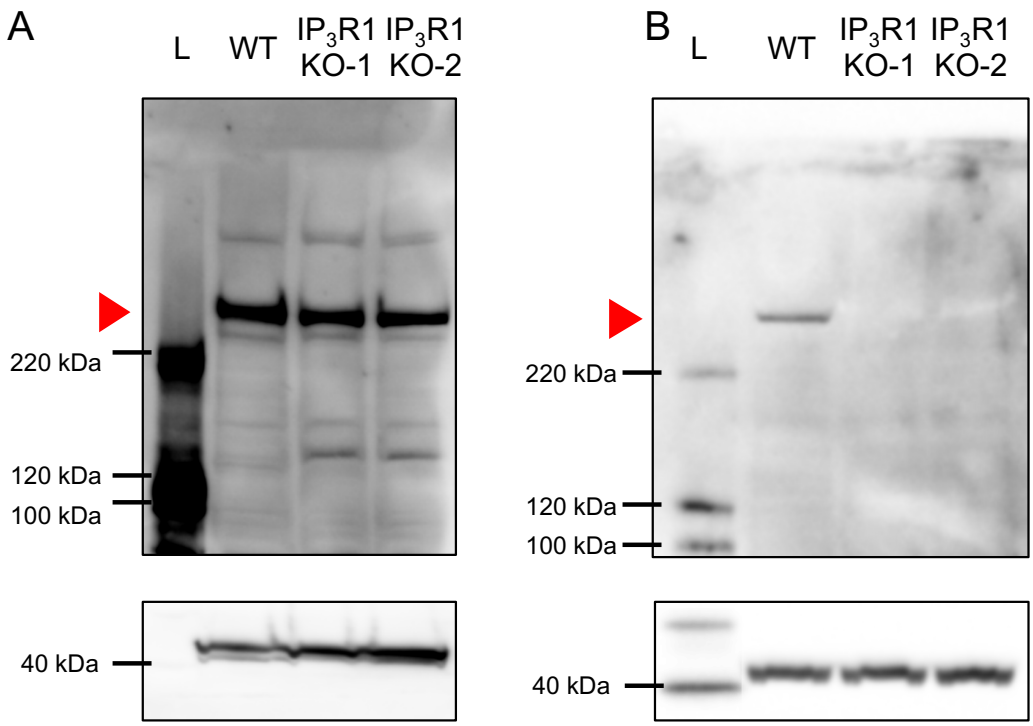

Figure 2.6: A commercial anti-IP_3R1 antibody shows disruption of the IP_3R1 gene in two independent IP_3R1-KO cell lines. 40μg WT, IP_3R1-KO-1 and IP_3R1-KO-2 lysates were analysed by Western blotting. Blots were performed using S1 (1:1000, Table 2.2) **(A)** and a commercial anti-IP_3R1 antibody (Ab1, 1:1000, Table 2.2) **(B)**. Red arrows indicate position of IP_3Rs. M_r markers (L) and β-actin blots (low panels) are also displayed. Results are representative of three independent experiments (*n* = 3).

Having established that HAP1 single-subtype KO cells each lack their cognate IP_3R subtype, Horizon Discovery Group proceeded with the preparation of double- and triple-KO cell lines. Six double mutants were generated in total (two independent cell lines for each remaining subtype) and each was shown to express only the expected IP_3R subtype **(Figure 2.7)**.

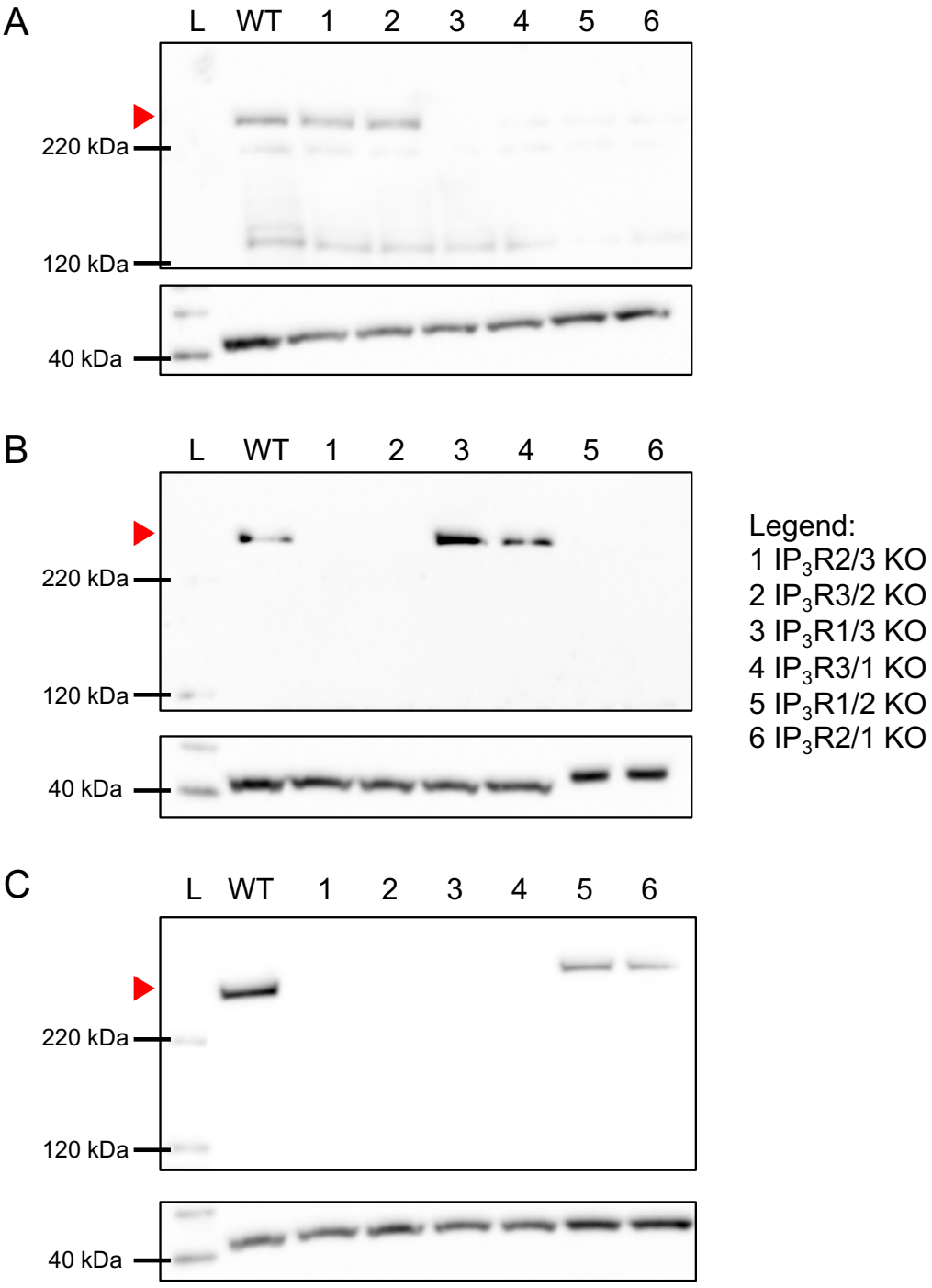

Figure 2.7: Six independently generated double HAP1 KO cell lines lack their cognate IP_3R. Lysates from six independent cell lines in which two IP_3R genes have been disrupted using CRISPR/Cas9 (see Table 2.2). 40μg of WT and double KO lysates were analysed by Western blotting. Blots were performed using **(A)** Ab1 (1:1000, Table 2.2), **(B)** Ab2 (1:1000, Table 2.2) and **(C)** Ab3 (1:1000, Table 2.2). Red arrows indicate position of IP_3Rs. M_r markers (L) and β-actin blots (low panels) are also displayed. Results are representative of two independent experiments *(*n = 2*)*.

HAP1 3-KO cells were generated by Horizon Discovery Group in which sequencing showed disruption of all three IP_3R subtypes (Table 2.1). Western blotting of HAP1 cells devoid of IP_3Rs using subtype-specific antibodies (Ab1, Ab2 and Ab3) confirmed the absence of all IP_3R subtypes **(Figure 2.8A, B & C)**. It was also necessary to validate that HAP1 3KO cells do not release any Ca^{2+} when stimulated. After permeabilization, IP_3-evoked Ca^{2+} release was abolished in HAP1 3-KO cells, confirming that there are no functional IP_3Rs **(Figure 2.8D & E)**. Additionally, lack of IP_3Rs does seem to not have an effect in the uptake of Ca^{2+} by the intracellular stores **(Figure 2.8D)**.

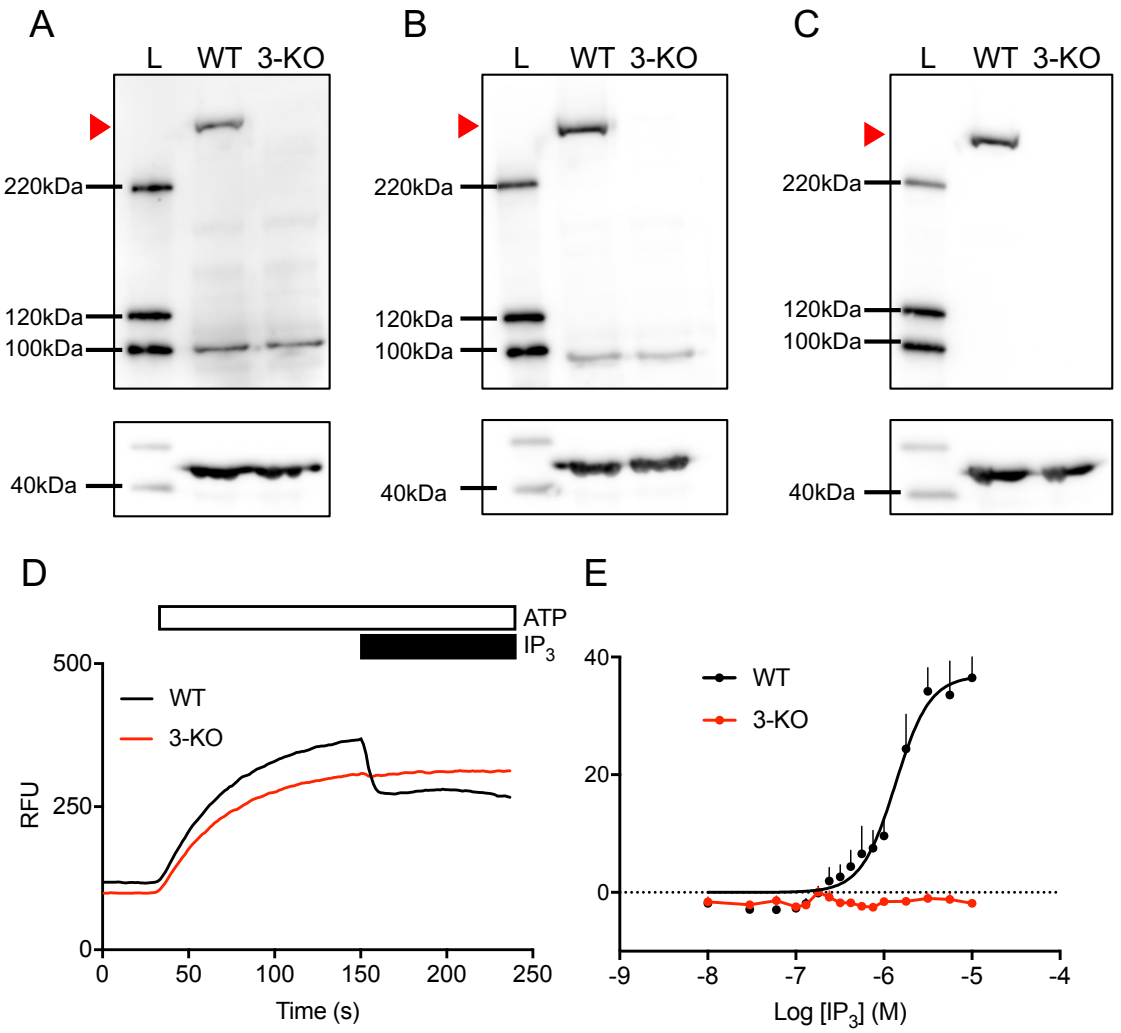

Figure 2.8: HAP1 3-KO cells lack all IP_3R subtypes and IP_3-evoked Ca^{2+} release. Lysates (40μg) of HAP1 WT and HAP1 3KO cell lines analysed by Western blotting. Lysates were blotted using **(A)** Ab1 (1:1000, Table 2.2), **(B)** Ab2 (1:1000, Table 2.2) and **(C)** Ab3 (1:1000, Table 2.2). Red arrows indicate position of IP_3Rs. M_r markers (L) and β-actin blots (low panels) are also displayed. Results are representative of three independent experiments (*n* = 3). **(D)** Shows Mag-Fluo-4 fluorescence in the ER of permeabilised HAP1 WT and HAP1 3-KO cells. Addition of MgATP (1.5mM) induces Ca^{2+} uptake in the ER in both cell lines. After 2min, IP_3 (10μM) induces Ca^{2+} release from the ER in HAP1 WT cells, whereas IP_3-evoked Ca^{2+} release in HAP1 3-KO cells is abolished. The data are the mean of three experimental triplicates from a single experiment (*n* = 1). **(E)** Shows the concentration-dependent effect of IP_3 on Ca^{2+} release (expressed as % of ER Ca^{2+} content) in HAP1 WT cells. IP_3-evoked Ca^{2+} release is abolished in HAP1 3-KO. The data shown are the mean ± s.e.m from four independent experiments (*n* = 4).

2.3.3 Characterisation of HEK 3-KO cell lines

In parallel to the generation of HAP1 KO cells, I tried to gene-edit VK HEK IP_3R3 KO cells to knock out the remaining subtypes. I transfected VK HEK IP_3R3 KO with two combinations of sgRNAs and picked colonies of monoclonal cells. Unfortunately, the screening for IP_3R1 expression used the S1 antibody before I had recognised the lack of specificity of this antiserum in HAP1 cells. This may explain, after screening ~100 clones, that only one clone appeared to have lost IP_3R1 (**Figure 2.9A, lane 9**). The clone was expanded and blotted with S1 and an antibody common to all IP_3Rs (S16, Table 2.2), and faint bands were detected by both antibodies. With hindsight, it seems that this lack of band may be unrelated to loss of IP_3R expression. It seems likely that some of the discarded clones may have had their IP_3R1 gene successfully disrupted.

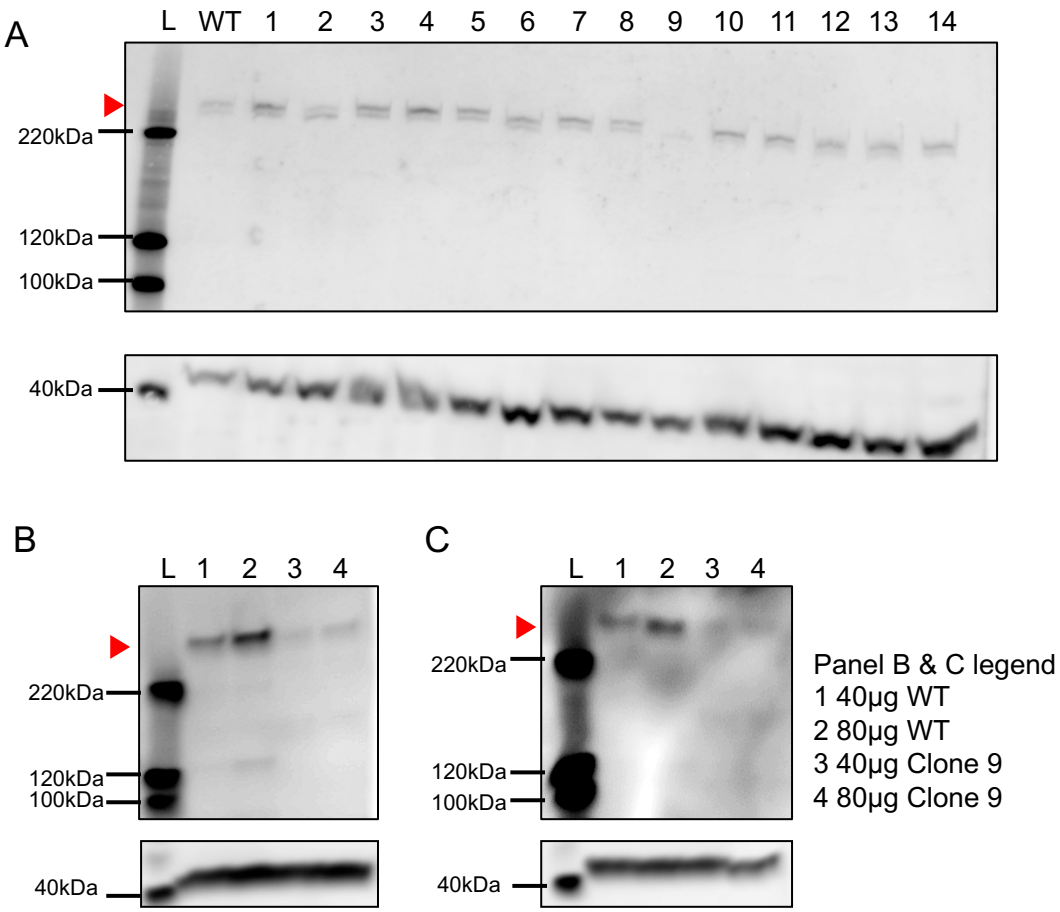

Figure 2.9: Candidate HEK 3-KO cell line shows residual IP_3R expression and Ca^{2+} release. (A) Lysates (20µg) from HEK WT cells (WT) and HEK VK IP_3R3 KO cells that had been further gene-edited using sgRNAs to the remaining subtypes (Lanes 1-14) were analysed by Western blot. This representative blot shows 14 different clones from ~100 that were tested (*n* = 1 for each clone). Lysates were blotted using S1 (1:1000, Table 2.2). The clone from lane 9 appeared to lack IP_3R1, so it was expanded and blotted with **(B)** S1 and **(C)** an antibody common to all IP_3Rs (S16, 1:1000, Table 2.2). Red arrows indicate position of IP_3Rs. M_r markers (L) and β-actin blots (low panels) are also displayed.

Recalling that while this work was in progress, I had no reason to doubt the specificity of S1, the results (**Figure 2.9**) so far suggested that there might be residual expression of IP_3R1 (and possibly IP_3R2) in the cell line in which I had attempted to disrupt all IP_3R genes. Two possibilities were that not all copies of *itpr1* were disrupted. There may have been more as Karyotype analysis (by Dr V. Konieczny) suggested that HEK cells possibly had 3 copies of *itpr1*.

Alternatively, the cell line may not have been monoclonal and included un-edited cells. To address the latter, I seeded cells in semi-solid medium to isolate new clonally-derived cell lines. The number of colonies was very low and in all of them IP_3R1 expression (screened using S1) was comparable to that of HEK293 WT cells **(Figure 2.10)**.

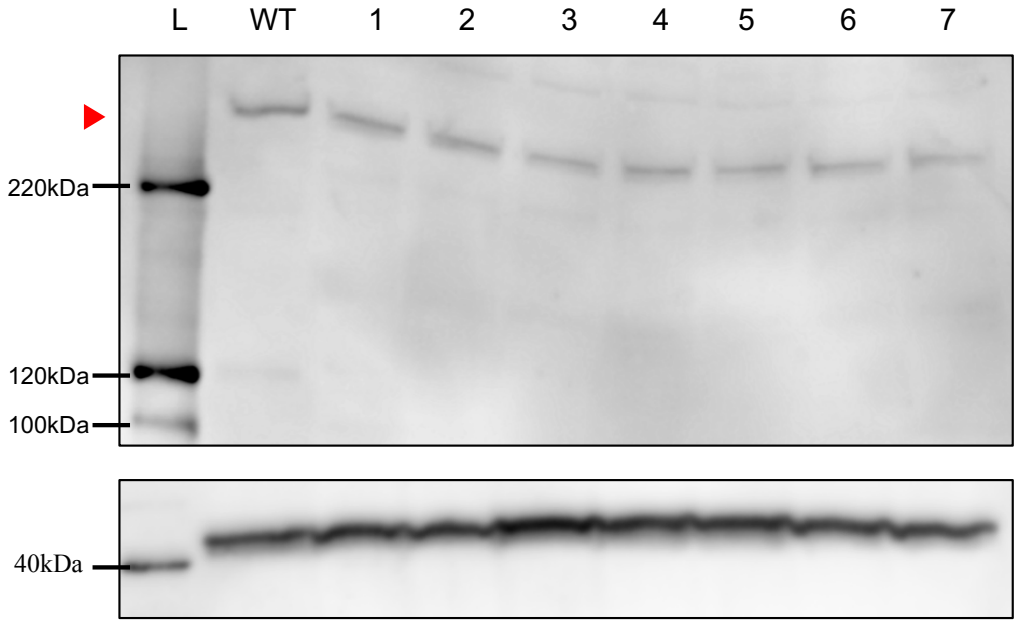

Figure 2.10: Clones derived from the candidate HEK 3-KO cell line express IP_3R1. WT and clonally-derived cell populations from the candidate HEK 3-KO (lanes 1-7) cell line were expanded and analysed using S1 (1:1000, Table 2.2) by Western blotting (*n* = 1 for each clone). Red arrows indicate position of IP_3Rs. M_r markers (L) and β-actin blots (low panels) are also displayed.

In summary, I screened ~100 clones for IP_3R1 expression (S1). Fortuitously, before embarking on another round of CRISPR with new sgRNAs, Alzayady and colleagues successfully generated a HEK 3-KO cell line (Alzayady et al., 2016). I, therefore, abandoned further attempts to generate a HEK 3-KO cell line, and from here on, the work described is exclusively on HEK cells generated by Alzayady and colleagues.

HEK 3-KO cells (Alzayady et al., 2016) were blotted using subtype-specific antibodies (S1, Ab1, Ab2 and Ab3) and a common antibody designed to

recognise an amino acid sequence conserved among the three subtypes (AbC). Blotting with S1 suggested that there is residual IP_3R1 in the HEK 3-KO cell line (**Figure 2.11A**). This observation was similar to results obtained with this antibody in HAP1 cells and VK IP_3R3-KO cells **(Figures 2.4, 2.6, 2.9 & 2.10)**. Blotting with Ab1, however, suggested that the IP_3R1 gene had been successfully disrupted (**Figure 2.11B**). Blotting with the IP_3R2- and IP_3R3- specific antibodies confirmed the absence of the cognate protein in HEK 3-KO cells **(Figure 2.11C and D)**. A common antibody recognising all IP_3R subtypes (AbC, Table 2.2) suggested that the cell line is devoid of all IP_3R subtypes **(Figure 2.11E)**. Direct stimulation of the IP_3R with IP_3 did not evoke any Ca^{2+} release in the HEK 3-KO cell line, confirming that they lack functional IP_3Rs **(Figure 2.12)**.

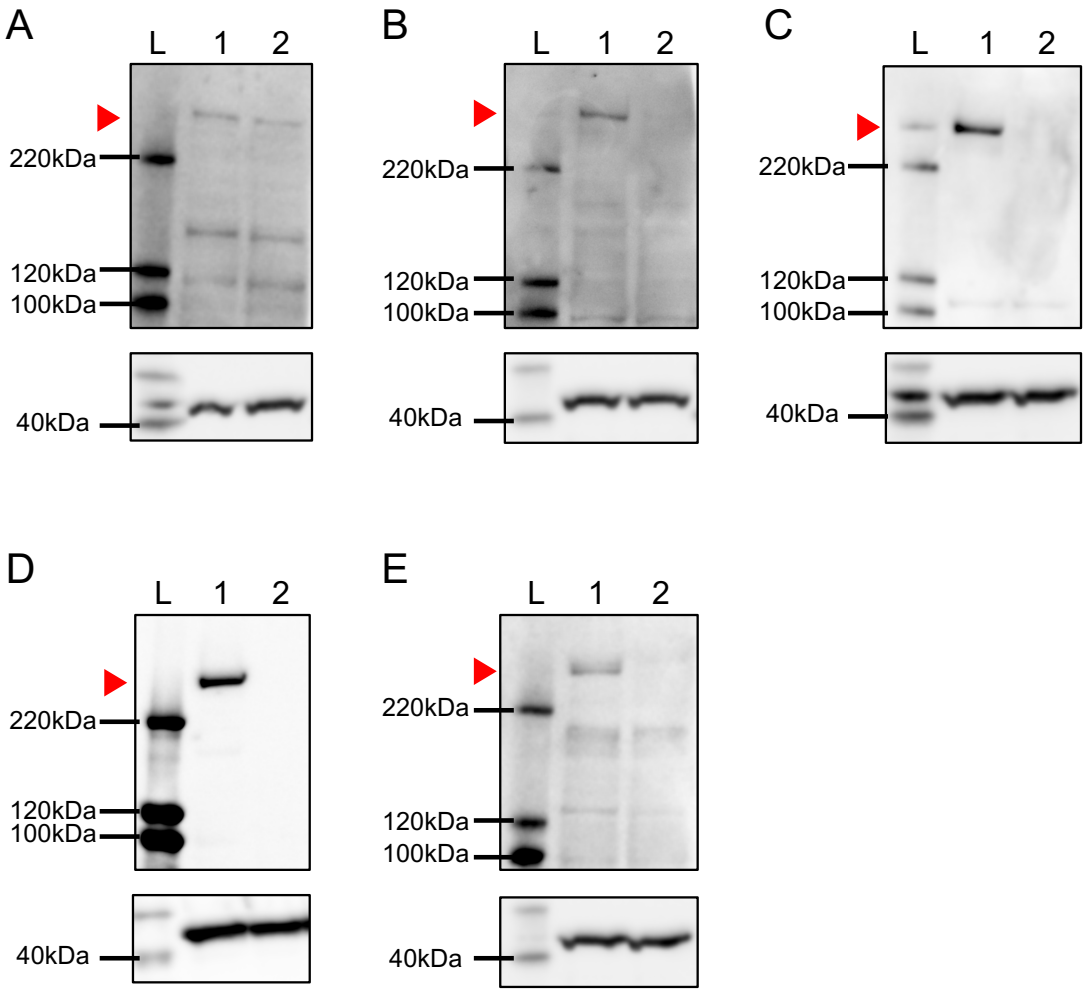

Figure 2.11: HEK 3-KO cells (Alzayady et al., 2016) lack IP_3R2 and IP_3R3 while IP_3R1 results are inconsistent. Lysates (40μg) of HEK WT (1) and HEK 3-KO (2) cell lines were analysed by Western blot. Lysates were blotted using subtype-specific antibodies **(A)** S1, **(B)** Ab1, **(C)** Ab2, **(D)** Ab3 and **(E)** a common antibody that recognises all IP_3R subtypes equally (AbC, 1:1000, Table 2.2). Red arrows indicate position of IP_3Rs. M_r markers (L) and β-actin blots (low panels) are also displayed. Results are representative of three independent experiments (*n* = 3).

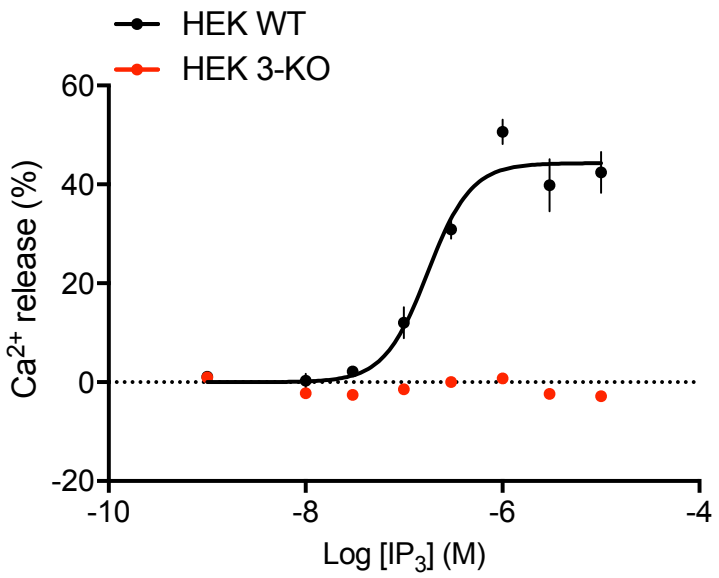

Figure 2.12: HEK 3-KO cells (Alzayady et al., 2016) lack functional IP_3Rs. Concentration-dependent effect of IP_3 on Ca^{2+} release (expressed as % of ER Ca^{2+} content) in permeabilised HEK WT cells. IP_3-evoked Ca^{2+} release is abolished in HEK 3-KO. Data show mean ± s.e.m from four independent experiments (*n* = 4, within a single experiment each concentration was run in triplicates).

Detection of IP_3R1 with S1 in HEK 3-KO was an issue that had to be addressed, despite the evidence that these cells lack IP_3R1. A good indication for the presence of a protein is the presence of its mRNA. It was hypothesised that *itpr1* mRNA would not be detected if cells were successfully edited as the mRNA would contain a premature stop codon leading to the degradation of the transcript by nonsense-mediated mRNA decay (Frischmeyer and Dietz, 1999, Maquat, 2004). Hence, two different primer pairs were used to amplify the C-terminal region of *itpr1* mRNA (Table 2.3). cDNA was synthesised from HEK 3-KO cells and the regions were amplified using RT-PCR. These experiments were carried out collaboratively with Dr. R. Lagos Cabre. Both primer pairs confirm that *itpr1* mRNA is present in the HEK 3-KO cell line **(Figure 2.13)**. Although the presence of mRNA may not correlate with protein expression, the presence of *itpr1* mRNA was a concern.

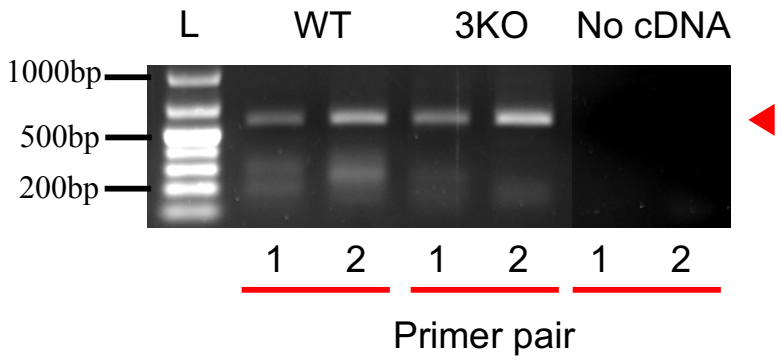

Figure 2.13: HEK WT and HEK 3-KO cells were lysed and mRNA was extracted and then reverse transcribed to cDNA. The cDNA was amplified using RT-PCR with two primer pairs (Table 2.3) that recognise exons 55-59 of the three *itpr1* mRNA variants. RT-PCR amplification was carried out on a cDNA control to ensure there is no contamination. The products of the RT-PCR reaction were run on a 1% agarose gel. The red arrow points to bands corresponding to IP_3R1 (expected fragment size ~600 bp). L is a 1kb DNA ladder. The blot is representative of two independent experiments (*n* = 2). The experiments were obtained in collaboration with Dr R. Lagos Cabre.

The results so far suggest that the Alzayady and colleagues HEK 3-KO cells (Alzayady et al., 2016) lack functional IP_3Rs (**Figure 2.12**), both IP_3R2 and IP_3R3 proteins (**Figure 2.11C & E**), but they provide ambiguous data on whether they express any residual IP_3R1 protein (**Figure 2.11A & B**).

I shared my results with Prof. D. Yule who reported that several antibodies to the C-terminus of IP_3R1 failed to detect significant bands in HEK 3-KO cells, although faint bands of the correct Mr were identified in some cases. Immunoprecipitation using three different antibodies to the C-terminus of IP_3R1 pulled down an IP_3R band in WT cells, but not in HEK 3-KO cells. Hence, I concluded that S1 lacks specificity and that Ab1 is the better antibody to use to identify IP_3R1. Using Ab1, Ab2 and Ab3, I confirmed the lack of expression of IP_3R1, IP_3R2 and IP_3R3 in HEK 3-KO cells (**Figure 2.14A-C**).

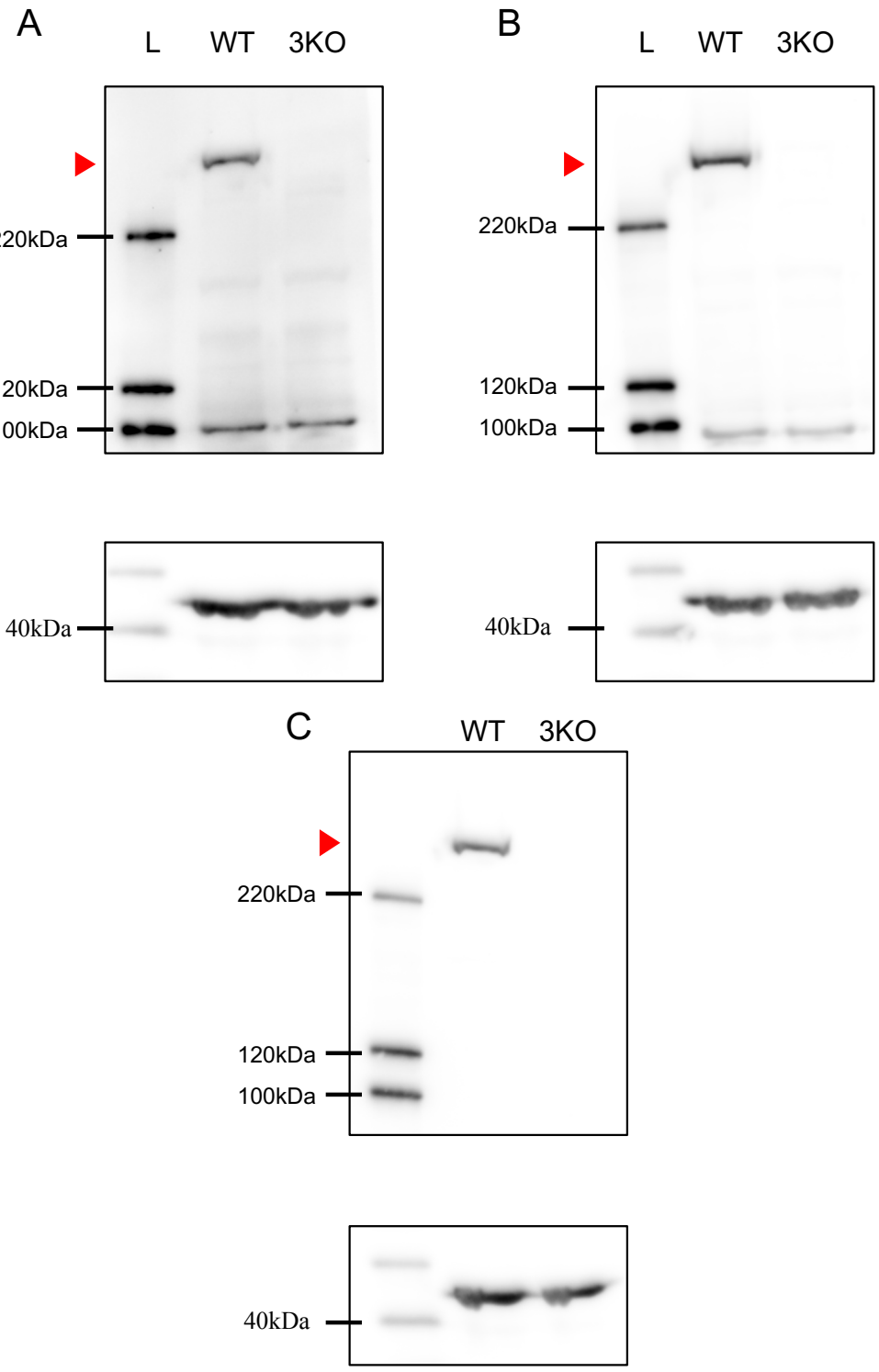

Figure 2.14: HEK 3-KO cells are devoid of IP_3Rs. HEK WT and HEK 3-KO cell lysates (40μg) were blotted using **(A)** Ab1, **(B)** Ab2 and **(C)** Ab3 (Table 2.2). Red arrows indicate position of IP_3Rs. M_r markers (L) and β-actin blots (low panels) are also displayed. Blots are representative of three independent experiments (*n* = 3).

2.3.4 Quantification of IP_3R expression in HEK cells expressing single IP_3R subtypes

An important component of this thesis was to determine whether all three IP_3R subtypes are able to evoke IP_3-mediated Ca^{2+} signals (Chapter 4). The question could be addressed in either cell type expressing single IP_3R subtypes. The choice between cell lines was based on their suitability to analyse Ca^{2+} signals by TIRFM. HAP1 cells in culture grow in patches and the cells are smaller than HEK cells (**Figure 2.15**). For imaging experiments, it is important to distinguish cell boundaries, making HEK cells more suitable. An added benefit of HEK cells is that they are easily transfected and they are cells that have been extensively characterised in terms of their Ca^{2+} signalling (Keebler and Taylor, 2017). For these reasons, optical patch-clamp experiments used HEK cells expressing single IP_3R subtypes.

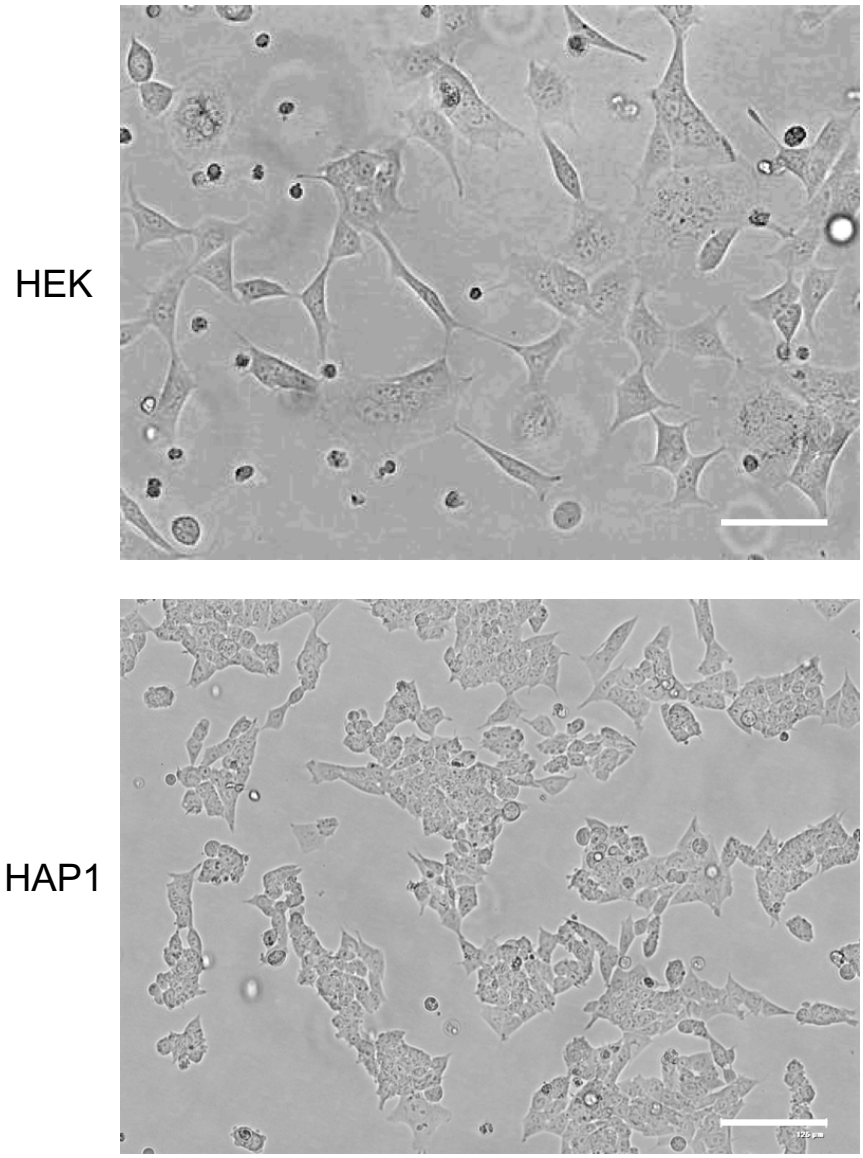

Figure 2.15: HEK WT cells are flatter than HAP1 cells. Brightfield image of HEK WT and HAP1 WT cells in culture. Scale bar 125 μm.

Using antibodies specific for each IP_3R subtype, I verified that HEK WT cells express three IP_3R subtypes (**Figure 2.16A-D**) and that the predominantly expressed subtype was IP_3R3, followed by IP_3R1 and IP_3R2 ($IP_3R3 \geq IP_3R1 > IP_3R2$, **Figure 2.16E**). The expression profile was different to previous analyses using Western blotting (Wojcikiewicz, 1995) or PCR (Tovey et al., 2008). The different expression profile could be attributed to the methods used or to the source of HEK cells. The HEK WT cell line used in this study is that used to generate HEK 3-KO cells by Alzayady et al (Alzayady et al., 2016). Within each cell line expressing a single IP_3R subtype, its expression level was lower than in WT cells **(Figure 2.16F)**. Using an antibody that equally detects each IP_3R subtype (AbC), I show that IP_3R expression in cells expressing a single IP_3R subtype is similar across the three cell lines, but approximately a third lower than in HEK WT cells **(Figure 2.16G)**. A key concern with this type of protein quantification is whether antibodies faithfully report the protein loadings. Plotting the band intensities for each protein loading shows that the intensity of IP_3R bands increases linearly with the concentration of the sample **(Figure 2.17)**. This confirms that IP_3R expression levels in Figure 2.16 are not saturated.

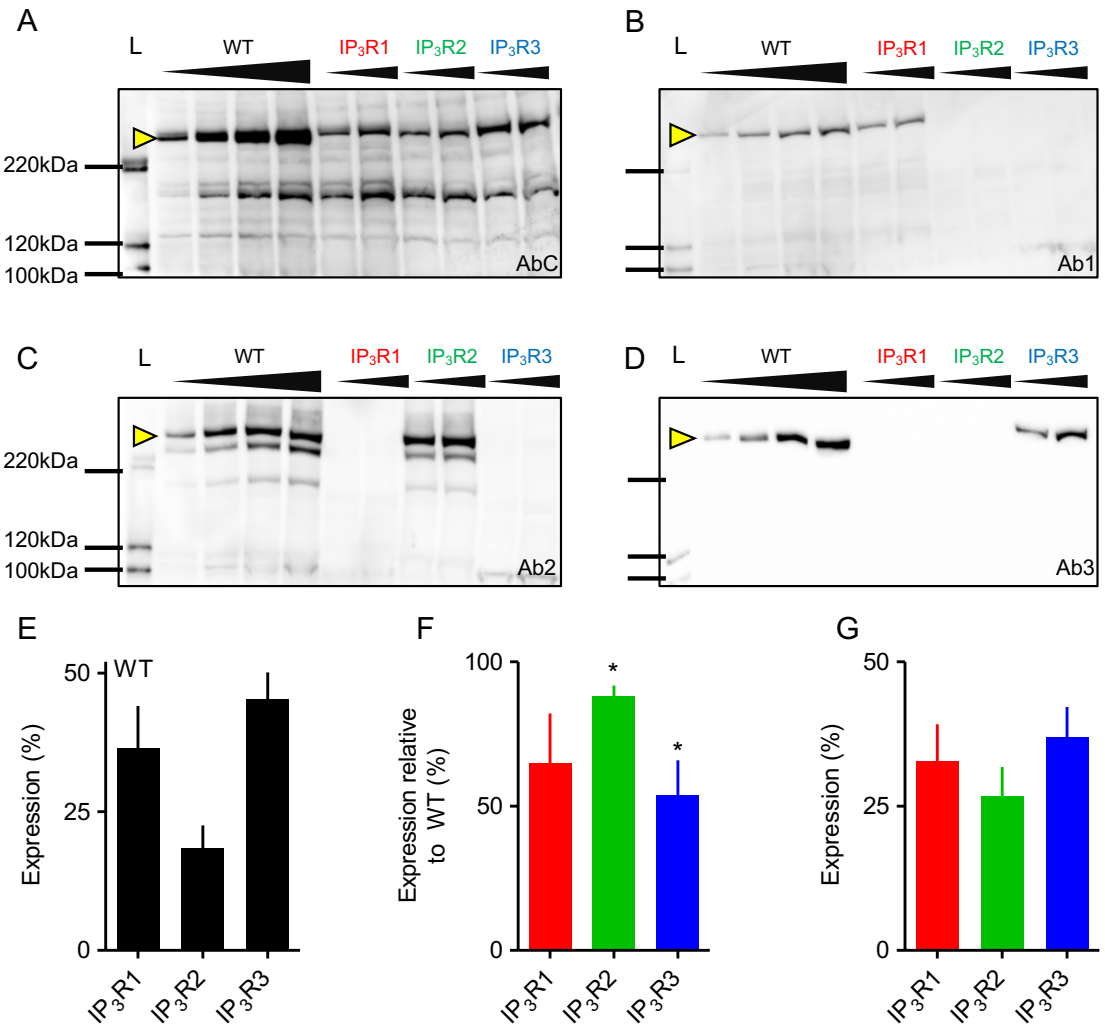

Figure 2.16: Expression of IP_3R subtypes in HEK cells. (A-D) Western blots using IP_3R subtype-selective antibodies (Ab1-3) or a common antibody (AbC). Lanes were loaded with 20, 40, 80 or 120µg protein for WT cells, and 80 or 120 µg for cells expressing a single IP_3R subtype. M_r markers are shown. Arrows show IP_3R bands used for quantification. **(E-F)** Summary results (%, mean ± s.e.m., five independent experiments) (*n* = 5) **(E)** shows relative expression of IP_3R subtypes in WT cells determined by calibrating bands identified with Ab1-3 to bands identified by AbC in lines expressing single IP_3R subtypes. The ratios were used to convert IP_3R subtype-specific bands to AbC intensities from which I estimated the relative expression of each subtype. **(F)** IP_3R expression in cell lines expressing single subtypes relative to the same IP_3R subtype in WT cells. **(G)** the total number of IP_3Rs expressed in each cell line relative to number in WT (by comparing intensities of AbC bands). In (F) *denotes values where the 95% confidence interval does not include 100%. No significant differences (p > 0.05) between values in (G).

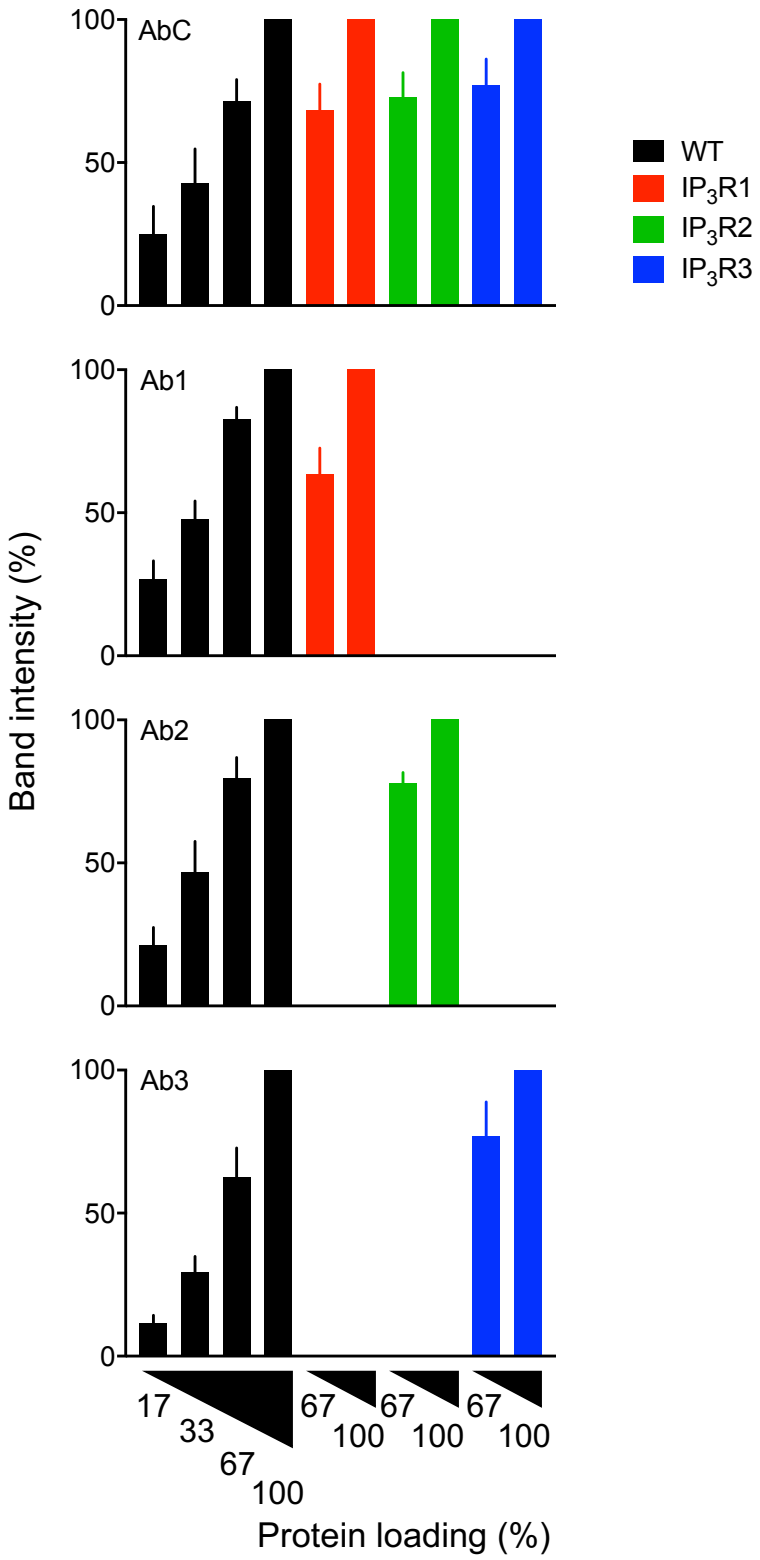

Figure 2.17: Band intensities in Figure 2.16 scale linearly with protein loadings. Protein loadings normalised to maximal loading (120 µg of protein per well = 100%) and band intensities are normalised to maximal loading band intensity. Results show the mean ± s.e.m from five independent experiments (*n* = 5, n=4 for the lowest loading of WT cells).

I also wanted to determine whether there is a difference in the distribution of IP_3R subtypes between cells expressing single IP_3R subtypes. Valid comparisons between cell lines expressing a single IP_3R subtype, require the use of a common antibody. I therefore, used AbC in immunostaining experiments in HEK 3-KO cells and gene-edited HeLa cells in which IP_3R1 has been endogenously tagged with GFP (Thillaiappan et al., 2017) to determine its specificity. However, there is AbC staining in both HEK WT and HEK 3-KO cells (**Figure 2.18A**). In addition, it appears that AbC staining in HEK WT cells is non-specific as we would expect a reticular IP_3R distribution, based on previous reports (Pantazaka and Taylor, 2011). Furthermore, there is no colocalisation of AbC staining and GFP-IP_3R1 fluorescence in HeLa GFP-IP_3R1 cells (**Figure 2.19B**). Based on these analyses, I concluded that AbC lacks specificity in immunostaining experiments, and I was unable to address whether IP_3R distributions differ between HEK cells expressing a single IP_3R subtype.

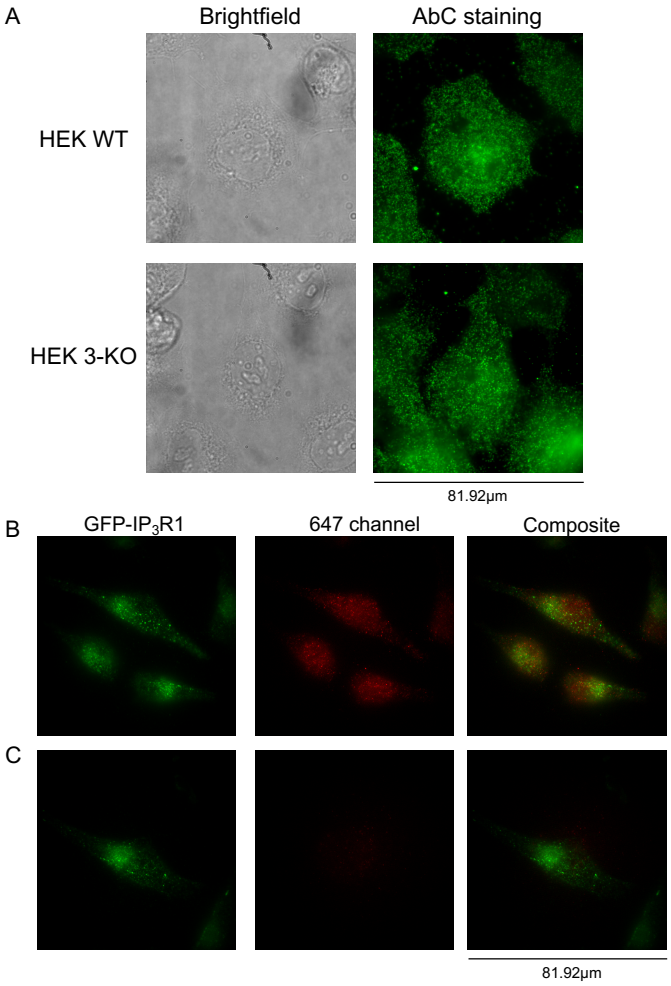

Figure 2.18: AbC appears to be non-specific in immunostaining experiments. (A) HEK WT and HEK 3-KO cells were fixed, permeabilised, incubated with AbC (1:500, overnight, Table 2.2) and then Alexa Fluor 488 conjugated secondary antibody (1:1000, 1h, Table 2.2). Samples were imaged using TIRF (488 laser, 200ms exposure, EM gain 300). Brightfield and AbC staining (representative of three different view fields from a single experiment) are shown for both cell lines. **(B)** Gene-edited HeLa cells endogenously expressing GFP-IP_3R1 (Thillaiappan et al., 2017) were fixed, permeabilised, incubated with AbC (1:500, overnight, Table 2.2) and then Alexa Fluor 647 conjugated secondary antibody (1:1000, 1h, Table 2.2). Samples were imaged using TIRFM (488 and 647 lasers, 100ms exposure, EM gain 300). Images show GFP-IP_3R1 fluorescence, AbC staining (647 channel) and a composite image. **(C)** A similar protocol was followed for panel C, except from incubation with the primary antibody. This shows that the Alexa Fluor 647-conjugated secondary antibody stains specifically. The results are representative of five different view fields from a single experiment (n = 1).

2.4 Conclusions

The aims of this chapter were to establish and/or characterise systems that allow us to better understand the function of IP_3Rs. My attempt to generate HEK293 cells devoid of IP_3Rs was unsuccessful probably because of an unrecognised lack of specificity of S1 for IP_3R1. It is worth noting that the same antibody presented no such problems in DT40 cells, where it recognised an IP_3R1 band only in cells expressing IP_3R1 (Saleem et al., 2012).

In parallel, Horizon Discovery Group used CRISPR/Cas9 to disrupt IP_3R genes in HAP1 cells and so generate cell lines expressing combinations of IP_3Rs, a single IP_3R subtype, and cells devoid of IP_3Rs. I demonstrated, after some difficulties with the S1 antiserum that the HAP1 3-KO cell line expressed no IP_3R proteins and IP_3 did not evoke Ca^{2+} release from intracellular stores. The cells are, however, less suitable for Ca^{2+} imaging than HEK cells.

While my work was in progress, Prof D. Yule's lab reported the use of CRISPR/Cas9 to generate HEK cells lacking all IP_3R subtypes. Both independently and then in collaboration with Prof D. Yule, I have verified that HEK 3-KO cells express no IP_3R proteins and they fail to release Ca^{2+} in response to IP_3. The results from Prof D. Yule's lab overtook my studies and prompted me to use his cells rather than investing further effort in developing my own.

Finally, an important component of this Chapter was to determine whether HEK WT from Prof. D. Yule expressed all three IP_3R subtypes and their relative expression levels ($IP_3R3 \geq IP_3R1 > IP_3R2$). In addition, HEK cells expressing a single IP_3R subtype were shown to only express their cognate IP_3R and their total IP_3R levels were about a third lower than WT cells. The four cell lines, HEK WT, HEK IP_3R1, HEK IP_3R2 and HEK IP_3R3 are used in the work described in Chapter 4 to determine whether Ca^{2+} puffs are the universal building blocks of Ca^{2+} signals.

Chapter 3: Validation of Flika, a python-based programme that automatically detects and analyses IP_3-evoked Ca^{2+} signals.

3.1 Introduction

3.1.1 Optical patch-clamp as a method to simultaneously monitor Ca^{2+} events from multiple channels

Our increasing knowledge of the hierarchical components of IP_3-evoked Ca^{2+} signalling has been driven by advances in optical technologies. Earlier Ca^{2+} imaging experiments used widefield imaging to study global Ca^{2+} transients in *Xenopus laevis* oocytes (Brooker et al., 1990) and to some extent local Ca^{2+} events (Parker and Yao, 1991). The development of TIRFM (Axelrod et al., 1984, Axelrod, 2001) and the discovery that the majority of IP_3-evoked Ca^{2+} events occur near the PM (Smith et al., 2009a, Thillaiappan et al., 2017, Ellefsen and Parker, 2018) revolutionised the field as it enabled visualisation of IP_3-evoked Ca^{2} events (including single-channel events) at a high temporal resolution using TIRFM (up to 2ms per frame) (Wiltgen et al., 2014, Wiltgen et al., 2010, Ellefsen and Parker, 2018).

The optical patch-clamp (Parker and Smith, 2010) method uses a TIRF microscope, a Ca^{2+} indicator (Cal-520) and a Ca^{2+} buffer to restrict the diffusion of Ca^{2+} (EGTA). This method, paired with the use of a cell-permeable IP_3 analogue, enable the direct stimulation of IP_3Rs and visualisation of IP_3-evoked Ca^{2+} signals. I will now discuss the experimental components needed to visualise IP_3-evoked Ca^{2+} signals in live cells.

The first component needed for optical patch-clamp experiments is a TIRF microscope. Although TIRFM for cell biology had been described since 2001 (Axelrod, 2001), it became more widely used recently. This is attributed to the development of TIRF objectives and the commercial availability of TIRF microscopes (Sanderson et al., 2014). The principles of TIRF were discussed in

section 1.3, so I will now focus on the remaining experimental components needed for optical patch-clamp experiments.

Tsien and his colleagues used the BAPTA structure, a Ca^{2+} buffer, as a backbone for the rational design of fluorescent Ca^{2+} indicators. These are fluorescent probes that undergo a significant fluorescence enhancement (quin-2) or spectral shift upon binding Ca^{2+} (fura-2 and indo-1) (Tsien, 1980, Paredes et al., 2008). Ca^{2+} indicators have a Ca^{2+}-binding region, which contains several anionic carboxyl groups that enable Ca^{2+} binding and a fluorescence region that confers spectral properties (Tsien, 1980). Quin-2 was the prototype for single-wavelength indicators, but there are now many sensors that differ in Ca^{2+} affinity, special properties and in the extent to which they are retained within the cytosol (fluo-8 and Cal520 are some examples).

Imaging of Ca^{2+} puffs at high temporal resolution requires indicators with specific properties:

- Firstly, they require an appropriate K_d for Ca^{2+}, ideally somewhere close to the global $[Ca^{2+}]_c$ changes evoked by IP_3 (Paredes et al., 2008, Bootman et al., 2014).
- Secondly, the indicator needs fast kinetics to faithfully report IP_3-evoked Ca^{2+} signals (Lock et al., 2015b).
- Thirdly, the indicator needs to be single wavelength to allow fast ci-IP_3 uncaging without the need to switch between wavelengths.
- Fourthly, it needs to be compatible with the use of ci-IP_3.
- Fifthly, it needs to have fluorescent properties that do not require use of excitation wavelengths that cause cell damage.
- Sixthly, it needs to be bright enough to allow accurate recordings without overloading the cytosol.
- Lastly, it needs to be retained in the cytosol.

Amongst presently available Ca^{2+} indicators, Cal-520 (K_d for Ca^{2+} 320nM; λ_{ex} 492nm and λ_{em} 514nm) best fulfils the aforementioned criteria (Lock et al., 2015b). Hence, I have used Cal-520 for my analyses of IP_3-evoked Ca^{2+} signals. As Cal-520 is unable to cross the PM, I have used an acetoxymethyl ester (AM) derivative of the indicator, Cal-520-AM. The AM derivative masks the overall

charge of the molecule and enables non-invasive delivery of the compound into cells. Non-specific esterases in the cytosol cleave the ester groups and trap the indicator in the cytosol (Li et al., 1997).

An exogenous Ca^{2+} buffer, EGTA, has been used in optical patch-clamping to restrict diffusion of Ca^{2+} ions (Shuai and Parker, 2005, Smith and Parker, 2009, Smith et al., 2009a, Wiltgen et al., 2010, Parker and Smith, 2010, Lock et al., 2017). EGTA has a relatively slow (compared to BAPTA for example) on-rate (3-10$\mu M^{-1}s^{-1}$) for Ca^{2+}. EGTA's on-rate is too slow to inhibit CICR between IP_3R channels in a single cluster, where distances are of the nanometer scale, but it is fast enough to bind Ca^{2+} ions diffusing over micrometer distances. Hence, Ca^{2+} ions diffusing from a cluster of IP_3Rs to a neighbouring IP_3R cluster will bind to EGTA instead of activating neighbouring receptors. As a result, Ca^{2+}-release sites act autonomously to generate local Ca^{2+} transients, while the functional coupling of different IP_3R clusters is disrupted to delay or inhibit global Ca^{2+} signals (Dargan and Parker, 2003). In the presence of EGTA, Ca^{2+} puffs are more transient and with their spatiotemporal profiles slightly sharpened (accelerated time course and decreased spatial spread), while there are no effects on the amplitude (Callamaras and Parker, 2000, Shuai and Parker, 2005, Smith et al., 2009a, Smith and Parker, 2009, Wiltgen et al., 2010) (**Figure 3.1**). I used the membrane-permeable derivative of EGTA (EGTA-AM) in my experiments to determine individual puff properties.

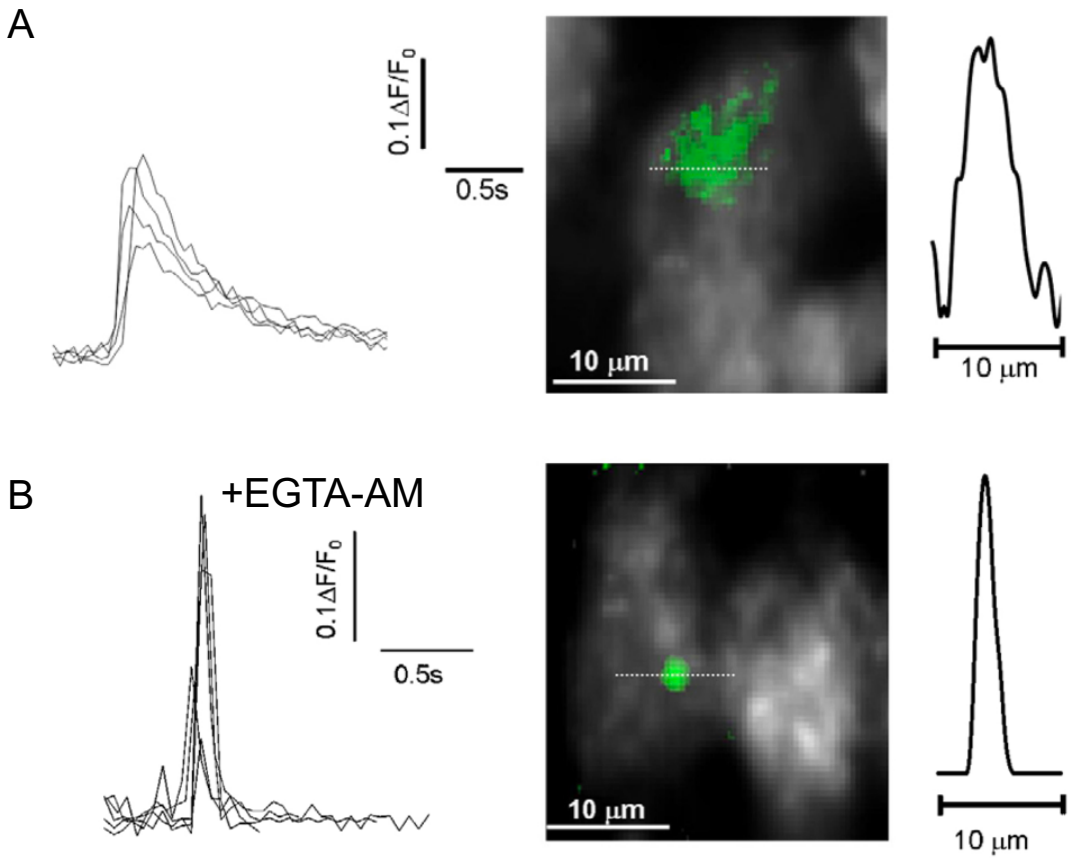

Figure 3.1: EGTA sharpens the spatial profile of IP_3-evoked Ca^{2+} puffs. Illustrates local and Ca^{2+} signals evoked by flash photolysis of ci-IP_3 in SH-SY5Y cells loaded with fluo-4-AM. Superimposed puff traces and spatial profile of Ca^{2+} puffs recorded using optical patch-clamp at their peak amplitude in **(A)** the absence and **(B)** presence of EGTA-AM. The figure is reproduced from Smith et al. (2009).

The study of IP_3-evoked Ca^{2+} signals requires direct activation of IP_3Rs by IP_3 or IP_3 analogues, with defined temporal resolution. Since IP_3 is a hydrophilic molecule (negative charge), it is unable to cross the hydrophobic PM. To enable non-invasive delivery of IP_3 into cells, researchers have developed lipophilic esters and analogues of IP_3 that mask the molecule's negative charge and enable it to cross the PM. Ci-IP_3/PM is a caged, cell-permeable derivative of IP_3 that is metabolically more stable. The cell permeability of ci-IP_3/PM is conveyed by the propionyloxymethyl groups that mask the three phosphate groups of IP_3 (**Figure**

3.2A). The propionyloxymethyl groups are cleaved by non-specific esterases in the cytosol, leading to entrapment of the compound within the cytosol. At this stage ci-IP_3 is inactive and has minimum binding affinity for the IP_3R (**Figure 3.2B**). The 2- and 3- hydroxyl groups of ci-IP_3 are protected by an isopropylidene group, and the 6-hydroxyl group, which is essential for binding to the IP_3R, is protected by a photolabile 'cage' (DMNB, 4,5-dimethoxy-2-nitrobenzyl). The DMNB group provides temporal control for activating IP_3Rs as UV illumination can photolyse the DMNB group and render i-IP_3 active (Li et al., 1998, Dakin and Li, 2007) (**Figure 3.2C**). The active compound can engage the IP_3R and induce Ca^{2+} release from the ER.

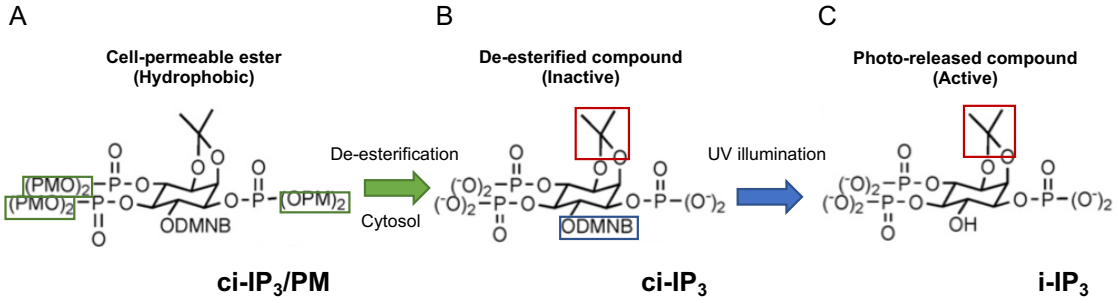

Figure 3.2: Conversion of ci-IP_3/PM to i-IP_3. (A) The inactive and cell-permeable derivative of IP_3, ci-IP_3/PM. The propionyloxymethyl groups are cleaved by non-specific esterases in the cytosol (shown in green). **(B)** The de-esterified compound, ci-IP_3, is trapped in the cytosol. The isopropylidene group (in red) and the DMNB group (in blue) are highlighted. **(C)** The DMNB group is photolysed by UV light to render the active compound, i-IP_3. The figure is reproduced from Dakin and Li (2007).

3.1.2 Algorithms that automate detection of Ca^{2+} events

To be able to determine puff kinetics, it is necessary to record Ca^{2+} signals at a high temporal resolution (~5ms/frame). Imaging at this frame rate results in recordings of considerable size (12,000 images per minute, which is equal to ~400MB of data when imaging a region of 120x120 pixels). The vast amounts of data make manual analysis of Ca^{2+} puffs extremely difficult and prone to user bias (e.g. small events might be missed). Therefore, analysis of IP_3-evoked Ca^{2+}

signals requires an algorithm/program that automates the detection and analysis of these signals (Lock et al., 2015a, Keebler and Taylor, 2017).

The first programmes developed were specifically designed to automatically detect Ca^{2+} sparks; they include SparkSpotter and XYSpark (Steele and Steele, 2014). The spatiotemporal differences, however, between Ca^{2+} puffs and Ca^{2+} sparks, render these programmes unfit for analysis of IP_3-evoked Ca^{2+} signals. Indeed, part of Dr M. Keebler's thesis was devoted in comparing these two programmes with his custom-made IDL algorithms, PuffMapper and SiteMapper. The head-to-head comparison of the different programmes was carried out by automatically analysing IP_3-evoked Ca^{2+} signals in HEK293 cells stimulated with 10μM CCh. He showed that his algorithm was superior in recognising 'true' Ca^{2+} events (Keebler, 2015).

Unfortunately, the IDL algorithm developed by Keebler (Keebler and Taylor, 2017) lacks a graphical user interface, and as a result, its use requires IDL coding experience. Additionally, PuffMapper and SiteMapper were optimised for a specific capture rate (40ms) and specific experimental conditions. The 40ms capture rate is not fast enough for high-resolution analysis of Ca^{2+} puffs. Hence, PuffMapper and SiteMapper are unsuitable for my analyses.

Kyle Ellefsen from Ian Parker's group published a python-based threshold program, Flika, for the detection of Ca^{2+} events in 2014 (Ellefsen et al., 2014). Flika is based on a threshold-cluster algorithm (Rodriguez and Laio, 2014). To locate clusters, the programme identifies pixels exceeding a user-specified threshold, and compares them to neighbouring pixels. In 2017, the newer version of Flika (https://github.com/flika-org/flika) was made available online, with a greatly improved graphical user interface that resembles that of Fiji (Schindelin et al., 2012). The new version is extremely user-friendly to users with no coding experience. Therefore, the work described in this Chapter and Chapter 4 has been carried out using the Flika program.

3.1.3 Aims of this Chapter

The aims of the work described in this chapter were:

1. To set up Flika program for detection of IP_3-evoked Ca^{2+} signals in HEK cells.
2. To compare puff detection between Flika program and manual analysis.

3.2 Materials and Methods

3.2.1 Materials

Cal-520-AM was from Stratech Scientific (Suffolk, UK). EGTA-AM was from Merck Millipore (Darmstadt, Germany). ci-IP_3/PM was from SiChem GmbH (Bremen, Germany). Glass-bottomed dishes (P35GC-1.5-14-C) were from MatTek (Ashland, MA, USA). Stock solutions of 10mM EGTA-AM and 2mM ci-IP_3/PM were prepared in DMSO and stored at -20°C. Sources of additional materials are provided in Chapter 2.

3.2.2 Cell culture

HEK WT cells were maintained as described in section 2.3.1. For imaging, $5x10^4$ cells were seeded on poly-L-lysine-coated (10µg/ml) 35mm glass-bottomed dishes. Prior to imaging, cells were maintained for 48h at 37°C, in a humidified atmosphere of 95% air and 5% CO_2. Cells were used when sub-confluent (typically covering 50% of dish) to allow individual cells to be clearly resolved.

3.2.3 High-resolution imaging of Ca^{2+} signals by TIRFM

To record local Ca^{2+} signals, cells were loaded with a cytosolic Ca^{2+} indicator (Cal-520), a caged analogue of IP_3 (ci-IP_3) and an exogenous Ca^{2+} buffer (EGTA) to restrict diffusion of Ca^{2+} ions (Smith et al., 2009a, Parker and Smith, 2010, Lock et al., 2015a).

Cells were firstly checked under the microscope to ensure they were sub-confluent. Immediately after, they were washed twice in HBS and incubated in the dark in HBS containing 0.02% w/v pluronic acid F-127, which increases the solubility and uptake of AM esters, 5µM Cal-520-AM and 1µM of ci-IP_3/PM. To

ensure there is no compartmentalisation of dye, all loading steps were carried out at room temperature (~20°C). After 1h, cells were washed to remove excess dye and ci-IP_3-PM and incubated for 45min with HBS containing pluronic acid F-127 and 5μM EGTA-AM. The cells were then washed and incubated for 30min in HBS to allow de-esterification of compounds in the cytosol. HBS was replaced with new HBS, immediately before imaging to ensure there was no leaked dye in the extracellular medium. Although, dye leak and/or compartmentalisation are drawbacks associated with the use of some Ca^{2+} indicators, there is no evidence of this occurring with Cal-520 (Lock et al., 2015b). To minimise any risk of compartmentalisation of the indicator, dishes were immediately used in experiments and experiments were of short duration (less than 1h). Additionally, there were no signs of indicator compartmentalisation when cells were observed under the microscope.

Dishes were mounted and immobilised, to prevent lateral movement during recordings, on the stage of an inverted Olympus IX83 microscope equipped with a 100x oil-immersion TIRF objective (Olympus UApo N; numerical aperture, NA 1.49), a multi-line laser bank (395nm, 425nm, 488nm, 561nm and 647nm) and an iLas2 targeted laser illumination system (Cairn, Faversham, Kent, UK). Cal-520 excitation was achieved by a 488nm diode-pumped solid-state laser (150mW) transmitted through a band-pass filter (ET-405/488/561/643 quad band filter set, Chroma). Emitted light was passed through a band-pass filter (Cairn Optospin, peak/bandwidth 525/50 nm) and captured by an Andor iXon 897 EMCCD camera (512 x 512 pixels, 16μm x 16μm per pixel; such that with a 100x objective, each pixel was 160nm x160nm). To achieve high temporal resolution (~188Hz), images were captured from a portion of the cytoplasm of a single cell (recording area: 120 x 120 pixels, 19.2μm x 19.2μm) and streamed directly into the computer's RAM. Images from a single recording were visualised as a stack on Metamorph (Molecular Devices, Sunnyvale, CA, USA) and saved as a tif file. Images were captured by TIRFM for 40s before and after flash photolysis of ci-IP_3, at a penetration depth of ~90nm. Photolysis of ci-IP_3 within the entire imaging field was achieved using a light-emitting diode (LED, 395 nm, SPECTRA X-light engine, Lumencor, Beaverton, OR, USA) with an exposure time of 50ms.

3.2.4 Manual detection of Ca^{2+} signals

Manual identification of IP_3-evoked Ca^{2+} signals was carried out in Fiji (Schindelin et al., 2012). Graphs were drawn using Prism 6 software.

3.2.5 Detection and analysis of Ca^{2+} events using Flika

Each recording was loaded on the Fiji programme (Schindelin et al., 2012). Every pixel was then background-corrected by subtracting the average fluorescence of a region of interest (ROI) outside the cell. I manually verified that prior to ci-IP_3 photolysis, there were no IP_3-evoked Ca^{2+} puffs (40s). Each stack was then truncated to keep the last 500 frames (~2.7 s) before flash photolysis and to remove the UV flash.

The truncated stack containing the pre- and post-flash images was loaded on Flika, a python-based program designed to automatically detect and analyse IP_3-evoked Ca^{2+} signals (Ellefsen et al., 2014). Steps one to three (image pre-processing) were performed using Flika's graphical user interface, and steps four to nine were performed using Flika's detect_puffs plugin. The steps I describe were adapted from (Ellefsen et al., 2014):
http://htmlpreview.github.io/?https://github.com/kyleellefsen/detect_puffs/blob/master/docs/How%20to%20detect%20subcellular%20Ca2%2B%20signals%20using%20Flika.html and
https://github.com/kyleellefsen/detect_puffs/blob/master/docs/detect_puffs_parameters.md.

1. **Generation of the 'F/F_0' stack:** The fluorescence intensity of each pixel was averaged across the first 500 frames (resting fluorescence) to generate a new F/F_0 image. For each slice in the frame, the fluorescence intensity of each pixel (F) was divided by its average fluorescence intensity prior to flash photolysis (F_0). This yielded a new F/F_0 stack, in which the average fluorescence intensity of each pixel is 1 before the flash and only marginally higher afterwards (since puffs occur relatively rarely at each pixel). This calculation corrects for uneven dye loading.

2. **Generation of the 'Normalised' stack:** To enable detection of Ca^{2+} puffs, a new stack had to be generated in which the average fluorescence

intensity of each pixel is equal to 0 with an s.d. equal to 1. To arrive at a baseline of 0, the value 1 was subtracted from each pixel in the stack. To arrive at an s.d. equal to 1, each pixel was divided by its average s.d. prior to the UV flash.

3. **Generation of the 'Gaussian' stack:** Each frame was blurred by using a Gaussian function. Gaussian smoothing works by spatial averaging of neighbouring pixels. This generates a new stack with an increased signal-to-noise ratio, which is used for the detection of Ca^{2+} events (**Figure 3.3**).

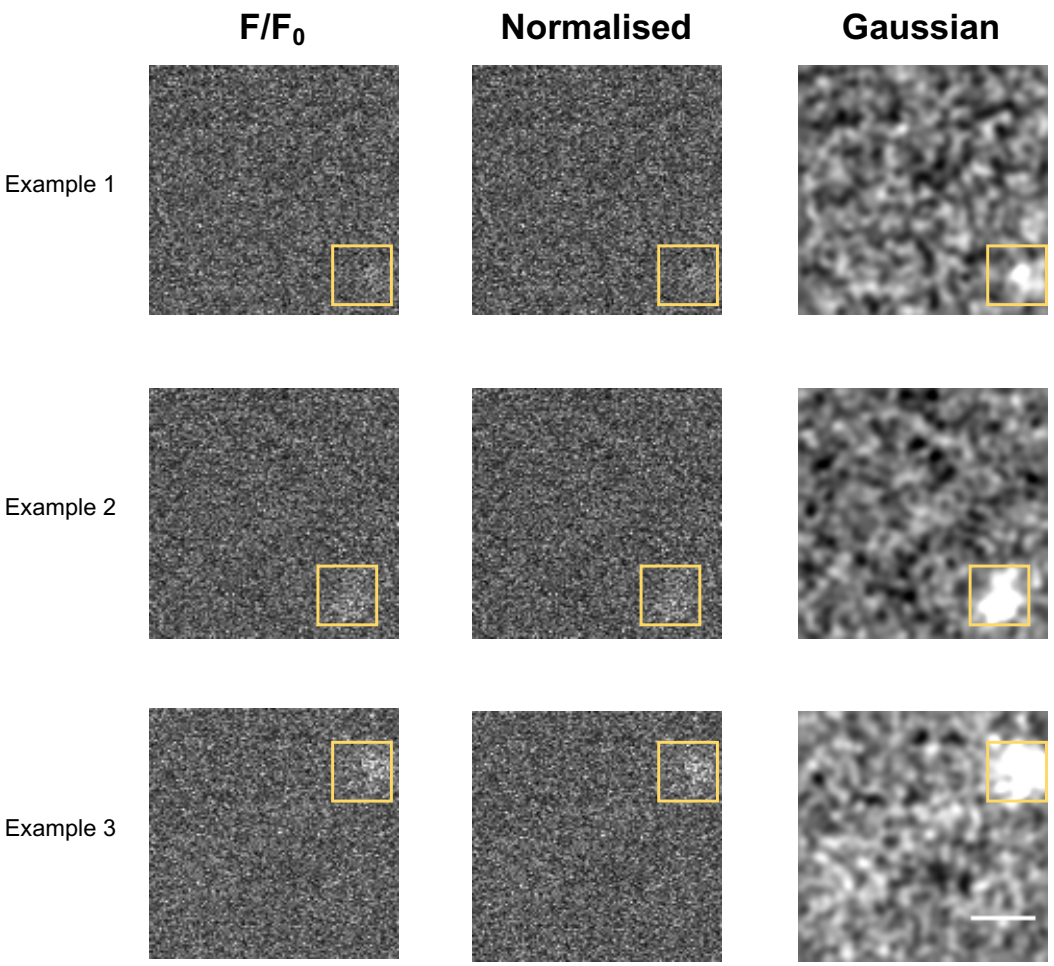

Figure 3.3: Image pre-processing for automatic detection of Ca^{2+} signals by Flika. Automated analysis using the Flika software requires the generation of three image stacks ('F/F_0', 'Normalised' and 'Gaussian'). Each stack has special properties. In the F/F_0 stack, the mean is centred around 1. In the Normalised stack the mean of each pixel is centred around 0 with an s.d. of 1. In the Gaussian stack, neighbouring pixels are filtered using a Gaussian function. Three different puff examples (in the yellow box) are presented (smallest event in the top and largest in the bottom) to show how image pre-processing increases the signal to noise ratio in the transformed images. Scale bar (applies to all images) = 5μm.

The remaining steps are carried out on Flika's detect_puffs plugin. Although, steps five to seven are described separately, they are performed seamlessly.

4. **Frame-by-frame thresholding of pixels:** This step applies a user-specified threshold to the Gaussian-filtered image and identifies, frame-by-frame, pixels exceeding this value. The programme scans every image on the Gaussian stack, pixel-by-pixel, and constructs a Boolean x,y,t matrix. Pixels exceeding the threshold are given a 'TRUE' value on the Boolean matrix, and will go through to the next step. The value needs to be low enough to ensure that even the smallest events are identified, and high enough to exclude pixels that do not belong to a Ca^{2+} event. Such 'false-positive' pixels would dramatically increase the computation time for the next step and Step 9 (manual inspection). When I started the analysis, I chose a higher threshold value (1.4) and determined that only large events were detected. Therefore, I worked my way down to identify the value that would allow me to detect even the faintest of events (0.85). In the end, I chose to set this value to 0.8, to ensure that I did not miss any small events in my analysis.

5. **Identification of cluster centres:** Pixels exceeding 0.8 in the Gaussian stack proceed through the threshold-cluster algorithm (Rodriguez and Laio, 2014) to identify Ca^{2+} puffs and their spatial and temporal extent. This particular threshold-cluster algorithm is based on two assumptions; that cluster centres will be surrounded by multiple pixels of lower value (this is defined as density) and that they will be far from other candidate cluster centres (more than 3μm). For each pixel, Flika identifies the near brighter pixel. In a Ca^{2+} puff, many pixels (high density) point to a single brightest pixel, which is the centre of the cluster. Pixels that point to the same brighter pixel (in the same frame) are considered to be part of the same cluster.

6. The pixels identified in Step 5 are seamlessly grouped together in space and time based on user-defined values. The first value groups together pixels that are located within 3μm of one another. K. Ellefsen has set this

parameter equal to 3.3μm (Ellefsen et al., 2014), which is reasonable as large events may have a diameter of ~3μm. Hence, in my analysis I set this value equal to 3μm. The second value is dependent on the frame-rate of the analysed recording. Setting a value that is too low will affect puffs with a long duration, as they will get broken down into multiple events. Taking into account that multiple events can occur in the same site (these may be separated only by a few milliseconds), a value that is too high might group separate Ca^{2+} events together into one event. I set this value equal to 9, as Ca^{2+} events were clustered appropriately after I ran the program. For each cluster, Flika identifies the start and end frame of the event within 100 frames before and 100 frames after the detection frame.

7. The Ca^{2+} events comprising less than 14 pixels in x,y,t were considered to be artefacts and were removed from the analysis. This is consistent with the user-specified values used in Ellefsen et al. (2014).

8. The programme then creates three-dimensional boxes (x,y,t) around each event. The x,y dimensions of the box were set to 1.76μm x 1.76μm and the temporal dimension began with the start of the event and ended at the termination of the event. The values of each pixel within the box were averaged for each frame, and a 2D Gaussian was fitted to locate the centres of Ca^{2+} puffs. This will determine the x,y coordinate of the centroid of the puff with sub-micrometer resolution. Additionally, average pixel intensities for each frame within the box are used to generate F/F_0 traces.

9. **Manual inspection:** At this stage, all Ca^{2+} puffs have been detected and are manually inspected. This allows the user to delete false positives from the analysis. The start and end of an event is manually curated by simultaneously looking at the F/F_0 traces and the F/F_0 stack.

10. **Extraction of puff properties:** Flika extracts individual puff properties and F/F_0 traces, on an Excel sheet, and groups them according to sites. Events whose centroids are less than 0.96 μm apart are linked into the same site. **Table 3.1** lists the properties of Ca^{2+} events that are extracted from Flika.

Property	
Group #	Identity number of a Ca^{2+} site.
GroupX	x-location of a Ca^{2+} site in pixels.
GroupY	y-location of a Ca^{2+} site in pixels.
Number of events	Number of Ca^{2+} events grouped in that specific site.
Max Amplitude	The maximal Ca^{2+} event amplitude detected at a particular site.
X	x-location of a Ca^{2+} event in pixels.
Y	y-location of a Ca^{2+} event in pixels.
T_peak	Frame on which the peak amplitude of a Ca^{2+} event is detected.
Amplitude	Peak amplitude of a Ca^{2+} event.
R20	Time (in frames) for a Ca^{2+} event to rise to 20% of its peak amplitude.
R50	Time (in frames) for a Ca^{2+} event to rise to 50% of its peak amplitude.
R80	Time (in frames) for a Ca^{2+} event to rise to 80% of its peak amplitude.
R100	Time (in frames) for a Ca^{2+} event to rise to 100% of its peak amplitude.
F80	Time (in frames) for a Ca^{2+} event to fall from its peak amplitude to 80% of its peak amplitude.
F50	Time (in frames) for a Ca^{2+} event to fall from its peak amplitude to 50% of its peak amplitude.
F20	Time (in frames) for a Ca^{2+} event to fall from its peak amplitude to 20% of its peak amplitude.
F0	Time (in frames) for a Ca^{2+} event to fall from its peak amplitude to baseline.

Table 3.1: List of puff properties extracted from the Flika programme. Amplitudes are calculated from the F/F_0 stack and Ca^{2+} event kinetics from the Normalised stack. Adapted from Ellefsen et al. (2014) and Lock et al. (2015a).

The average unitary step (0.101±0.002) during the decay of *n* = 10 Ca^{2+} signals was used to determine the number of active IP_3R in a cluster.

Number of active channels = $\frac{Amplitude\ (\Delta F)}{Unitary\ fluorence\ (0.101)}$.

$\Delta F = F_{peak} - F_{pre}$, where F_{peak} is the F/F_0 value determined at the peak of the Ca^{2+} puff and F_{pre} is the average F/F_0 value is the from the same region ten frames before and ten frames after the puff.

Equation 1 was used to calculate the duration at half-maximal amplitude, **Equation 2** was used to calculate the rise time (time for a Ca^{2+} event to rise from 20% of its peak amplitude to peak amplitude) and **Equation 3** was to calculate the falling time (time for a Ca^{2+} event to fall from peak amplitude to 20% of its peak amplitude).

Equation 1

Duration at half-maximal amplitude = (R100-R50+F50)*5.32ms (**Table 3.1**)

Equation 2

Rising time = (R100-R20)*5.32ms (**Table 3.1**)

Equation 3

Falling time = F20*5.32ms (**Table 3.1**)

3.3 Results and discussion

Flika has been successfully validated using synthetic data (Ellefsen et al., 2014) and used for the automated detection of IP_3-evoked Ca^{2+} puffs in several publications (Ellefsen et al., 2014, Lock et al., 2015a, Lock et al., 2015b, Ellefsen and Parker, 2018). Although, Flika has been shown to faithfully report the location and properties of IP_3-evoked Ca^{2+} events in SH-SY5Y cells, it has not been validated in HEK cells.

Before using Flika in Chapter 4, it had to be validated. The Flika user-specific settings and the rationale for choosing these specific values were discussed in section 3.2.5. Automatic detection of IP_3-evoked Ca^{2+} events in HEK WT cells following flash photolysis of ci-IP_3 was compared to manual detection of Ca^{2+}

puffs. Flash photolysis of ci-IP_3 in HEK WT cells evoked a flurry of Ca^{2+} puffs, and eventually Ca^{2+} signals propagated to the whole cell **(Figure 3.4)**. This observation is similar to observations made in different cell types (Bootman et al., 1997a, Kasai et al., 1993, Marchant and Parker, 2001, Rooney et al., 1990).

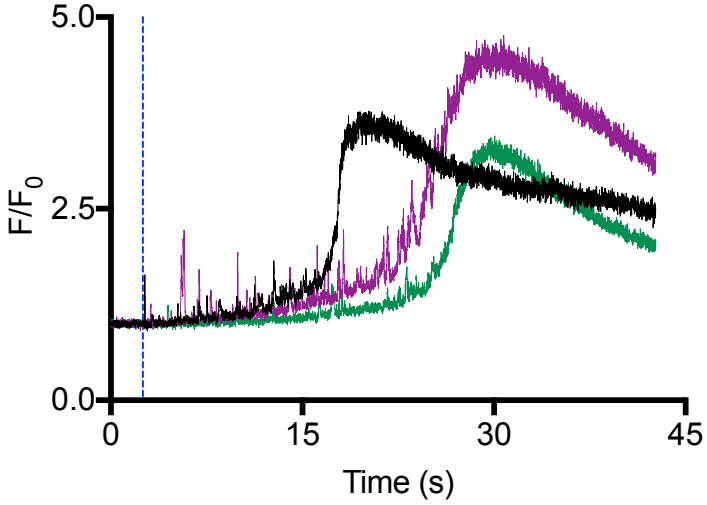

Figure 3.4: HEK WT cells experience global Ca^{2+} signals following flash photolysis of ci-IP_3. The graph shows F/F_0 values from an active (puff events were manually identified) 1.76 x 1.76μm region for three cells, with each cell coloured differently. The dashed blue line shows the time when flash photolysis of ci-IP_3 occurred.

Global Ca^{2+} signals that invade the whole cell interfere with the detection of local Ca^{2+} signals. Therefore, HEK WT cell recordings were manually truncated, by excluding from the analysis all subsequent frames after a 10% increase in baseline ($\geq F/F_0$ 1.1). The rationale for excluding puffs after the baseline had increased by 10% was that the number of open channels reported for each puff would be significantly underestimated. For example, a puff consisting of five active channels would have been reported as a puff consisting of four active channels. The author of the algorithm suggests using a low-pass filter, such as a Butterworth filter, to remove global signals from the Normalised and Gaussian-filtered stacks. Butterworth-filtering would remove the slow increase in baseline fluorescence (global signals), while keeping the fast elevations in baseline fluorescence (local Ca^{2+} signals). This type of filtering would increase the window

of detection for local Ca^{2+} signals, but would not solve the problem of underestimating the number of open channels in a Ca^{2+} event. The issue would remain, because the amplitudes of Ca^{2+} signals detected by Flika are calculated from the F/F_0 stack, which would be unfiltered.

Flika was initially validated, in six HEK WT cells. 200 frames from each cell were randomly selected to ensure that Flika was validated for events that occurred immediately after flash photolysis of ci-IP_3, events that occurred in the middle of the recording and events occurring near the end of the recording. This was done to ensure that Flika identified Ca^{2+} events throughout the duration of the recording. The total number of events reported by Flika was similar to the number of events identified by manual detection **(Figure 3.5)**. The minor differences in the events identified were attributed to events initially missed by manual inspection because they were too small to identify. The small events identified by Flika were validated manually to confirm they were true events.

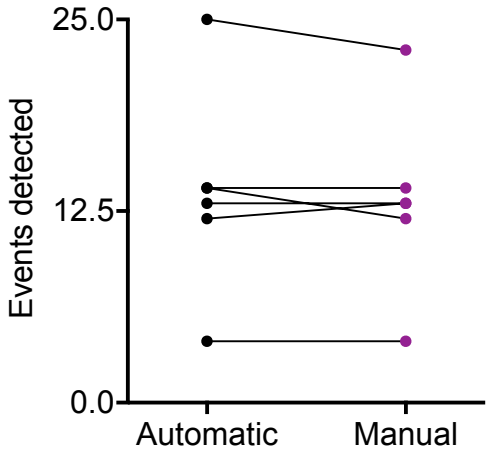

Figure 3.5: Flika faithfully detects Ca^{2+} puffs in HEK WT cells. A single random 200-frame part of the recording was chosen for each cell (*n* = 6 cells). For *n* = 2 cells, these 200 frames of activity occurred immediately after flash photolysis of ci-IP_3. For *n* = 2, the frames were taken from the middle of the recording; and for *n* = 2 cells, the frames were taken from the end of the recording. Dots represent the total number of IP_3-evoked Ca^{2+} puffs detected per cell and paired observations are connected by a straight line. $P > 0.05$, using a two-tailed paired Wilcoxon test.

Flika was next validated for the duration of a whole recording. The majority of events detected by Flika were also identified by manual analysis of the stack (**Figure 3.6**, red arrows). The threshold was set low to enable detection of small events. Some of these events were only identified by Flika, but they were then validated as true events by visual inspection (**Figure 3.6**, blue arrows). Setting a low threshold during the analysis allows the user to identify Ca^{2+} events that lie close to the baseline. This, however, results in identification of false-positives (~5%) (**Figure 3.6**, yellow arrows). An added advantage of Flika is that it enables the user to go through the puffs identified by the threshold-algorithm and check whether they are real events. Events identified as false positives (**Figure 3.6**, yellow arrows) can be deleted after manual inspection and removed from further analysis.

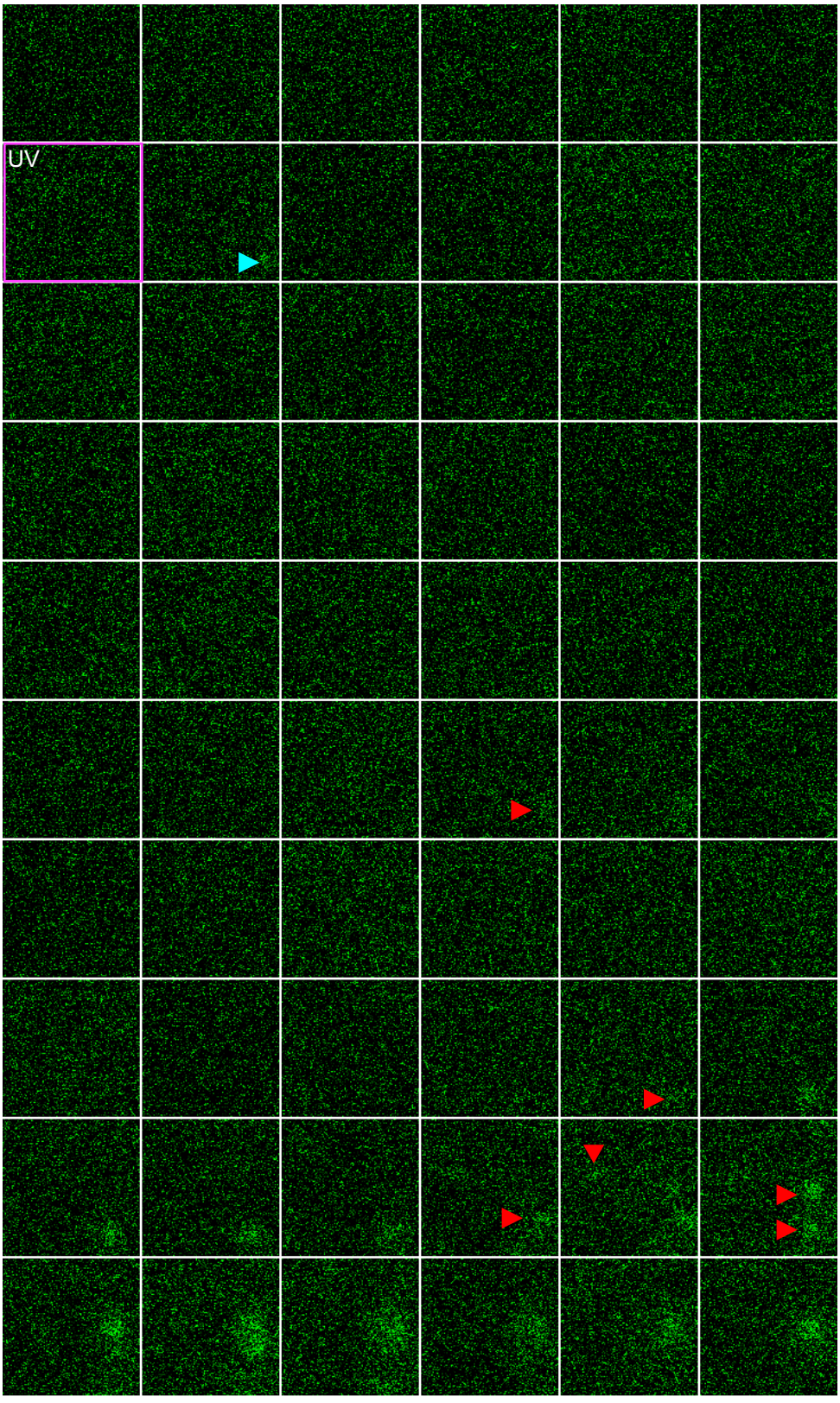

Figure 3.6A: Flika faithfully detects IP_3-evoked Ca^{2+} signals throughout the duration of a recording. The legend is provided with Figure 3.6E.

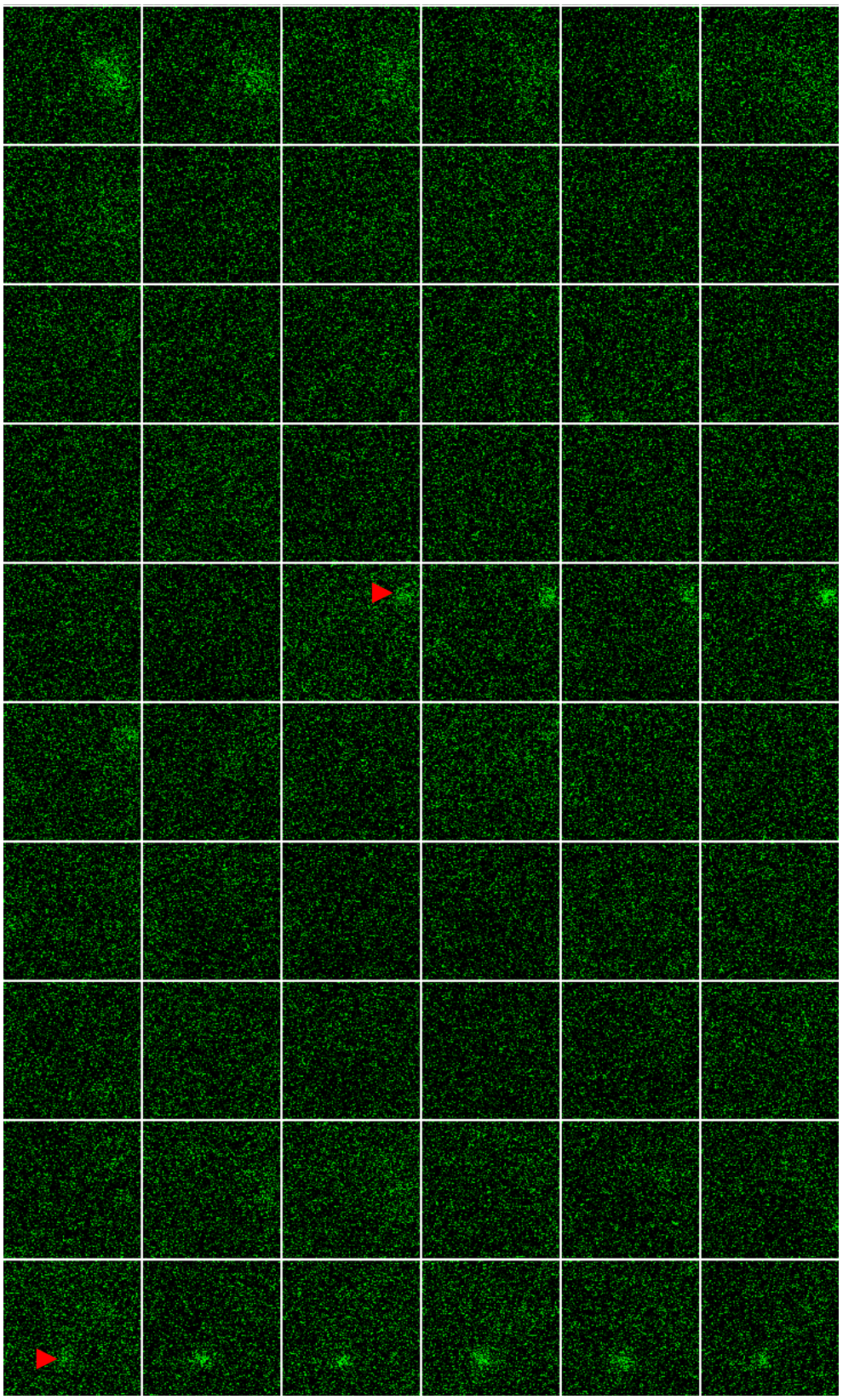

Figure 3.6B: Flika faithfully detects IP_3-evoked Ca^{2+} signals throughout the duration of a recording. The legend is provided with Figure 3.6E.

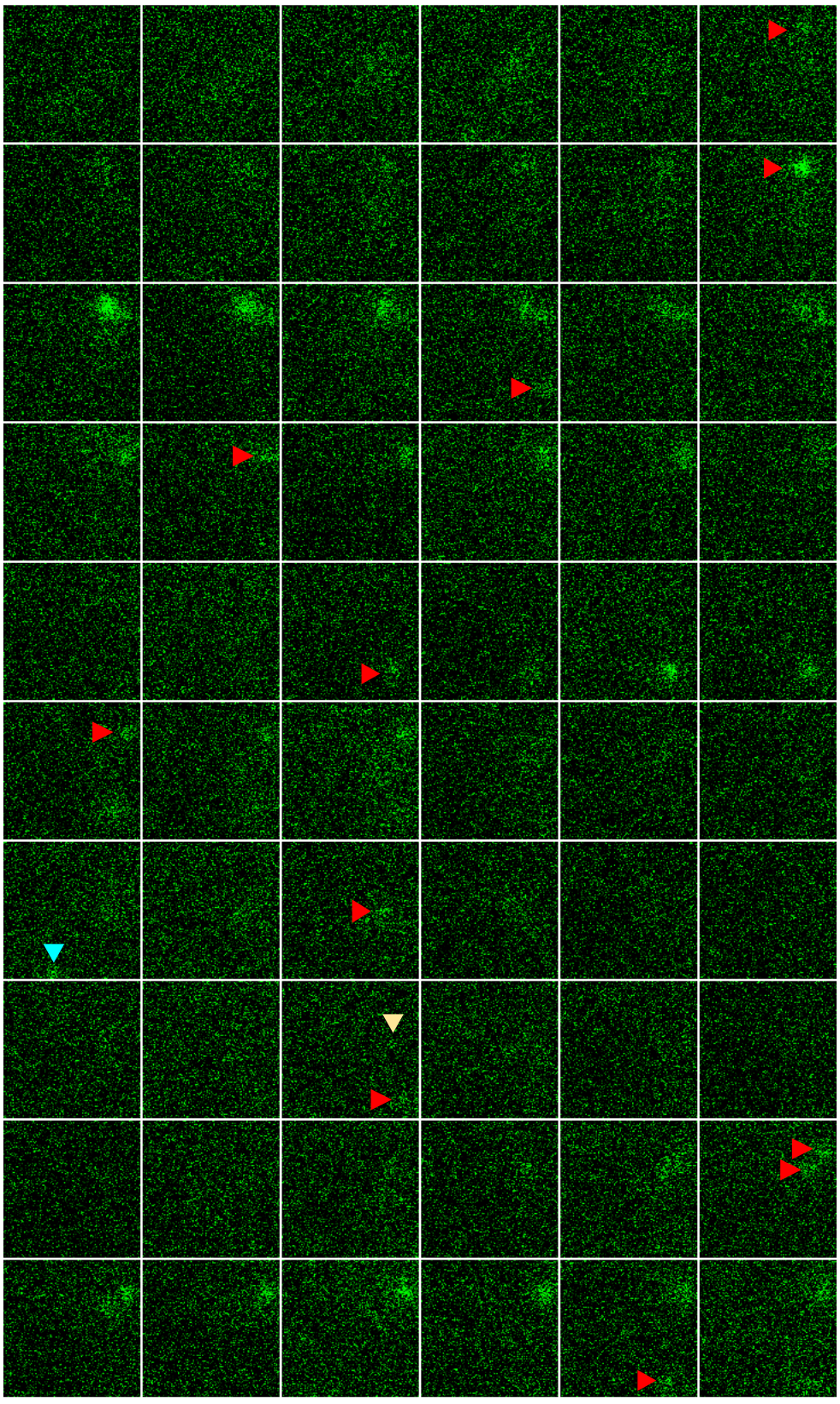

Figure 3.6C: Flika faithfully detects IP_3-evoked Ca^{2+} signals throughout the duration of a recording. The legend is provided with Figure 3.6E.

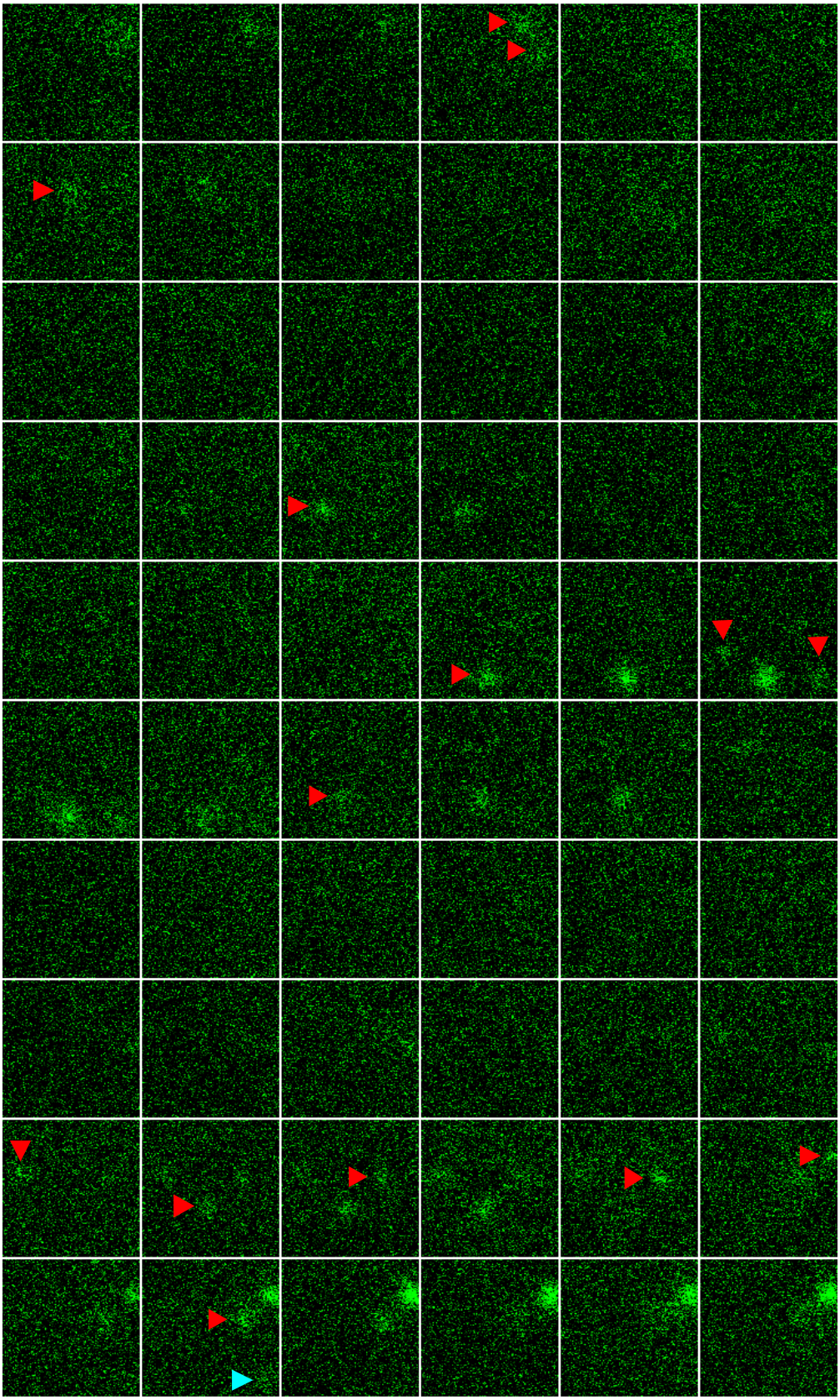

Figure 3.6D: Flika faithfully detects IP_3-evoked Ca^{2+} signals throughout the duration of a recording. The legend is provided with Figure 3.6E.

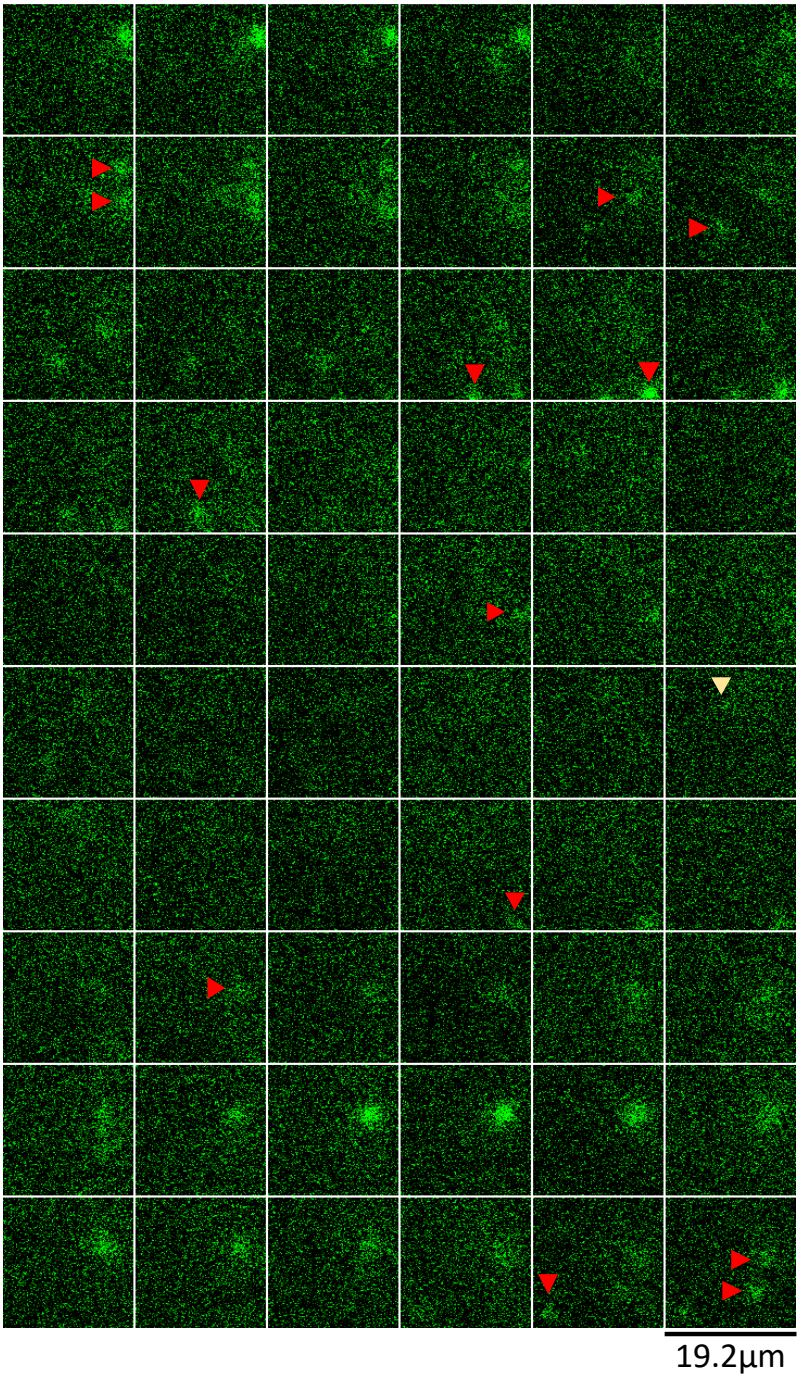

Figure 3.6E: Flika faithfully detects IP_3-evoked Ca^{2+} signals throughout the duration of a recording. TIRFM images from part of a WT cell show fluorescence before and after photolysis of ci-IP_3, throughout the duration of a recording (Parts A-E). The first frame after flash photolysis of ci-IP_3 is highlighted in pink (in part A). Images collected at 5.32ms intervals, with every 2nd frame shown. Red shows IP_3-evoked Ca^{2+} puffs identified by Flika. Blue arrows show events missed by manual analysis. Yellow arrows show events that were identified as false positives and were removed from further analysis. The scale bar applies to each part of the figure. The same legend applies to parts A-E.

3.4 Conclusions

High temporally resolved analyses of local Ca^{2+} signals using the optical patch-clamp method generate a large volume of data that is unmanageable when analysed manually (Keebler and Taylor, 2017). To automatically detect and extract useful information from Ca^{2+} events, several programmes were developed based on Ca^{2+} events mediated by RYRs. Although such programmes have been used for the detection of IP_3-mediated Ca^{2+} events, they have been shown to be unreliable (Keebler, 2015, Keebler and Taylor, 2017). The differences in spatiotemporal properties between Ca^{2+} sparks and Ca^{2+} puffs may account for the limited application of these programmes in the detection of IP_3-evoked Ca^{2+} events. This Chapter describes how the programme developed by Kyle Ellefsen (Ellefsen et al., 2014) detects Ca^{2+} events and how it was validated for use in the detection of IP_3-mediated Ca^{2+} events in HEK WT cells.

Flika has some characteristics that enable it to faithfully detect local Ca^{2+} signals: i) its ability to group puffs to sites and ii) the ability to manually examine Ca^{2+} puffs detected automatically. The latter is particularly useful, as it allows the user to visually inspect all detected events and delete false positives from subsequent analysis. The ability to delete false positives combined with the fact that it is extremely uncommon to miss any true events make it a reliable tool that can been used in various experimental settings.

The work described in this chapter provides the foundation for the use of Flika in Chapter 4.

Chapter 4: Ca^{2+} puffs are the building blocks for Ca^{2+} signals mediated by all IP_3R subtypes

4.1 Introduction

4.1.1 IP_3R family

Vertebrate genomes contain three genes that encode a family of IP_3Rs (IP_3R1-3), with multiple splice variants reported for IP_3R1. The three different subtypes share ~60-80% overall amino acid similarity and can assemble to form homo- or hetero-tetrameric Ca^{2+}-release channels regulated by IP_3 and biphasically by Ca^{2+} (Maeda et al., 1991, Wojcikiewicz and He, 1995, Taylor et al., 1999, Foskett et al., 2007, Berridge, 2016). Some amino acid sequences are more conserved. For example, the residues that interact with the three phosphate groups of IP_3 are highly conserved among the three IP_3R subtypes. An additional example, are the highly conserved amino acid residues located in the fifth and sixth TMDs, which form the Ca^{2+}-permeable pore (Taylor et al., 1999). Hence, functions that are conserved between the subtypes such as binding of IP_3 and formation of a Ca^{2+}-permeable pore are associated with the most conserved sequences. Within the less conserved sequences, the differences are so small that they are unlikely to affect the 3D structure of the channel. As a result, the three IP_3R subtypes share similar overall structures (Fan et al., 2015, Paknejad and Hite, 2018).

There are, however, functional differences between IP_3R subtypes. They differ in their affinities for IP_3 (Iwai et al., 2007) and in their regulation by other molecules (Prole and Taylor, 2016). The three subtypes are differentially expressed between cells and tissues, and perhaps within different parts of the same cell. The latter may allow different IP_3R subtypes to interact selectively with other intracellular organelles, such as mitochondria (Mendes et al., 2005). The subtypes can also be degraded at different rates (Wojcikiewicz, 1995).

The expression of multiple IP_3R subtypes, their ability to assemble into either homo- or heterotetrameric channels, the lack of subtype-selective ligands, and the lack of tools that allow complete and selective inactivation of IP_3R

subtypes acutely make it difficult to disentangle the contribution of each IP_3R subtype to Ca^{2+} signalling (Hattori et al., 2004, Saleem et al., 2012, Saleem et al., 2013).

4.1.2 Differential regulation of physiological and cellular functions by IP_3R subtypes

Most tissues express at least two IP_3R subtypes, although different subtypes predominate in different cells (Newton et al., 1994). Central nervous system cells such as cerebellar Purkinje cells and SH-SY5Y cells (as used in much of the work from Ian Parker's lab) (Smith et al., 2009a) predominantly express IP_3R1 (Wojcikiewicz, 1995). Several studies have highlighted the importance of IP_3R1 in brain function. $IP_3R1^{+/-}$ mice had impaired motor coordination skills (Ogura et al., 2001) and *IP$_3$R1*$^{-/-}$ mice either die in utero or by the weaning period after experiencing severe ataxia and seizures (Matsumoto et al., 1996). The phenotype of IP_3R1-deficient mice is similar to that of the *opisthotonos* (opt) mouse, which lacks part of the IP_3R1 regulatory region (Street et al., 1997). Additionally, conditional KO of IP_3R1 in Purkinje cells increased their spine density and length, and adult mice experienced severe ataxia (Sugawara et al., 2013). These studies highlight the importance of IP_3R1-mediated Ca^{2+} release in mediating the excitability of Purkinje cells. Consistent with IP_3R1 being important in normal function, Takei et al. showed that local inactivation of IP_3R1 in dorsal root ganglia growth cones inhibits neural extension and causes growth arrest and retraction (Takei et al., 1998). Thus, IP_3R1 is crucial for brain development and function.

High IP_3R1 mRNA levels are also detected in mouse oocytes, consistent with the contribution of IP_3R1 to Ca^{2+} oscillations in the fertilised egg. Indeed, inhibition of IP_3R1 with a monoclonal antibody inhibits Ca^{2+} oscillations required for normal fertilisation in hamster eggs (Miyazaki et al., 1992). Apart from its roles in brain cells and embryonic development, IP_3R1 is ubiquitously expressed and thought to be involved in ubiquitous cell functions such as proliferation (Fujino et al., 1995).

In adult ventricular cells, IP_3Rs have been associated with arrhythmias and cardiac hypertrophy (Kockskamper et al., 2008). IP_3R2 is the predominant subtype in atrial myocytes and co-localises with RYRs, although RYRs are much more abundant (RYR to IP_3R ratio ~ 50-100 to 1) (Moschella and Marks, 1993). Consistent with its subcellular location, IP_3R2 is thought to have an ionotropic effect on Ca^{2+} signals mediated by RYRs during E-C coupling (Li et al., 2005). Atrial myocytes can be activated in response to high agonist concentrations, such as endothelin (ET-1) which is known to contribute to cardiac arrhythmias and hypertrophy. Under basal conditions, electrically stimulated IP_3R2-deficient atrial myocytes had similar Ca^{2+} transients as WT cells, suggesting that IP_3R2 does not affect E-C coupling. Stimulation with ET-1, however, increased the amplitude of Ca^{2+} signals evoked by electrical stimulation, while it had no effect in IP_3R2 KO cells or in wild-type cells incubated with 2-aminoethoxydiphenyl borate (2-APB). These observations suggest that ventricular arrhythmias evoked by an increase in [ET-1] might be a result of the inotropic effects of IP_3R2-mediated signalling on E-C coupling.

Nakayama et al generated a transgenic mouse cell line with inducible enhanced IP_3R2 expression. By three months, the mice had developed cardiac hypertrophy, measured as an increased heart to body ratio; and consistent with a hypertrophic phenotype, hypertrophy-associated genes were expressed. The transgenic model was crossed with another transgenic mouse model with an inducible IP_3-sponge. This is a soluble and truncated IP_3R that binds IP_3 with high affinity. The increased Ca^{2+} events and arrhythmias associated with IP_3R2 overexpressing mice were abolished by the IP_3-sponge (Nakayama et al., 2010). Drawnel and colleagues showed that myocytes overexpressing miRNA-133a (an anti-hypertrophy microRNA) had decreased IP_3R2 protein levels, while miRNA-133a silencing led to increased IP_3R2 levels and increased gene expression of a hypertrophy gene. It was hypothesised that the hypertrophic effects are driven by IP_3-evoked Ca^{2+} signals. Consistent with this hypothesis, IP_3 5-phosphatase, which metabolises IP_3, reduced the expression of a hypertrophy marker (Drawnel et al., 2012). Thus, in pathological conditions in which IP_3R2 levels may be elevated, IP_3R2 seems to contribute to cardiac hypertrophy and arrhythmias.

IP_3R2 has also been associated with cell migration. Ca^{2+} imaging in migrating human fibroblasts showed a global [Ca^{2+}] gradient and highly localised Ca^{2+} events (flickers) located exclusively to the leading end of the cell (Wei et al., 2009). Mechanical stimulation elicited Ca^{2+} flickers in the leading edge, but their amplitude was reduced by thapsigargin or IP_3R2 knockdown, suggesting that Ca^{2+} flickers in migrating cells are generated by stretch-activated cation channels and amplified by IP_3R2-mediated Ca^{2+} release. Furthermore, migrating fibroblasts steered towards the chemoattractant that was added in a direction perpendicular to cell movement. The change in direction was accompanied by an increase in flicker activity in the cell portion facing the chemoattractant. In similar experiments, IP_3R2 knockdown diminished the ability of cells in changing direction towards the chemoattractant (Wei et al., 2009). The study by Wei et al. (2009) shows compelling evidence for the importance of IP_3R2 in cell migration and steering.

itpr3 mRNA is very abundant in the intestine (Newton et al., 1994) and its gene product has been associated with taste perception and secretion. IP_3R3 KO mice display unusual behaviour to certain tastes, such as sweet and bitter. Wild-type mice were shown to respond to these tastes in a dose-dependent manner in behavioural studies, while IP_3R3 KO mice did not. The behavioural responses were consistent with electrophysiological recordings from nerves located at the taste buds, that showed markedly decreased responses to certain tastes. Other tastes such as sour remained unaffected in the IP_3R3 KO mice (Hisatsune et al., 2007).

IP_3R subtypes are also found in different intracellular locations. While IP_3R1 and IP_3R3 have a more reticular distribution (Vermassen et al., 2004, Pantazaka and Taylor, 2011), IP_3R2 has a more punctate distribution (Pantazaka and Taylor, 2011) and has been shown to be expressed in unidentified vesicular structures that are very mobile (Prole and Taylor, unpublished). This suggests that different IP_3R subtypes may mediate different functions in a cell. Several studies have implicated IP_3Rs with mitochondrial Ca^{2+} signalling and apoptosis. A study by Mendes and co-workers showed that while Chinese hamster ovary eggs express all three IP_3Rs, mitochondrial Ca^{2+} signals and apoptosis are preferentially

mediated by IP_3R3. In this study, IP_3R3 stained pixels co-localised to some extent (~25%) with Mitotracker Red and siRNA knockdown of IP_3R3 partially inhibited mitochondrial Ca^{2+} signals and bile-induced apoptosis. Despite these results, some effects were also observed with single knockdowns of the other two subtypes, especially relating to apoptosis, but only IP_3R3 effects were shown to be statistically significant (Mendes et al., 2005). Evidence from other studies does not, however implicate IP_3R3 in apoptosis, but instead implicates IP_3R1. IP_3R1-deficient Jurkat T lymphoma cells are protected from apoptosis, suggesting that IP_3R1 has a preferential role in apoptosis (Jayaraman and Marks, 1997). Thus, it appears that IP_3R-mediated release from the ER is a key step in the induction of apoptosis, but the exact complex assembled in the ER-mitochondria contact sites is unknown and may differ between cell types (Rizzuto et al., 2009).

Despite the distinct contribution of each IP_3R subtype in distinct tissues, IP_3R subtypes are often redundant. There is some evidence that IP_3Rs may be vital in cardiogenesis. RYR2 KO mice die in utero around embryonic day 10 with severe defects in the heart tube as the E-C coupling system cannot develop. There is, however, evidence of spontaneous Ca^{2+} signals and heart contractions before their death, indicating that early Ca^{2+} signals in cardiogenesis are RYR2-independent. (Takeshima et al., 1998). A study by Sasse and colleagues implicates IP_3Rs in mediating early Ca^{2+} signals in the heart. Ca^{2+} oscillations in murine embryonic cardiomyocytes were inhibited by the depletion of intracellular stores but were insensitive to the inhibition of voltage-activated Ca^{2+} channels (Sasse et al., 2007). A mouse model generated by Uchida et al. reinforces this hypothesis as $IP_3R1^{-/-}$ - $IP_3R2^{-/-}$ mice were embryonic lethal and died in utero with severe ventricular defects. This indicates that IP_3R1 and IP_3R2 may have redundant roles in cardiogenesis (Uchida et al., 2010).

$IP_3R2^{-/-}$-$IP_3R3^{-/-}$ mice display a malnourished phenotype and die within four weeks, while single subtype KO were viable. When the double KO were fed with wet mash, they were able to survive suggesting that their digestive system was malfunctioning. Consistent with this, they displayed symptoms of digestive malfunctions such as high nutrient concentrations in their feaces. This phenotype was associated with impairments in saliva and digestive enzyme secretion.

Double KO pancreatic cells were swollen and both Ca^{2+} release and digestive enzyme secretion in response to CCh were abolished (Futatsugi et al., 2005). Consistent with the involvement of both IP_3R2 and IP_3R3 in regulating enzyme and water secretion in exocrine tissues, olfactory mucus secretion in $IP_3R2^{-/-}$-$IP_3R3^{-/-}$ mice is abolished. Ca^{2+} imaging in acinar nasal cells showed that Ca^{2+} responses were abolished, whereas ACh stimulation led to Ca^{2+} waves in both wild-type and the two single KO cells. The abolished Ca^{2+} response to ACh in double KO cells was associated with increased intracellular accumulation of fluid and reduced protein concentration in extracellular fractions (Fukuda et al., 2008). Hence, IP_3R subtypes often have redundant roles.

4.1.3 Properties of single IP_3R subtypes

Different IP_3Rs have been shown to mediate different types of Ca^{2+} signals in DT40 cells endogenously expressing a single IP_3R subtype. IP_3R2 mediated long-lasting Ca^{2+} oscillations, IP_3R1 mediated less regular Ca^{2+} signals, and IP_3R3 mediated monophasic Ca^{2+} signals (Miyakawa et al., 1999). Consistent with these observations IP_3R1 knockdown in HeLa cells abolished Ca^{2+} oscillations, while IP_3R3 knockdown promoted them (Hattori et al., 2004). These studies are important in understanding how different IP_3Rs contribute to spatiotemporally distinct Ca^{2+} signals, but they provide no information on which IP_3R features are responsible for the different Ca^{2+} signals (Foskett et al., 2007).

IP_3Rs are cation-selective, high-conductance channels with a modest selectivity for Ca^{2+} over monovalent ions such as K^+ (Ca^{2+} to K^+ ratio ~ 6) (Williams et al., 2001, Foskett et al., 2007, Taylor and Tovey, 2012). In comparison to IP_3Rs, Ca^{2+} channels on the PM, such as SOCs, are much more selective for Ca^{2+} (Ca^{2+} to K^+ ratio >1000) and have lower single-channel conductance (Zweifach and Lewis, 1995, Taylor and Tovey, 2012). IP_3Rs mainly conduct Ca^{2+}, as Ca^{2+} is probably the only cation moving down its concentration gradient ($[Ca^{2+}]_c$ ~ 100nM while $[Ca^{2+}]_{ER}$ ~ 100μM) (Taylor and Tovey, 2012), with channel openings lasting a few milliseconds (Ramos-Franco et al., 1998a).

Under similar ionic conditions, nuclear patch-clamp recordings for different IP_3R subtypes give similar conductance values. Recording of endogenous IP_3R1

channels in *Xenopus* oocytes suggest a channel conductance value of 370 ± 5 pS (Mak and Foskett, 1998), while nuclear recordings from recombinant IP_3R1 channels in DT40 3KO cells are consistent (373 ± 2 pS) (Betzenhauser et al., 2009). Additionally, recombinant IP_3R2 channels in DT40 3KO and recombinant IP_3R3 channels in *Xenopus* oocytes have a channel conductance of 375 ± 5 pS (Wagner and Yule, 2012) and 358 ± 5 pS (Mak et al., 2000), respectively. It is suggested that highly conserved amino acid residues that form the channel pore, also determine channel conductance (Mak and Foskett, 2015).

There has been, however, some disagreement concerning the ability of cytosolic Ca^{2+} to inhibit Ca^{2+} release by different subtypes. Ca^{2+}-dependent inhibition of Ca^{2+}-release serves as a mechanism of autoregulation and is essential to support Ca^{2+} oscillations and regenerative Ca^{2+} waves (Hagar et al., 1998). Although most studies would agree that IP_3R1 displays a bell-shaped dependence on Ca^{2+}, the findings regarding IP_3R2 and IP_3R3 are controversial, with some studies suggesting that the latter two subtypes are not regulated by cytosolic Ca^{2+}. A bell-shaped dependence on Ca^{2+} suggests that as $[Ca^{2+}]_c$ increases the probability of the channel being open (P_o) also increases (with a maximal P_o ~0.8 for all IP_3R subtypes) and after a certain $[Ca^{2+}]_c$ (~1μM), Ca^{2+} becomes inhibitory (Ramos-Franco et al., 1998a, Foskett et al., 2007). It has been suggested that this is not the case for IP_3R2 and IP_3R3, and that they both show a sigmoidal dependence on Ca^{2+} (Ramos-Franco et al., 1998a, Hagar et al., 1998), whereas other studies suggest a bell-shaped dependence on Ca^{2+} for both IP_3R2 and IP_3R3 (Marshall and Taylor, 1993, Cardy et al., 1997, Swatton et al., 1999, Taylor and Laude, 2002, Swatton and Taylor, 2002, Tu et al., 2005, Foskett et al., 2007). Despite some studies suggesting that IP_3R2 and IP_3R3 channels are not inhibited by high cytosolic Ca^{2+}, the general consensus is that all IP_3R subtypes are inhibited by high $[Ca^{2+}]_c$. The discrepancies between the different analyses may be due to the different experimental preparations (Swatton et al., 1999, Foskett et al., 2007). Overall, patch-clamp recordings show that the general shapes of channel P_o versus $[Ca^{2+}]_c$ between different IP_3Rs are similar, with minor differences in their Ca^{2+} dependencies. For example, the maximal P_o of IP_3R1 by Ca^{2+} is achieved within a narrow $[Ca^{2+}]_c$ range, while P_o of IP_3R3 increases over a broader range of $[Ca^{2+}]_c$ (Foskett et al., 2007).

Most studies agree that different IP_3R subtypes have different IP_3 affinities with a relative order of affinities of $IP_3R2 > IP_3R1 > IP_3R3$, with binding affinities determined by the suppressor domain (Südhof et al., 1991, Newton et al., 1994, Ramos-Franco et al., 1998a, Hagar and Ehrlich, 2000, Iwai et al., 2007). The fact that different IP_3R subtypes have different IP_3 affinities is very important as it could serve as a path of segregating parallel signalling cascades (Ramos-Franco et al., 1998a). For example, in a cell expressing both IP_3R2 and IP_3R3 a low IP_3 stimulus would be enough to elicit IP_3R2-mediated Ca^{2+}-release, while IP_3R3 would remain inactive.

IP_3R subtypes share most key functional attributes (conductance, selectivity, inhibition by $[Ca^{2+}]_c$, open times) (Mak and Foskett, 1998, Ramos-Franco et al., 1998a, Foskett et al., 2007, Betzenhauser et al., 2009, Wagner and Yule, 2012, Mak et al., 2000, Clapham, 2007) but have notable differences in their modulation by accessory regulators and affinity for IP_3 (Südhof et al., 1991, Newton et al., 1994, Ramos-Franco et al., 1998a, Hagar and Ehrlich, 2000, Iwai et al., 2007, Foskett et al., 2007). These functional attributes and many other factors including channel density and distribution of IP_3R clusters determine the complex Ca^{2+} signals generated by different IP_3R subtypes.

4.1.4 Imaging of Ca^{2+} signals mediated by single IP_3R subtypes

Hitherto, the only null-background wherein single IP_3R subtypes can be expressed is provided by the DT40 3KO cell line (Sugawara et al., 1997). The cytoplasm of these cells, however, is restricted to a narrow rim around the nucleus, making DT40 cells unsuitable for analyses of elementary Ca^{2+} signals by TIRFM. As a result, nobody has yet imaged Ca^{2+} signals mediated by single IP_3R subtypes, although Ca^{2+} puffs have been reported for cells in which different IP_3R subtypes predominate (Rooney et al., 1990, Kasai et al., 1993, Yao et al., 1995, Bootman et al., 1997a, Simpson et al., 1997, Smith and Parker, 2009, Nakamura et al., 2012, Keebler and Taylor, 2017). Thus, it is unclear whether all IP_3R subtypes are capable of generating Ca^{2+} puffs, and whether Ca^{2+} elementary events are the building blocks of all IP_3-evoked Ca^{2+} signals.

4.1.5 Aim this Chapter

The aim of the work described in this chapter was to establish whether all three IP_3R subtypes can generate Ca^{2+} puffs and to define any differences between them.

4.2 Materials and Methods

4.2.1 Materials

NP-EGTA-AM (caged EGTA, O-nitrophenyl-EGTA-AM) was from Thermofisher (Paisley, UK). The sources of other materials are listed in Sections 2.2.1 and 3.2.1.

4.2.2 Cell culture

Wild-type HEK cells, from which the gene-edited cell lines were derived were provided by Dr D. Yule (University of Rochester, NY, USA). Gene-edited HEK cells expressing single IP_3R subtypes (Alzayady et al., 2016), were from Kerafast (Boston, MA, USA). The culture and characterisation of the four cell lines are described in Section 2.2.2 and 2.3.4, respectively.

4.2.3 High-resolution imaging and analysis of Ca^{2+} signals

The methods used for high-resolution imaging of Ca^{2+} signals are provided in Section 3.3.5. The methods used to load cells with NP-EGTA-AM (1μM) were the same used for loading with ci-IP_3/PM (Section 3.2.4). The detection of Ca^{2+} events used the Flika program (Ellefsen et al., 2014) (https://github.com/flika-org/flika) and is described in Section 3.3.5.

4.2.4 Statistics

Results are presented as means ± s.e.m., unless otherwise stated, with *n* usually referring to the number of cells analysed. Statistical analyses used Kruskal-Wallis test with Dunn's correction for multiple comparisons (PRISM version 6, GraphPad, CA, USA). Statistical significance is denoted by: $^{*}p < 0.05$, $^{**}p < 0.01$, $^{***}p < 0.001$.

4.3 Results and Discussion

4.3.1 All IP_3Rs subtypes can generate Ca^{2+} puffs

I used CRISPR/Cas9-edited HEK cells that express a single IP_3R subtype and the HEK WT cell line from which the other cell lines were generated (Section 2.3.4). Cells were loaded with Cal520 to record Ca^{2+} signals, EGTA to limit the propagation of the Ca^{2+} signal, and ci-IP_3 to allow photo-release of the stable IP_3 analogue, i-IP_3.

Cal520 fluorescence was recorded from cells for 40s after delivery of a uniform stimulus across the cell lines (50ms UV flash). This was preceded by a 40s pre-stimulation period. A 50ms UV flash was chosen because it evoked Ca^{2+} puffs in cells expressing single IP_3R subtypes, and allowed ~8s of useful recording in HEK WT cells prior to global elevations in $[Ca^{2+}]_c$. A lower stimulus was not sufficient to reliably evoke Ca^{2+} puffs in single IP_3R subtype-expressing cells, and greater flash intensities rapidly evoked global Ca^{2+} signals in HEK WT cells. Even though the exact i-IP_3 concentration cannot be quantified in these analyses, the parallel loadings of these cells and delivery of the uniform stimulus (50ms flash) are likely to have resulted in similar concentration of i-IP_3 in the cytosol of each cell line.

To resolve the kinetic properties of each Ca^{2+} puff, recordings were performed at the high temporal resolution of 188Hz (intervals of 5.32ms). In order to achieve such a high temporal resolution, it was necessary to restrict the recording area to a 19.2μm x 19.2μm region. Hence, the results in this chapter report the events detected from only a portion of each cell (~25% of the TIRF footprint of the cell), (**Figure 4.1A**) and **4.1B**). Prior to analysis, it was verified that recording areas were indistinguishable in the four cell lines (**Figure 4.1B**).

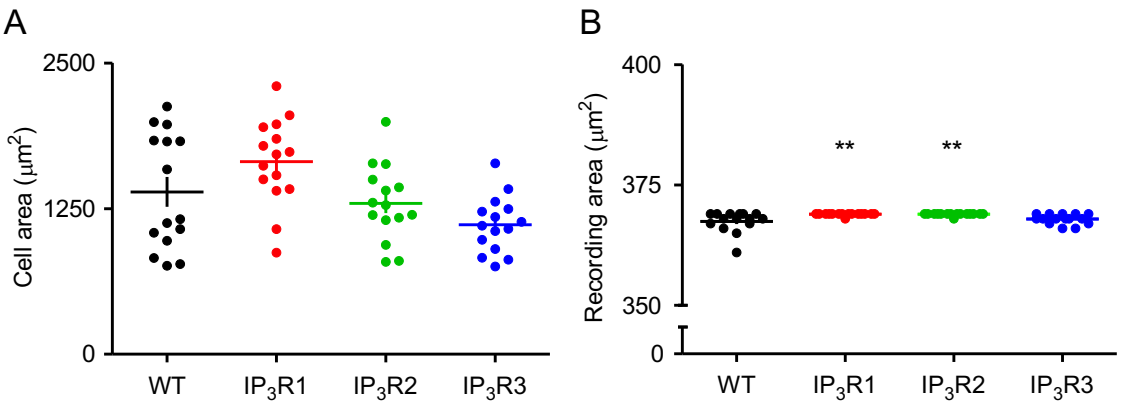

Figure 4.1: Recording areas are similar in all cell lines. (A) Total cell areas detected by TIRF and **(B)** total recording areas within the TIRF field. Results show individual values (n = 15 for each cell line) and the mean ± s.d. $^{**}p < 0.01$ (Kruskal-Wallis test with Dunn's correction) relative to WT cells. Differences in recording areas for IP_3R1- and IP_3R2 expressing cells were not a source of experimental error as differences were less than 0.4% of the average recording area.

As Ca^{2+} puff kinetics can be influenced by intracellular Ca^{2+} buffer, I examined the effects of releasing Ca^{2+} from NP-EGTA to ensure there are no differences in intracellular Ca^{2+} buffering between the cell lines. The peak fluorescence changes were indistinguishable between cell lines (**Figure 4.2A** and **B)**, suggesting that Ca^{2+} buffering does not differ between them.

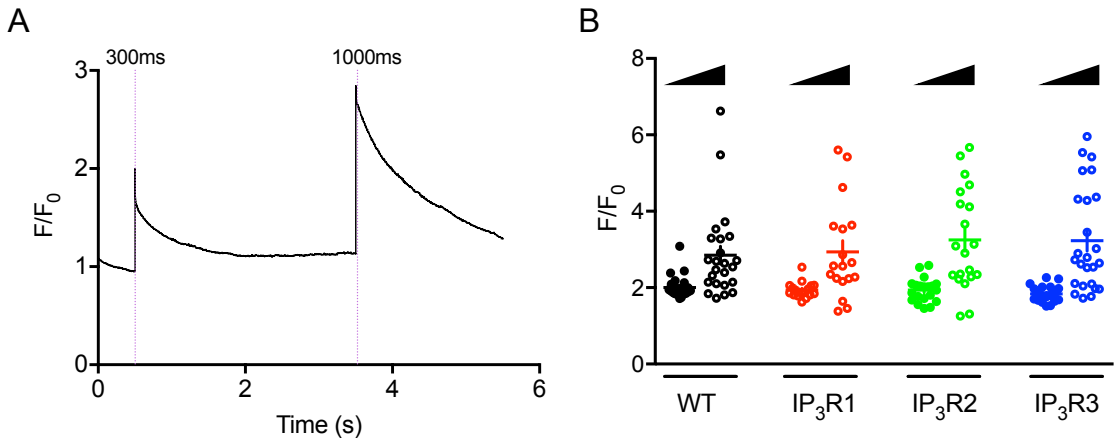

Figure 4.2: Intracellular Ca^{2+} buffering is similar in all cell lines. (A) Average response of WT cells (*n* = 24) loaded with NP-EGTA to the indicated flashes. The trace is from a ROI of 1.76 x 1.76 μm. **(B)** Summary data showing the mean, s.e.m. and individual values of peak fluorescence changes in response to a 300ms flash (filled circles) and a 1000ms flash (open circles).

In HEK WT cells (where, IP_3R3 > IP_3R1 > IP_3R2, **Figure 2.16**), flash photolysis of ci-IP_3 led to a flurry of Ca^{2+} puffs (**Figure 4.3A-B** and **Figure 4.4**), while no puffs were evoked in HEK 3-KO cells (**Figure 4.4**). Ca^{2+} puffs (**Figure 4.3A-B** and **Figure 4.5**) were detectable until a global signal invaded the cell leading to a global increase in $[Ca^{2+}]_c$ (**Figure 4.3B**). These responses are similar to those observed in other cell types (Kasai et al., 1993, Yao et al., 1995, Bootman et al., 1997a, Simpson et al., 1997, Smith and Parker, 2009, Nakamura et al., 2012). HEK cells expressing a single IP_3R subtype were also exposed to a 50ms UV flash and Cal520 fluorescence was recorded (**Figure 4.6 Parts A-C**).

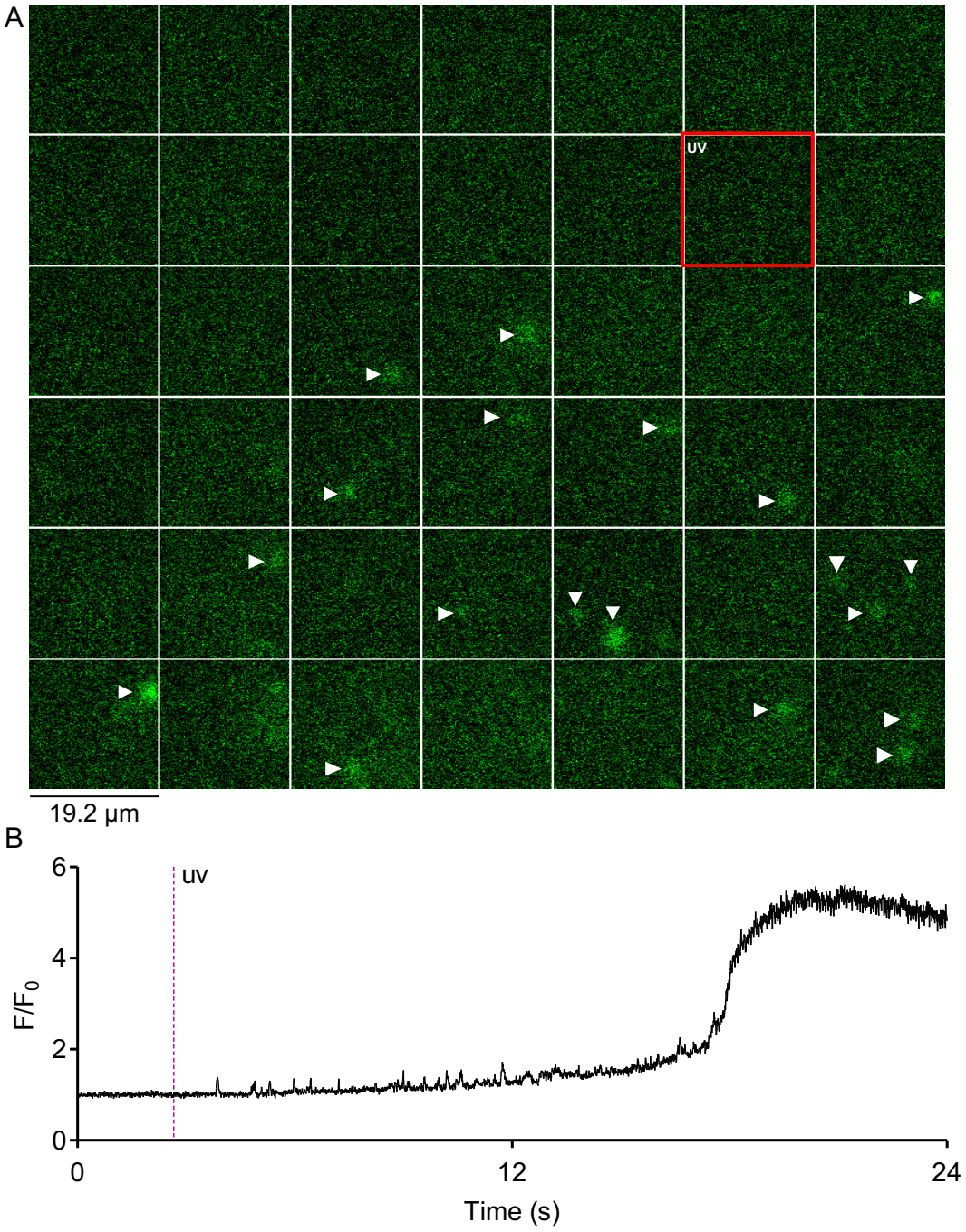

Figure 4.3: Flash photolysis of ci-IP_3 in HEK WT cells generates Ca^{2+} puffs and generates a Ca^{2+} wave. (A) Typical TIRF images show a portion of a HEK WT cell's cytoplasm fluorescence before and after photolysis of ci-IP_3. The first frame after the UV flash is highlighted in red, and white arrows point to puffs detected using the Flika program (Ellefsen et al., 2014). Images were collected at 5.32ms intervals, with every 20th frame shown in the montage. **(B)** Representative F/F_0 trace from a 1.76µm x 1.76µm region of the recording. The trace shows that prior to flash photolysis, there are no local Ca^{2+} elevations. After the UV flash, Ca^{2+} puffs are detected before a Ca^{2+} signal invades the entire cell.

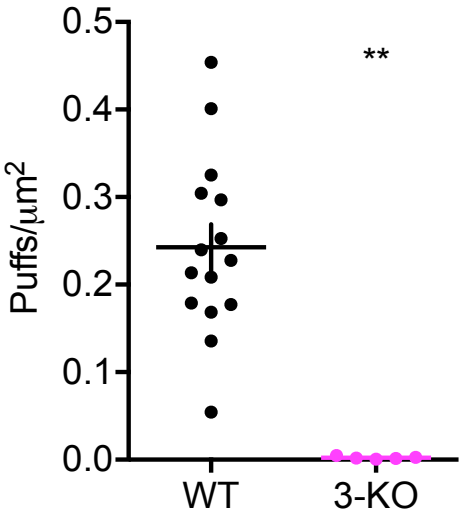

Figure 4.4: Flash photolysis of ci-IP_3 in HEK 3-KO cells does not evoke Ca^{2+} puffs. Numbers of Ca^{2+} puffs detected in WT and HEK 3-KO cells. Results show individual values for HEK WT (15 cells) and HEK 3-KO cells (5 cells), means ± s.e.m. $^{**}p < 0.01$, two-tailed Mann-Whitney test.

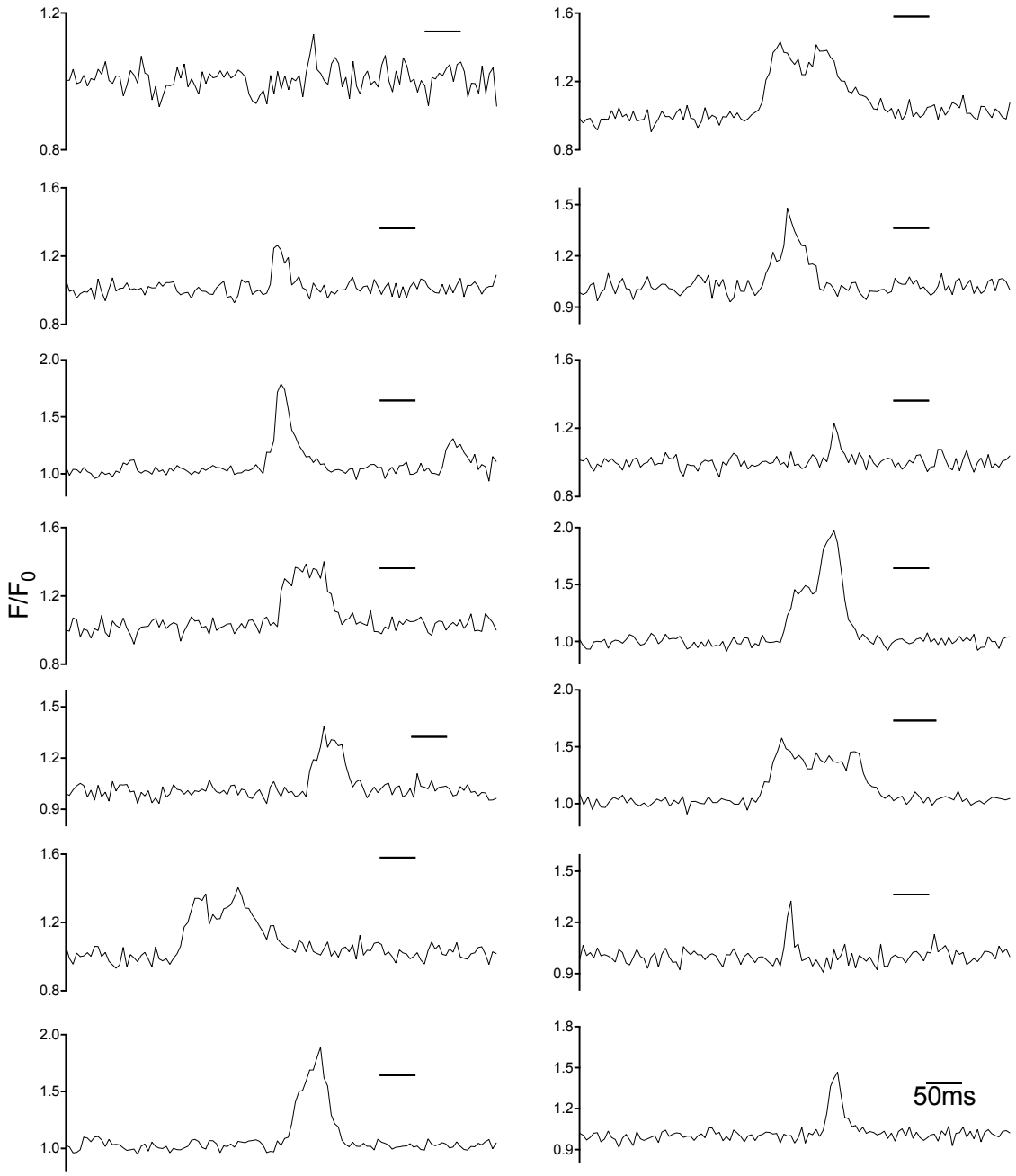

Figure 4.5: Examples of IP_3-evoked Ca^{2+} puffs in HEK WT cells. The figure shows 20 representative F/F_0 traces from a 1.76 x 1.76μm region of Ca^{2+} puffs from *N* = 4 cells. The events shown were detected using Flika, and traces were extracted from the F/F_0 stack. The code at the scale bar applies to every event.

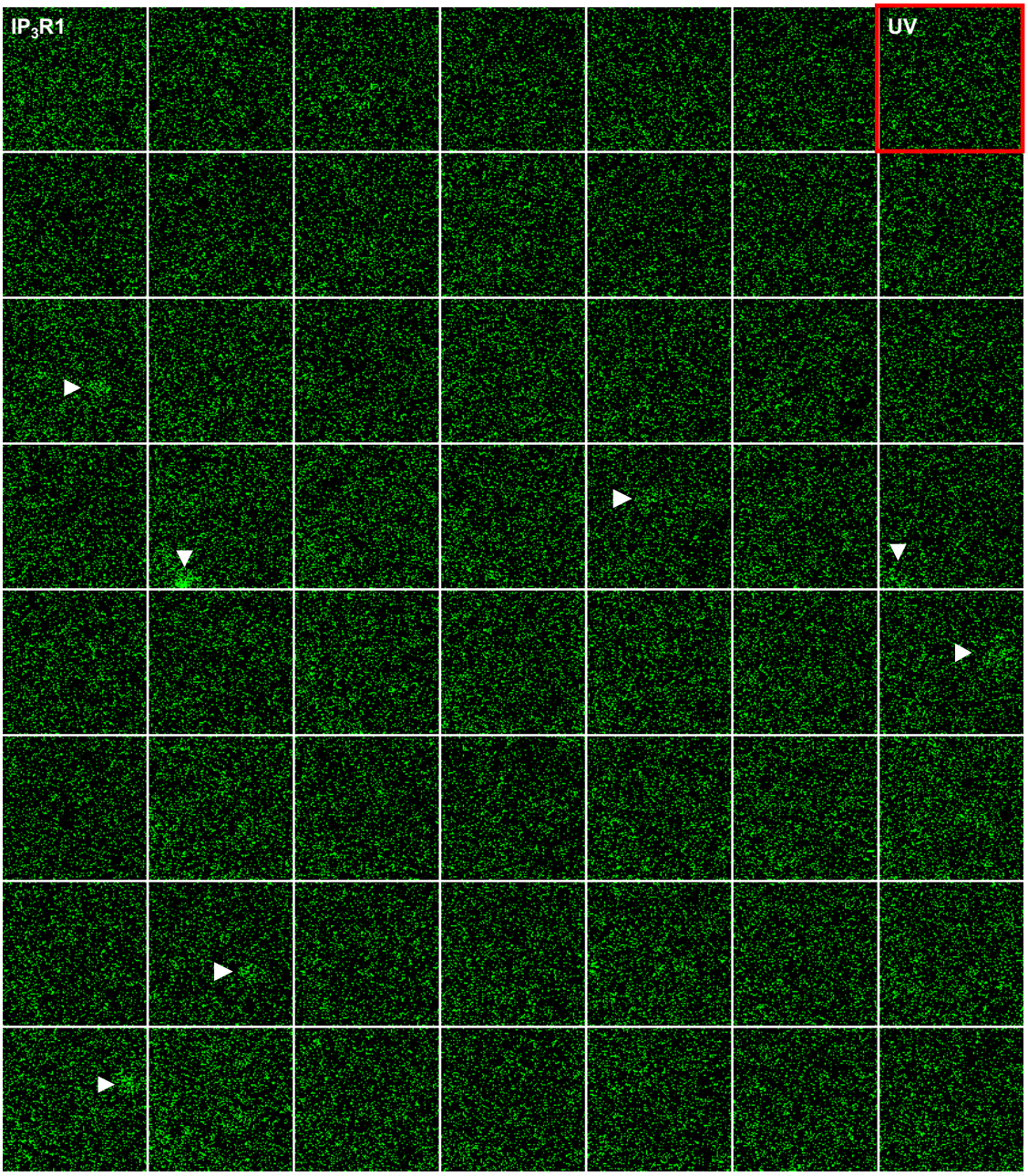

Figure 4.6A: Flash photolysis of ci-IP_3 in HEK cells expressing a single IP_3R subtype generates Ca^{2+} puffs. The legend is provided with Figure 4.6C.

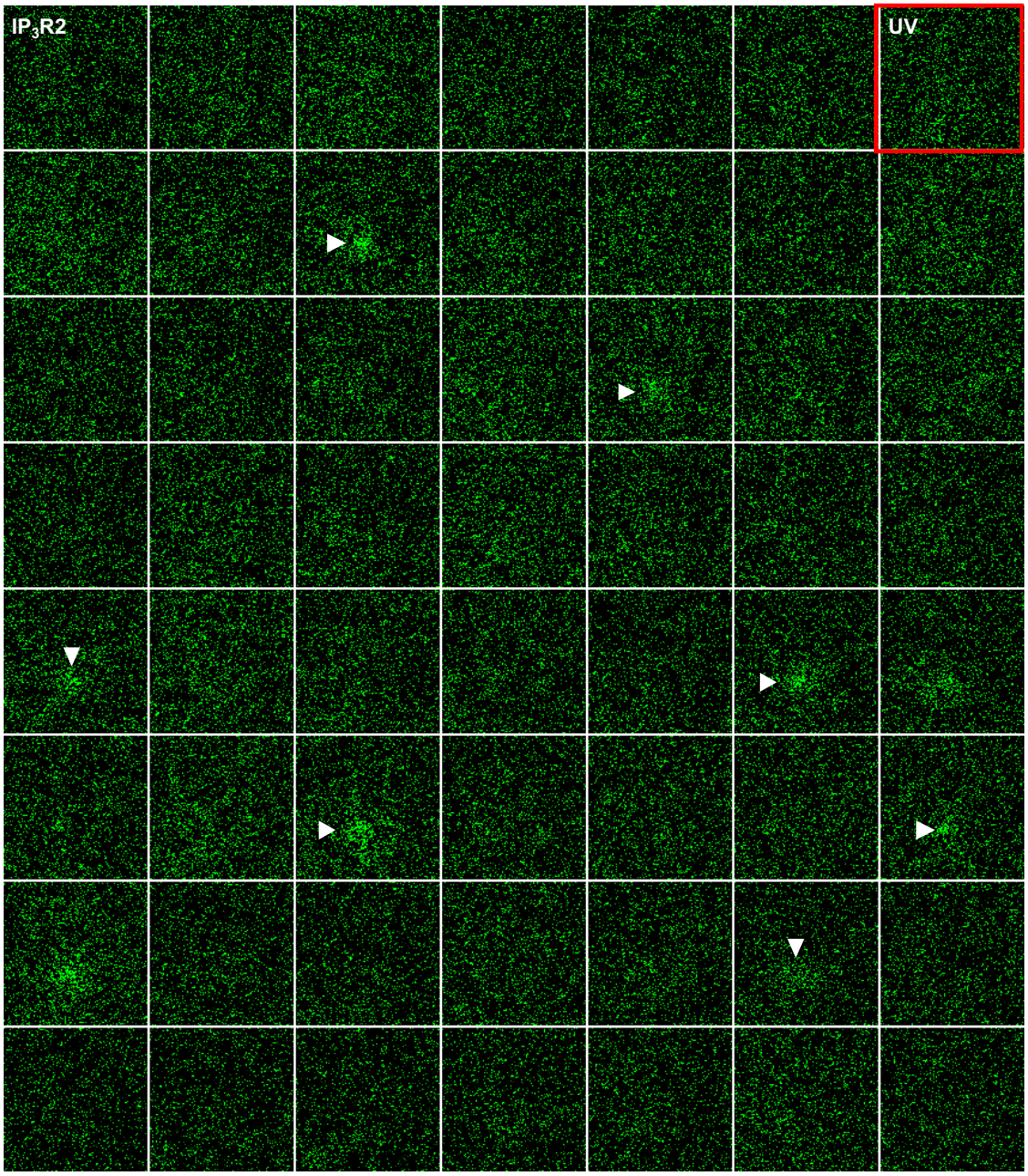

Figure 4.6B: Flash photolysis of ci-IP_3 in HEK cells expressing a single IP_3R subtype generates Ca^{2+} puffs. The legend is provided with Figure 4.6C.

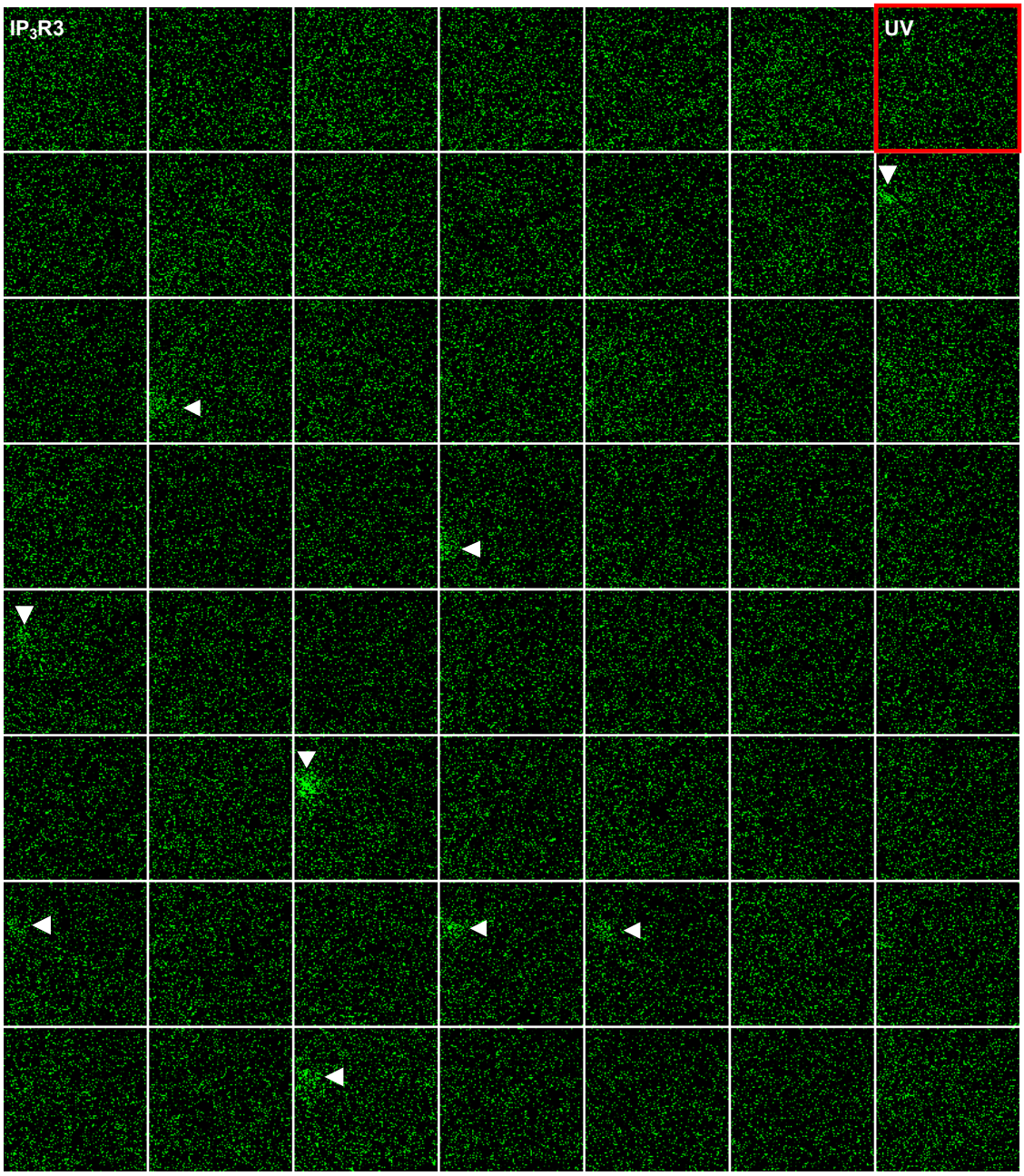

Figure 4.6C: Flash photolysis of ci-IP_3 in HEK cells expressing a single IP_3R subtype generates Ca^{2+} puffs. Typical TIRF images from HEK cells expressing **(A)** IP_3R1, **(B)** IP_3R2, or **(C)** IP_3R3 show fluorescence from part of each cell before and after photolysis of ci-IP_3. The first frame after the UV flash is highlighted in red. White arrows point to puffs detected using the Flika program (Ellefsen et al., 2014). Images were collected at 5.32ms intervals, with every 80th frame shown in the montage.

HEK cells expressing a single IP_3R subtype also evoked Ca^{2+} puffs (**Figure 4.6**). Although, Ca^{2+} puffs have been observed in cells in which particular subtypes predominate (IP_3R1 in SH-SY5Y (Smith et al., 2009a, Smith et al., 2009b)), this is the first time (to my knowledge) that signals mediated by single IP_3R subtypes have been imaged and compared side-by-side.

Unlike HEK WT cells, in which a 50ms UV flash always evoked a global increase in $[Ca^{2+}]_c$, HEK cells expressing a single IP_3R subtype experienced fewer global Ca^{2+} signals. 20% of HEK IP_3R1-expressing cells, and 13.3% of HEK IP_3R2-expressing cells had global Ca^{2+} signals, while there were none in HEK IP_3R3-expressing cells (**Figure 4.7A**). Additionally, the latent period for cells expressing a single IP_3R subtype is approximately three-times longer than that of HEK WT cells (**Figure 4.7B**).

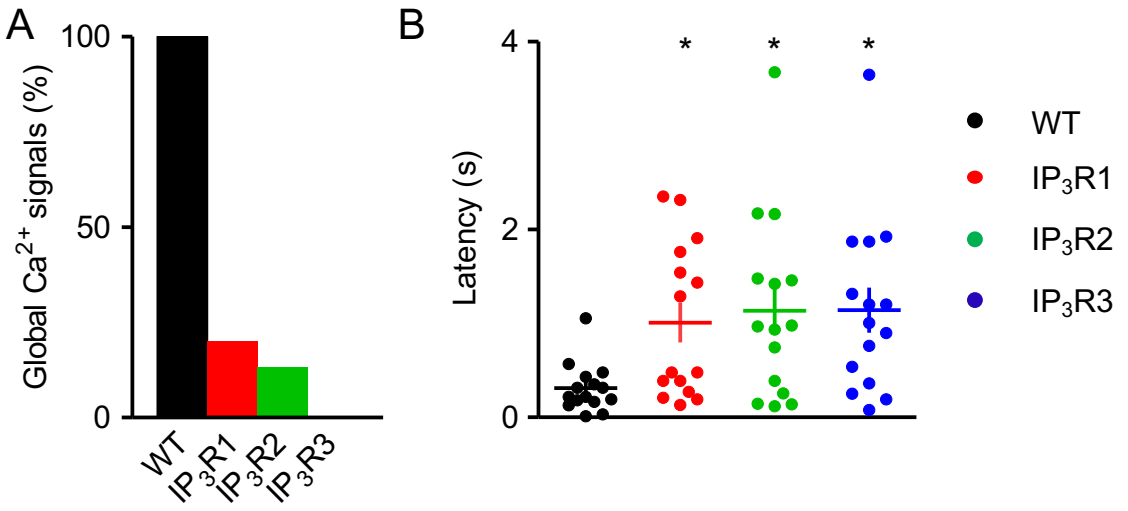

Figure 4.7: HEK cells expressing a single IP_3R subtype had fewer global signals. (A-B) Summary results for the indicated cell lines. **(A)** Shows the percentage of cells in which there was a global increase in $[Ca^{2+}]_c$ within the recording interval. **(B)** Latency from the UV flash to the first detected Ca^{2+} puff. $^{*}p < 0.05$, Kruskal-Wallis test with Dunn's correction relative to WT cells. The colour code applies to both panels.

4.3.2 Cells with more IP_3R have more Ca^{2+}-release sites

As soon as global signals invaded the cell, it became impossible to identify Ca^{2+} puffs. Since the interval between the UV-flash and occurrence of a global Ca^{2+} signal varied between cell lines (**Figure 4.7A**), the useful recording interval varied between cell lines. However, if recordings from cells expressing a single IP_3R subtype were terminated to match recording intervals from WT cells, there would be too few Ca^{2+} puffs to analyse. For that reason, recordings where global signals invaded the cell were terminated when there was a 10% increase in global $[Ca^{2+}]_c$. Although i-IP_3, the compound released by photolysis of ci-IP_3, is more metabolically stable than IP_3 (Dakin and Li, 2007), it was necessary to check that that i-IP_3 is not degraded during the 40s analysis period. The frequency of Ca^{2+} puffs throughout the whole recording interval was uniform in cell lines (**Figure 4.8**). This result, indicating that Ca^{2+} puffs occur with uniform frequency across the recording period, validated my comparisons of the four cell lines.

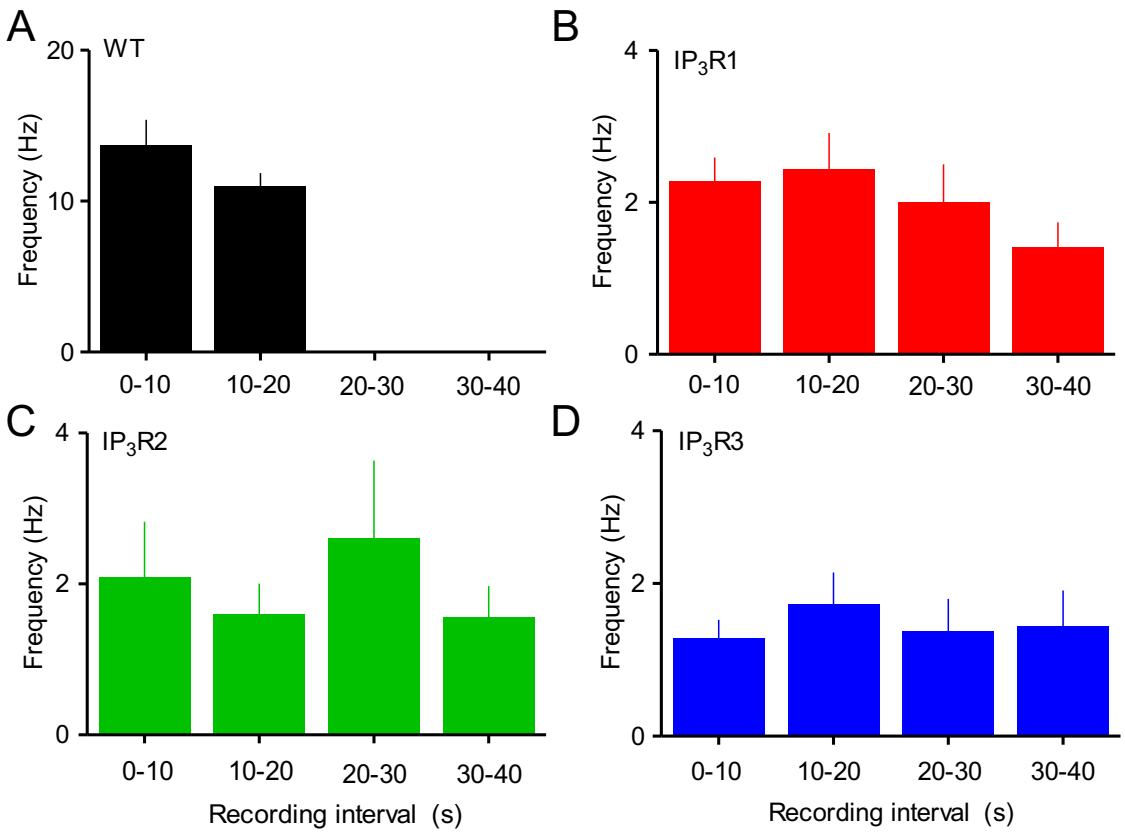

Figure 4.8: Ca^{2+} puffs occurred with uniform frequency throughout the recording interval. Frequency of Ca^{2+} puffs detected in each 10s recording interval in HEK **(A)** WT, **(B)** IP_3R1, **(C)** IP_3R2 and **(D)** IP_3R3. Ca^{2+} puffs contributed to the analysis only if they occurred after the average latent period of each cell line until the end of the recording at either 40s or until the Ca^{2+} signal invaded the cell. There were no significant differences between values determined in the later time intervals relative to the first interval (Kruskal-Wallis with Dunn's test, $p < 0.05$).

The frequency of Ca^{2+} puffs was greater in WT cells than in cells expressing single IP_3R subtypes, although they could be recorded for longer from the latter because they took longer to initiate global Ca^{2+} signals (**Figure 4.3A, 4.6A-C** and **Figure 4.9A**).

HEK cells expressing a single IP_3R subtype express only a third as many IP_3R as HEK WT cells (**Figure 2.16**). It was, therefore important to establish whether the cell lines differed in the number of sites at which Ca^{2+} puffs occur.

Ca^{2+}-release sites are located at fixed positions and can be revisited (Smith et al., 2009b, Keebler and Taylor, 2017, Thillaiappan et al., 2017). As a result, more puffs provide more opportunities to discover a new Ca^{2+}-site. Puffs detected in my analyses were about ten-times more abundant than reported in other studies of different cell types (Nakamura et al., 2012; Smith and Parker, 2009; Thomas et al., 2000). The difference in total number of Ca^{2+} puffs detected is unlikely to be due to the mis-indentification of Ca^{2+} puffs. It is more likely to be due to the improved detection of Ca^{2+} puffs arising from automated analysis and the longer recording intervals (Keebler and Taylor, 2017, Thillaiappan et al., 2017).

Fortuitously, the total number of puffs detected in HEK WT cells was similar to the numbers detected in cells expressing single subtypes (**Figure 4.9B** and **Figure 4.10**). Since the total number of puffs was similar across the cell lines, I compared the number of sites detected across the different cell lines. HEK WT cells have almost twice the number found in cells expressing single IP_3R subtypes (**Figure 4.9C**). This indicates that cells with more IP_3Rs have more Ca^{2+}-release sites.

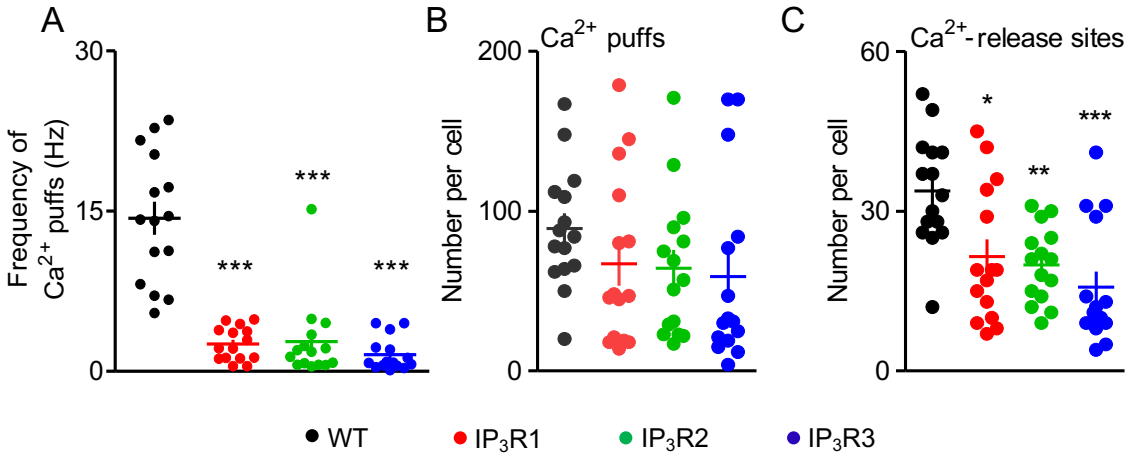

Figure 4.9: HEK cells expressing a single IP_3R subtype have fewer Ca^{2+}-release sites. (A-C) Show summary results for the indicated cell lines. **(A)** Frequency of Ca^{2+} puffs occurring within the entire recording region. **(B)** Number of puffs detected per cell and **(C)** the number of sites detected per cell. All panels show mean ± s.e.m., and the individual mean values from 15 cells. $^{*}p < 0.05$, $^{**}p < 0.01$, $^{***}p < 0.001$, Kruskal-Wallis test with Dunn's correction relative to WT cells.

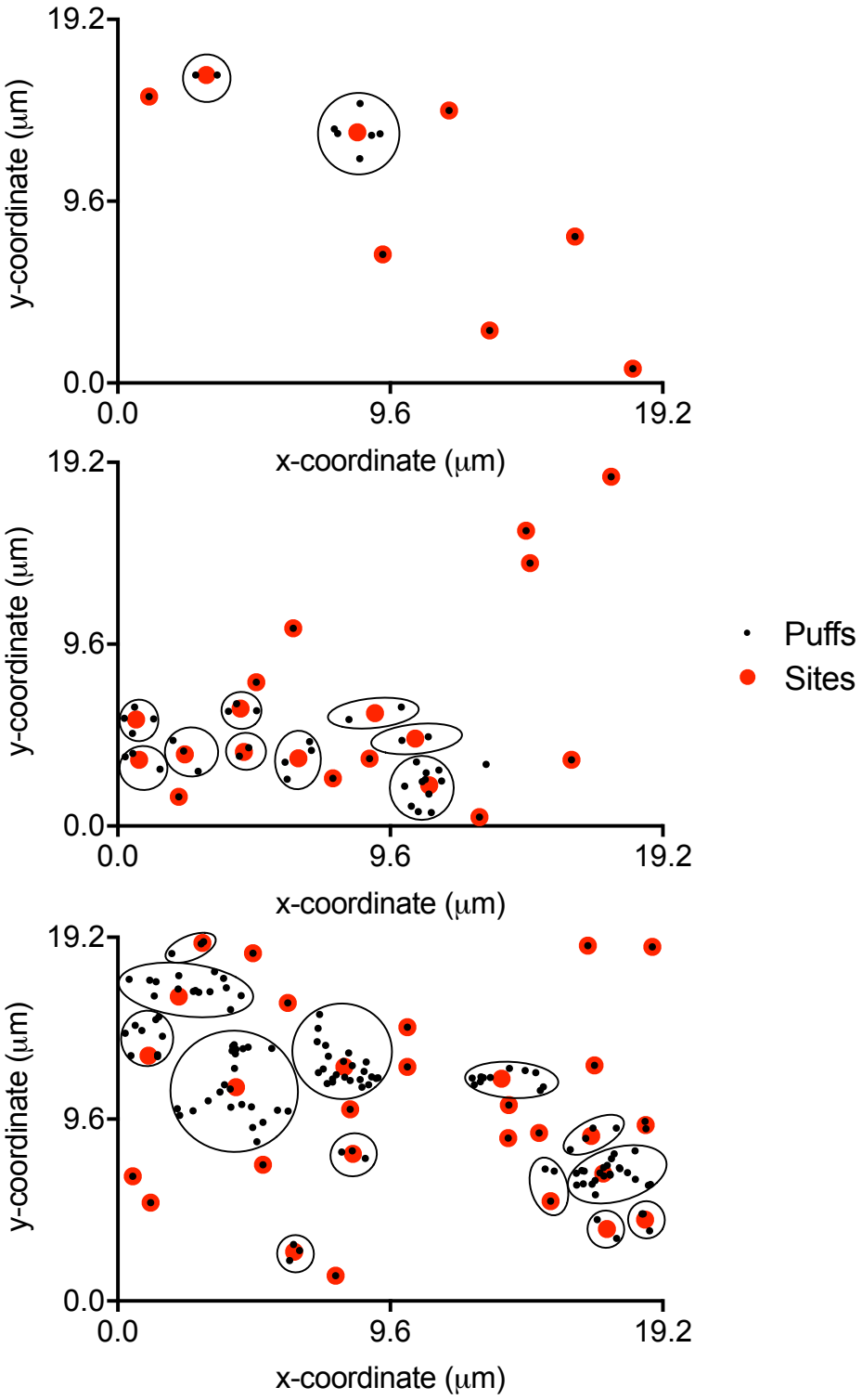

Figure 4.10: Examples of how Ca^{2+} puffs were grouped into sites from three representative cells. Shows the x- and y- coordinates of Ca^{2+} puffs (black) and Ca^{2+} sites (red). The events shown were detected and analysed using Flika.

Since there are a limited number of fixed Ca^{2+}-sites (Keebler and Taylor, 2017), each successive Ca^{2+} puff during a recording is less likely to discover a new site than preceding Ca^{2+} puffs were. This provided another approach to validate that the number of puffs detected in each cell line was sufficient to discover all the Ca^{2+}-release sites. Each recording was divided into four bins, of 10s intervals for the cells expressing single IP_3R subtypes, and of 2s intervals for WT cells. A mono-exponential curve was fitted to describe the mean number of newly discovered sites in each bin versus time. The half-times for the decay in the discovery of new Ca^{2+}-sites in cells expressing single IP_3R subtypes ranged between 3.76s and 5.53s (**Figure 4.11A**). and for WT cells the half-time was 2.01s (**Figure 4.11B**). Thus, throughout the recording interval (>4 half-lives), I should be able to identify most (~94%) of the Ca^{2+}-release sites. I conclude that the fewer sites detected in cells expressing a single IP_3R subtype are not due to inadequate sampling. I conclude that cells with fewer IP_3Rs have fewer Ca^{2+}-release sites.

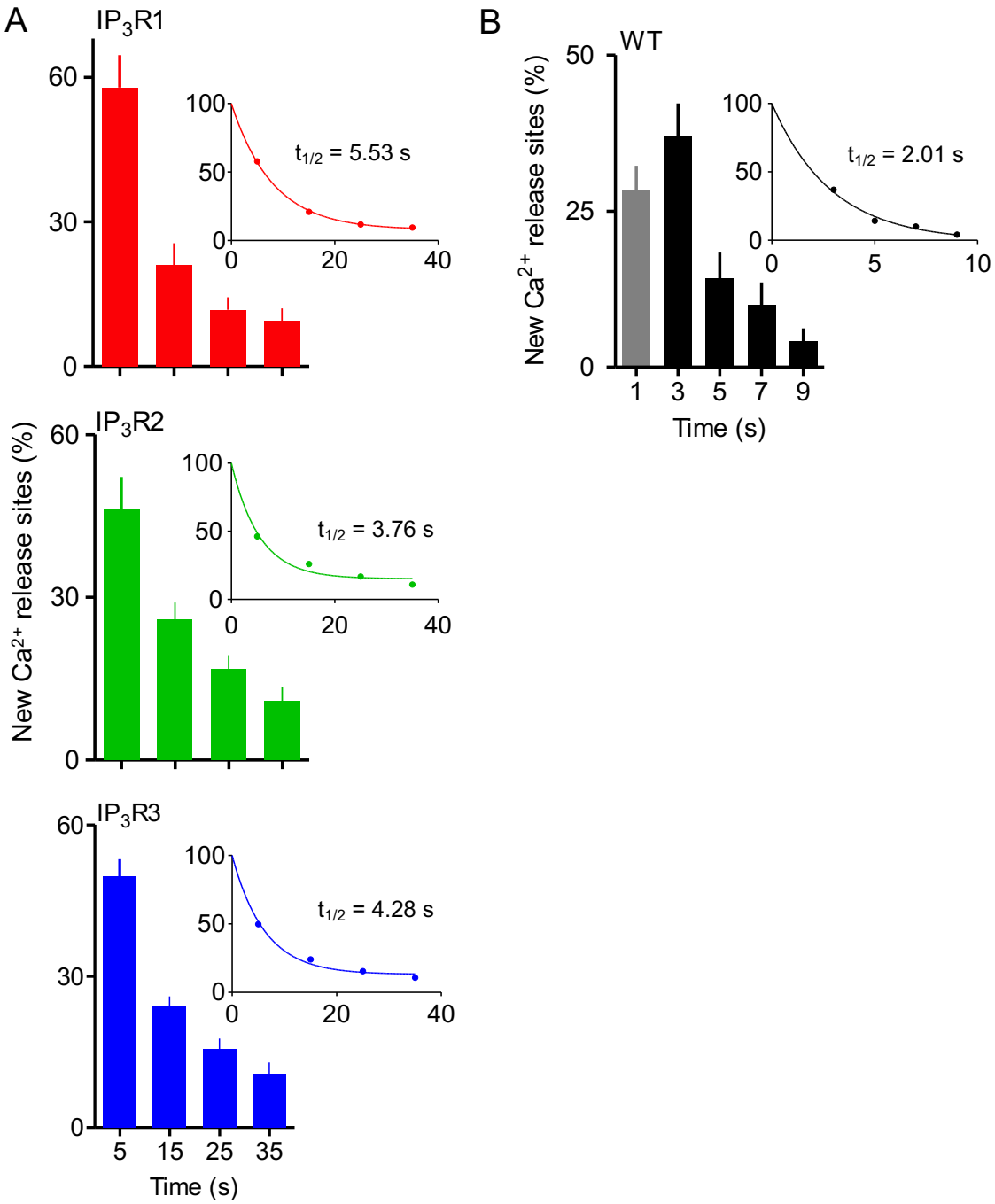

Figure 4.11: **Cells with fewer IP_3R subtypes have fewer Ca^{2+}-release sites** **(A)** Recordings from cells expressing a single IP_3R subtype were divided into four 10s bins, with each bin showing the number of new Ca^{2+}-release sites identified. Insets show exponential one-phase decay curves and half-times. **(B)** A similar analysis was conducted for WT cells, but recordings were divided to 2s bins to accommodate the more frequent puffs. The grey bin includes a variable latency during which there were no Ca^{2+} puffs.

4.3.3 Ca^{2+} signals evoked by different IP_3R subtypes have similar kinetic properties

The mean rise-times, decay-times and durations (duration at half-maximal amplitude) of Ca^{2+} puff and their frequency distributions were compared for each cell line. The mean rise times (~20ms), decay times (~30ms) and durations at half-maximal amplitude (~30ms) were similar in WT cells and in cells expressing only IP_3R1 or IP_3R3 (**Figure 4.12A & B**, **Figure 4.13A & B** and **Figure 4.14A & B**). These properties are comparable to analyses performed in SH-SY5Y cells (Smith et al., 2009a, Wiltgen et al., 2014, Lock et al., 2017), and in previous studies of a different HEK cell line, where the relative expression of the three IP_3R subtypes was different from the cells used in my study (Keebler and Taylor, 2017).

The kinetics of IP_3R2-mediated Ca^{2+} signals were significantly different from those determined in the other cell lines (**Figure 4.12B**, **Figure 4.13B** and **Figure 4.14B**). In IP_3R2-expressing cells, the mean rise time of 44.6 ± 4.7ms, mean decay time 53.1 ± 5.0ms and mean duration at half-maximal amplitude were significantly longer (62.6 ± 5.6ms) (**Figure 4.12B**, **Figure 4.13B** and **Figure 4.14B**) than in WT cells. The differences seem to be largely attributable to an extended tail in the IP_3R2 frequency distributions (**Figure 4.12A**, **Figure 4.13A** and **Figure 4.14A**).

With variability in the total number of puffs observed in each cell (**Figure 4.9B**), I asked whether there were any obvious differences in the properties of Ca^{2+} puffs in the most and least active cells. I therefore selected five cells from each cell line, spanning the full range of Ca^{2+} puff activity, and compared the frequency distributions of the properties of their Ca^{2+} puffs. There were no systematic differences between the most and least active cells in the durations, rise times and decay times (**Figure 4.15-4.17**).

I conclude that different IP_3R subtypes generate Ca^{2+} puffs with broadly similar characteristics and that IP_3R2-mediated Ca^{2+} puffs typically last about twice as long as Ca^{2+} events mediated by IP_3R1, IP_3R3 or native mixtures of IP_3R subtypes.

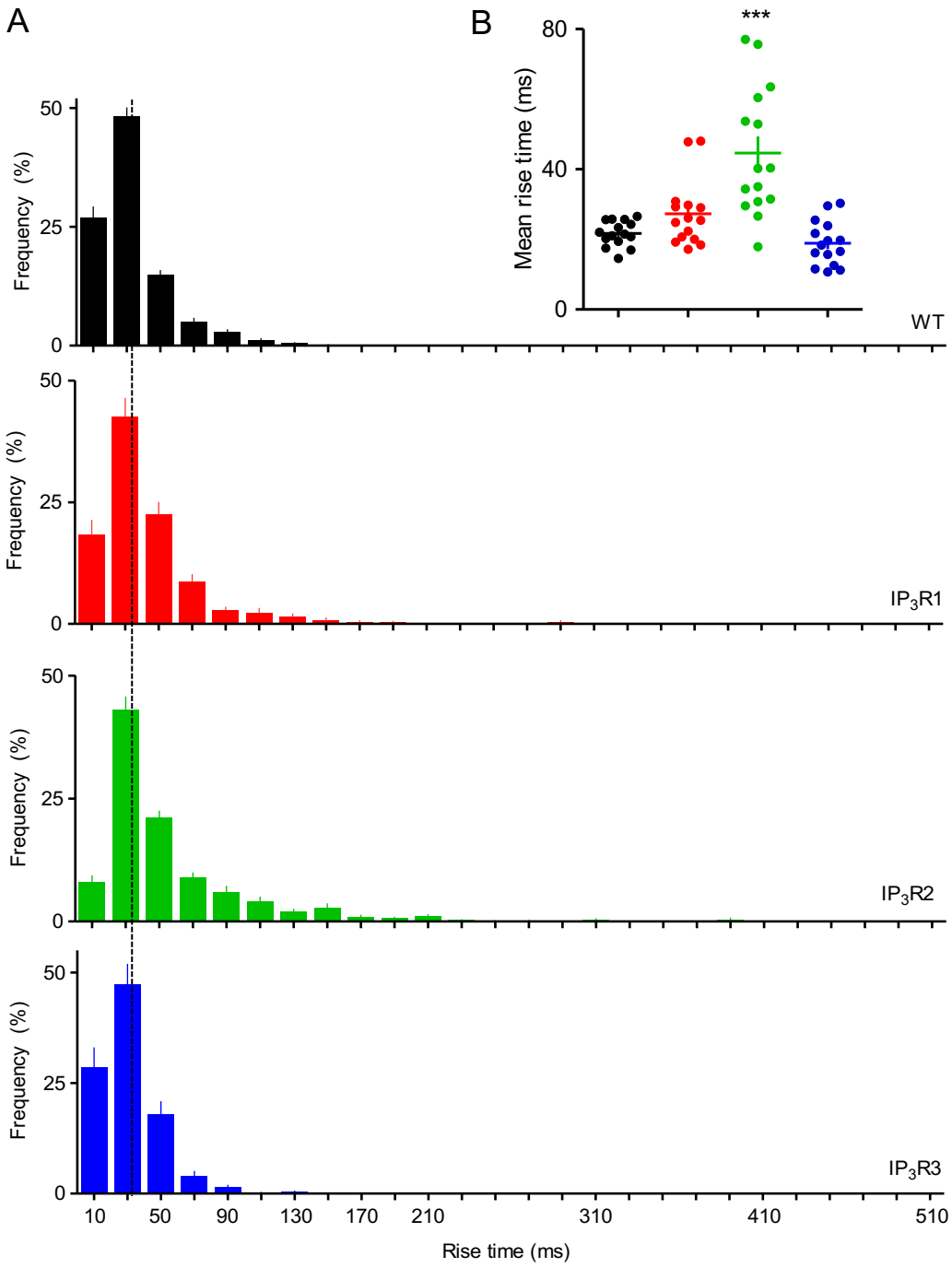

Figure 4.12: IP_3R2-mediated Ca^{2+} puffs have longer rise times. (A) Frequency distributions of rise times of Ca^{2+} puffs occurring within the entire recording region. For Ca^{2+} puffs evoked by photolysis of ci-IP_3 in each cell line, the rise times (time for fluorescence to increase from 20% to 100% of its peak amplitude) were measured. The mean value for WT cells is shown by the dashed line. Results (mean ± s.e.m., n = 15 cells) show the frequency for each 20ms time-bin. Summary data in **(B)** show mean values for each of 15 cells for each cell line (~1000 puffs analysed for each cell line), and the mean ± s.e.m. of these values ***$p < 0.001$, Kruskal-Wallis test with Dunn's correction relative to WT cells.

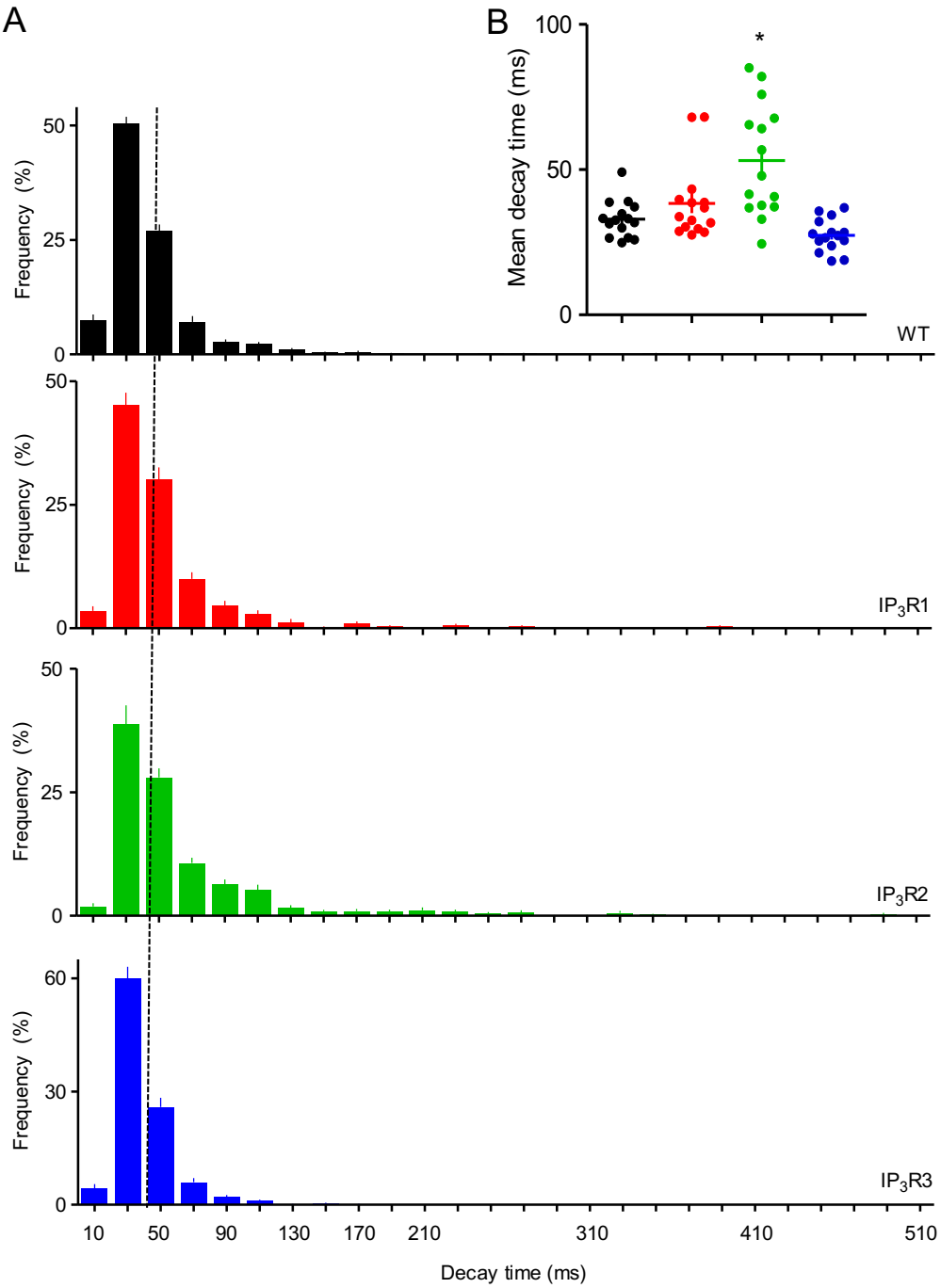

Figure 4.13: IP_3R2-mediated Ca^{2+} puffs have longer decay times. (**A**) Frequency distributions of decay times of Ca^{2+} puffs occurring within the entire recording region. For Ca^{2+} puffs evoked by photolysis of ci-IP_3 in each cell line, the decay times (time for fluorescence to decrease from 100% to 20% of its peak amplitude) were measured. The mean value for WT cells is shown by the dashed line. Results (mean ± s.e.m., n = 15 cells) show the frequency for each 20ms time-bin. Summary data in **(B)** show mean values for each of 15 cells for each cell line (~1000 puffs analysed for each cell line), and the mean ± s.e.m. of these values *$p < 0.05$, Kruskal-Wallis test with Dunn's correction relative to WT cells.

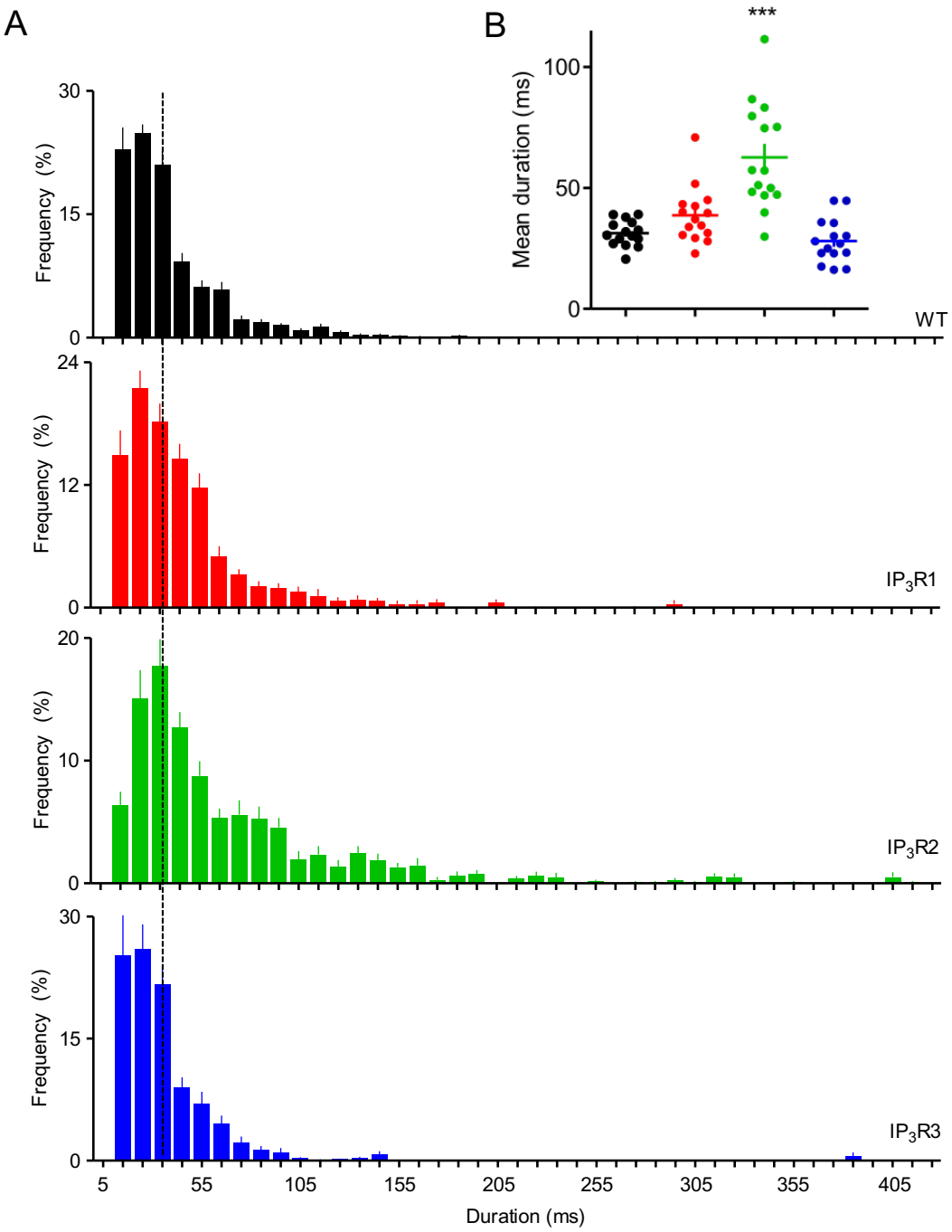

Figure 4.14: IP_3R2-mediated Ca^{2+} puffs have longer durations. (**A)** Frequency distributions of decay times of Ca^{2+} puffs occurring within the entire recording region. For Ca^{2+} puffs evoked by photolysis of ci-IP_3 in each cell line, the duration (width at half peak amplitude) were measured. The mean value for WT cells is shown by the dashed line. Results (mean ± s.e.m., n = 15 cells) show the frequency for each 20ms time-bin. Summary data in **(B)** show mean values for each of 15 cells for each cell line (~1000 puffs analysed for each cell line), and the mean ± s.e.m. of these values ***p < 0.001, Kruskal-Wallis test with Dunn's correction relative to WT cells.

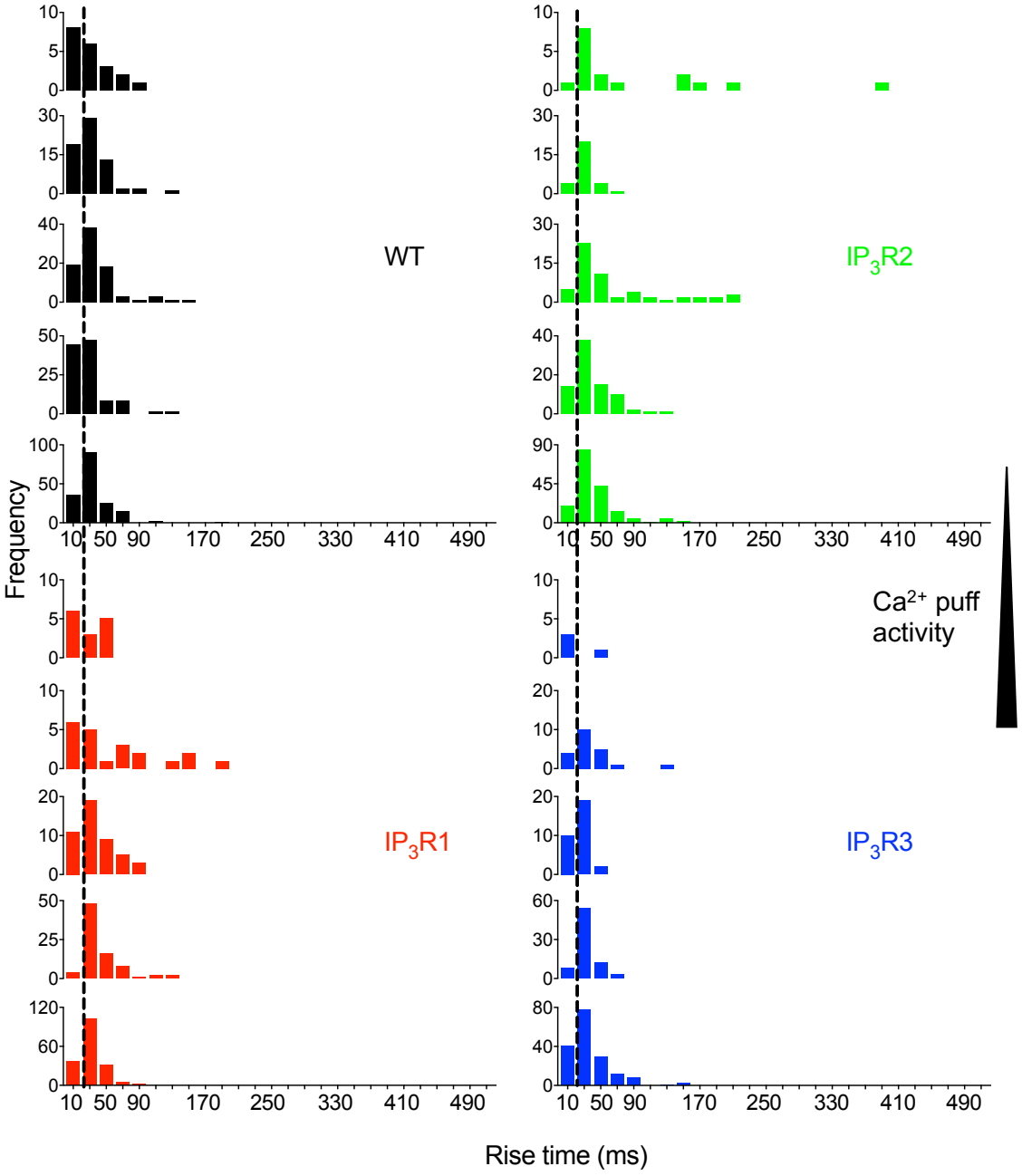

Figure 4.15: Frequency distributions for rise times are similar in cells of ranging Ca^{2+} puff activities. Five cells per cell line were selected to represent a range of Ca^{2+} puff activities, ranging from least active (top) to most active (bottom). Frequency distributions (20ms bins) of rise times of Ca^{2+} puffs occurring within the entire recording region. Dashed lines show the mean value for wild-type cells.

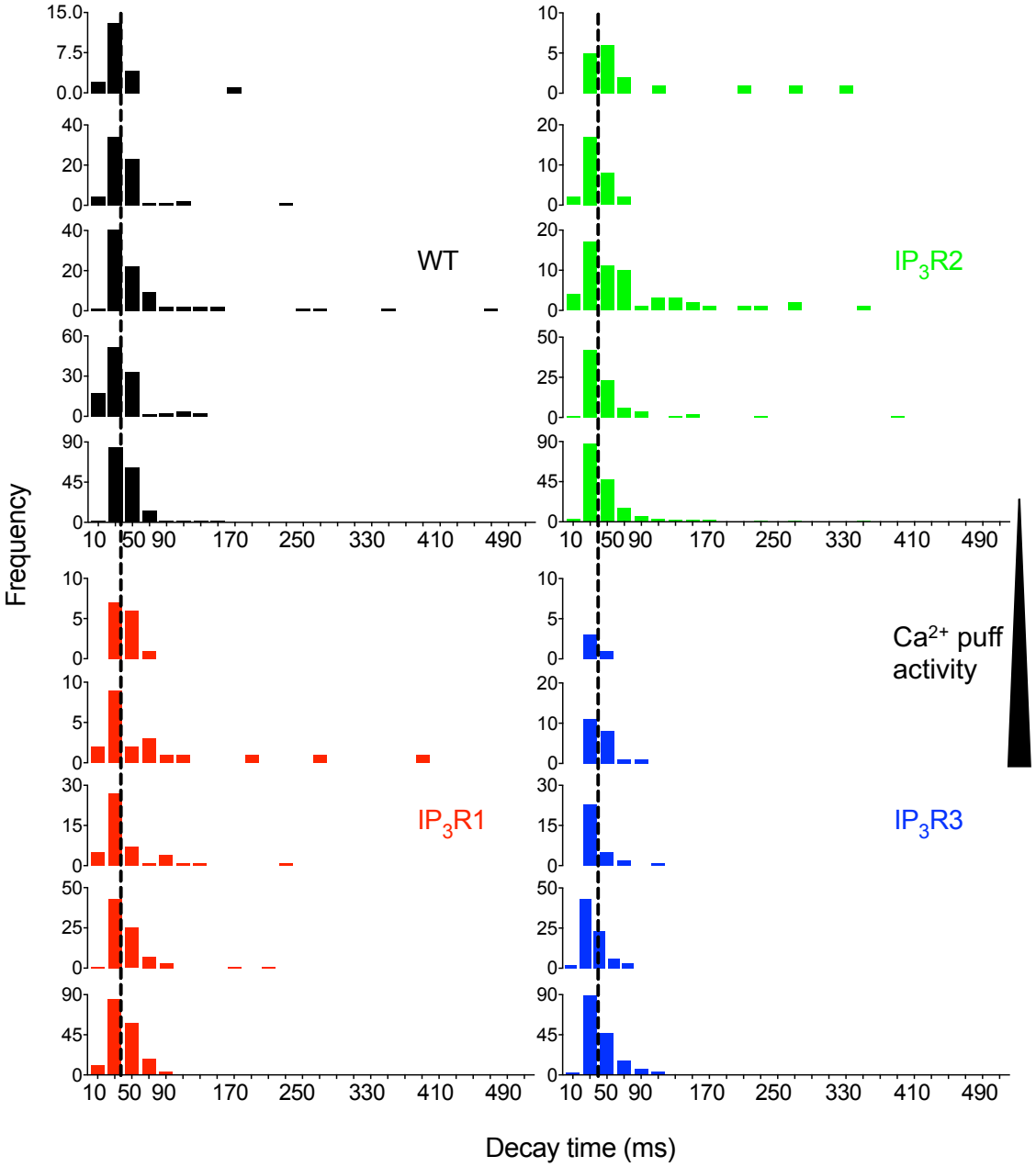

Figure 4.16: Frequency distributions for decay times are similar in cells of ranging Ca^{2+} puff activities. Five cells per cell line were selected to represent a range of Ca^{2+} puff activities, ranging from least active (top) to most active (bottom). Frequency distributions (20ms bins) of decay times of Ca^{2+} puffs occurring within the entire recording region. Dashed lines show the mean value for wild-type cells.

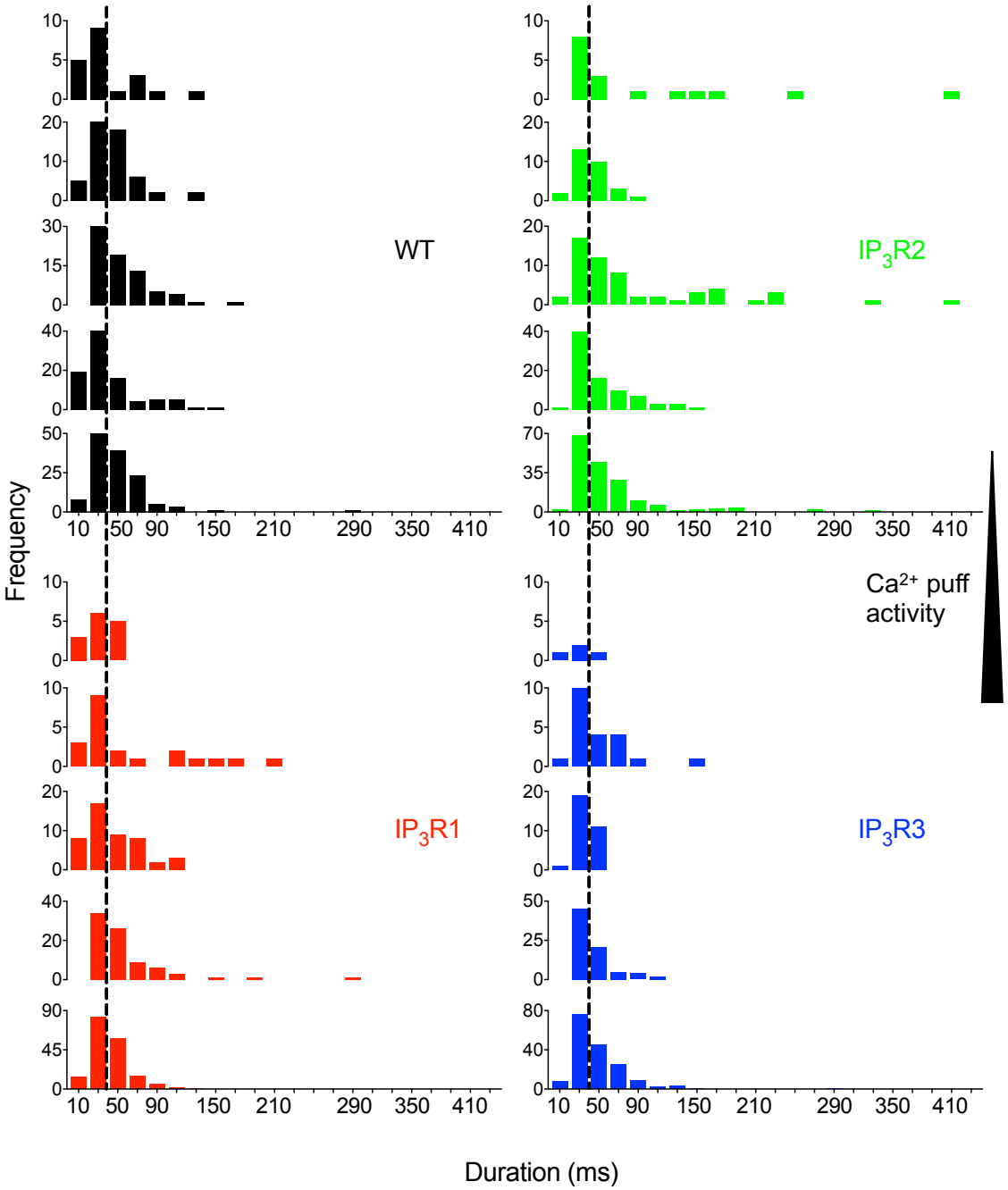

Figure 4.17: Frequency distributions for durations are similar in cells of ranging Ca^{2+} puff activities. Five cells per cell line were selected to represent a range of Ca^{2+} puff activities, ranging from least active (top) to most active (bottom). Frequency distributions (20ms bins) of durations of Ca^{2+} puffs occurring within the entire recording region. Dashed lines show the mean value for wild-type cells.

4.3.4 A similar number of active IP_3Rs contribute to Ca^{2+} puffs mediated by different IP_3R subtypes

I next considered whether the number of active channels in a Ca^{2+} puff differs between different IP_3R subtypes. Using highly temporally resolved Ca^{2+} imaging, it is sometimes possible to resolve unitary channel closures during the falling phase of Ca^{2+} puffs (Smith and Parker, 2009, Parker and Smith, 2010, Wiltgen et al., 2014). By using a 5.32ms frame rate, it was possible to resolve single channel closures in the falling phases of puffs evoked by all IP_3R subtypes (**Figure 4.13**).

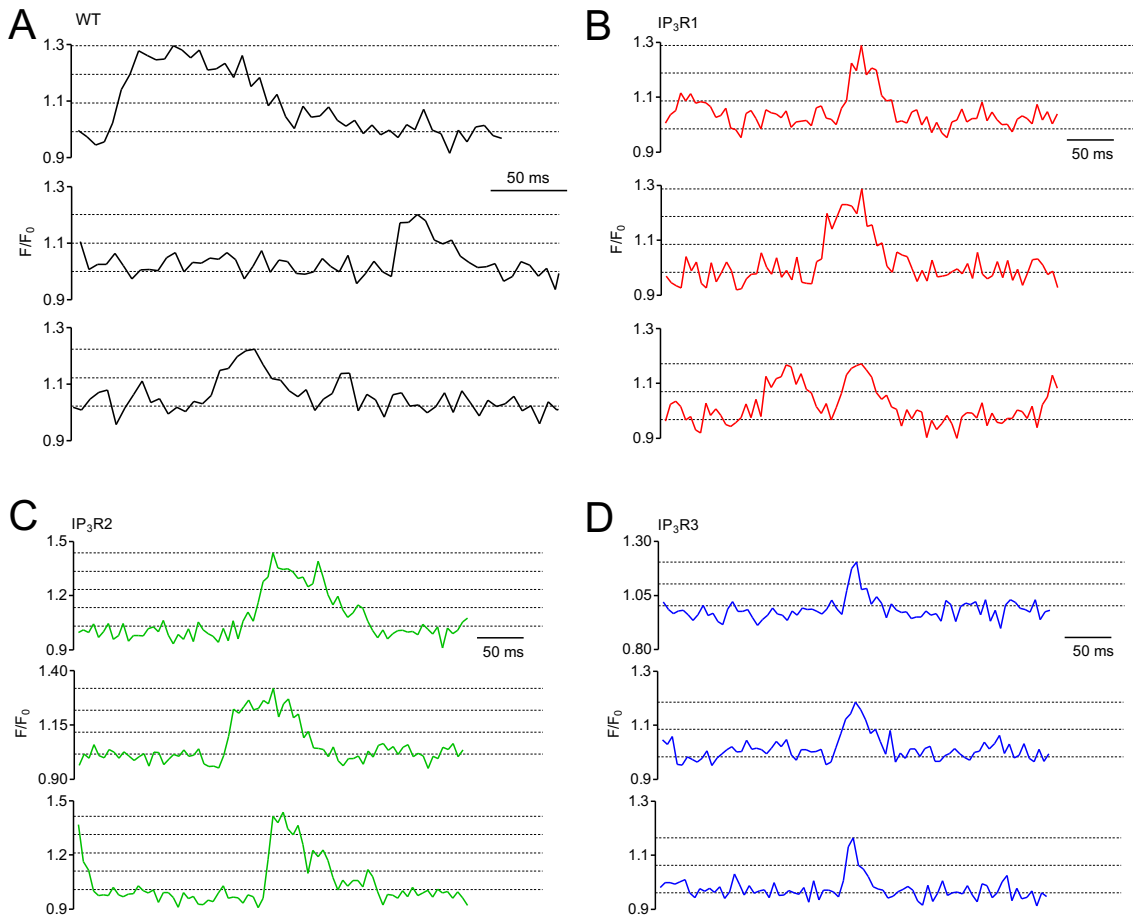

Figure 4.18: Unitary channel closures can sometimes be resolved during the falling phase of Ca^{2+} puffs. Typical examples of Ca^{2+}puffs from HEK **(A)** WT, **(B)** IP_3R1, **(C)** IP_3R2 and **(D)** IP_3R3 cells showing discrete fluorescence steps in their decay time. Dashed lines show the unitary steps.

The unitary steps during the falling phase of *n* = 10 puffs (per cell line) were measured to determine the mean unitary amplitude, which was similar for each cell line (**Figure 4.19A**). This suggests that in all cell lines, active IP_3Rs are distributed similarly within the TIRF field (within ~100nm from the interface). However, this needs additional analyses where IP_3R distribution across different cell lines is compared using an antibody that interacts equally with all three subtypes. Although, the AbC used in Western blot analyses proved useful, it failed to work in immunostaining analyses. In HEK 3KO cells, there was considerable staining with AbC, suggesting a lack of specificity in these analyses (**Figure 2.18**). Thus, I was unable to further interrogate the distribution of IP_3Rs in these cell lines. In addition, my results are consistent with single-channel recordings, indicating that different IP_3R subtypes have similar cation conductances (Ramos-Franco et al., 1998a, Vais et al., 2010).

Using the mean unitary amplitude from all cells ($\Delta F/F_0$ = 0.101 ± 0.002, n = 40), it was possible to estimate the number of active channels (N) that contribute to each Ca^{2+} puff: (N = $\frac{Puff\ amplitude}{Mean\ unitary\ amplitude}$). **Figure 4.19B** shows that the mean number of active channels in HEK WT and IP_3R3 cells is ~2.7. This agrees with observations from HeLa cells where most Ca^{2+} puffs contained less than seven active channels (Thillaiappan et al., 2017) and SH-SY5Y cells (Smith et al., 2009a).

Frequency distributions from Ca^{2+} puffs in all cell lines show a skewed distribution of events, with many small events and fewer large events (**Figure 4.20)**. The number of active channels are significantly different for IP_3R1- and IP_3R2- expressing cells (**Figure 4.19B** and **Figure 4.20**) but the differences are small. The mean number of active channels per puff in IP_3R2-expressing cells was ~3.2 (**Figure 4.19B**) and in IP_3R1-expressing cells it was 2.3 (**Figure 4.19B**). These results are consistent with observations that native clusters of IP_3Rs include an average of eight IP_3Rs (Thillaiappan et al., 2017).

Data in **Figure 4.21** show that frequency distributions of Ca^{2+} puff amplitudes from less active and more active cells are similar.

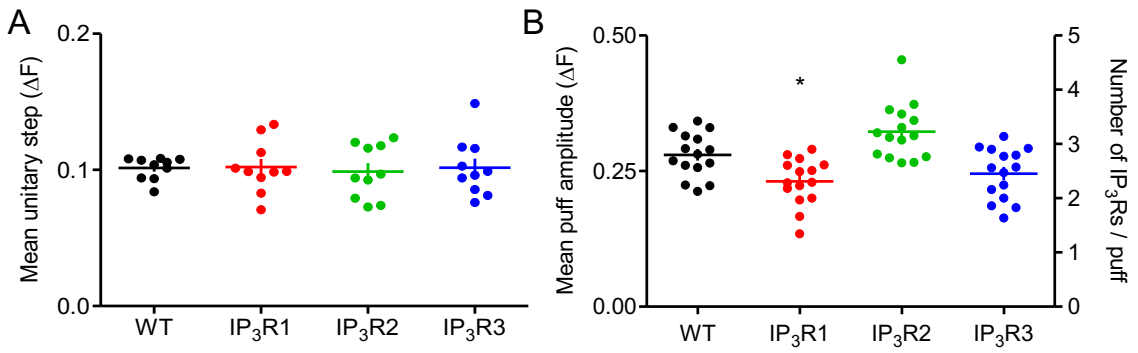

Figure 4.19: Amplitudes of Ca^{2+} puffs evoked by a single IP_3R subtype. (A) Summary results (mean ± s.e.m. *n* = 10 puffs from different cells) of the mean unitary step fluorescence. $p > 0.05$ using Kruskal-Wallis test with Dunn's correction between each cell line. (B) Summary results (mean ± s.e.m. *n* = 15 cells) show the mean puff amplitude and the estimated number of active channels of Ca^{2+} puffs occurring within the entire recording region. $^*p < 0.05$, Kruskal-Wallis test with Dunn's correction relative to WT cells.

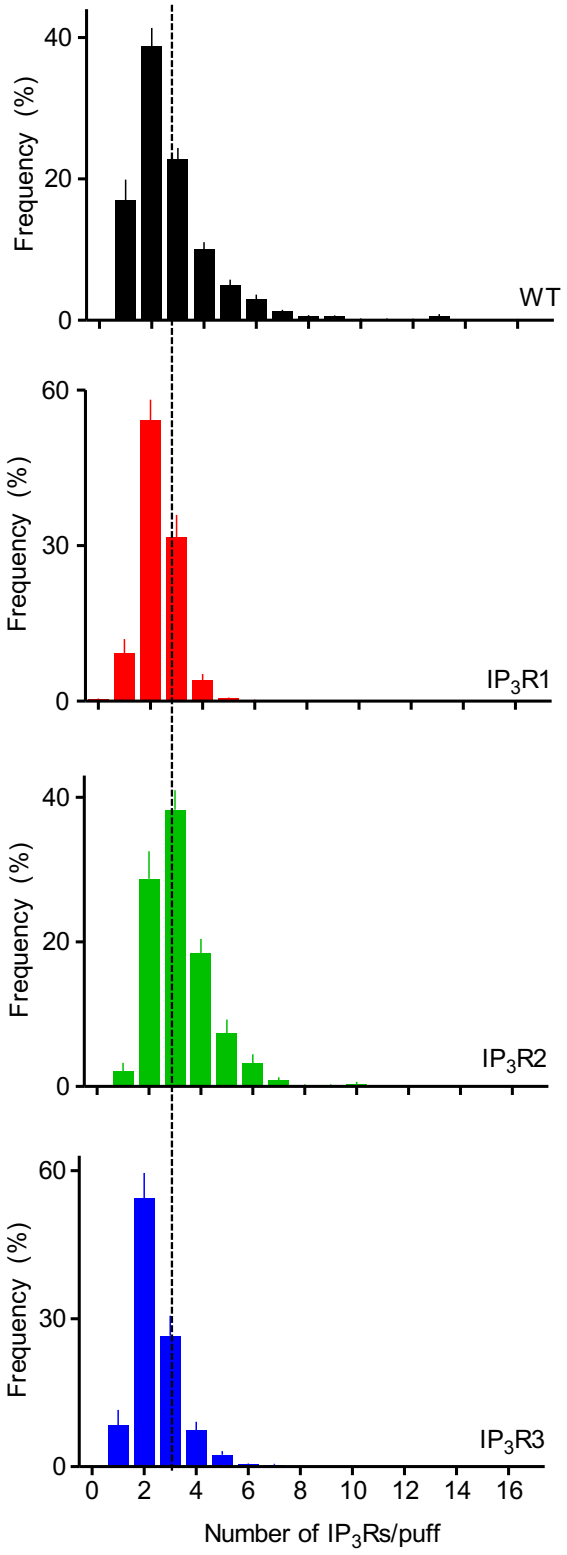

Figure 4.20: Frequency distributions of the number of active IP_3Rs in each Ca^{2+} puff. Shows frequency distributions of the estimated number of active channels in a Ca^{2+} puff for each cell line. Data are mean ± s.e.m., *n* = 15 cells. The dashed line shows the mean number of active channels for events in WT cells.

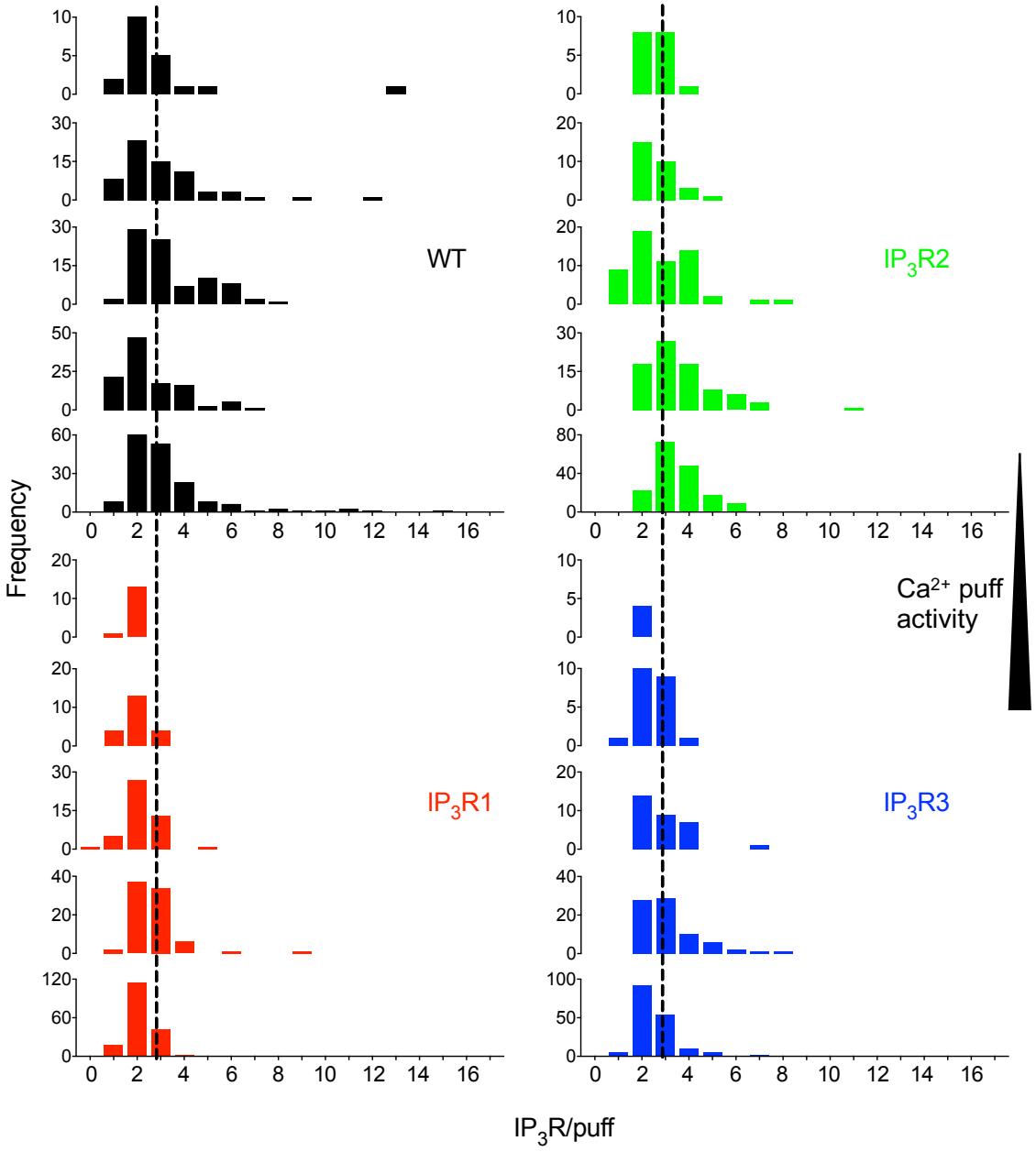

Figure 4.21: Amplitude frequency distributions of less active and more active cells are similar. Five cells per cell line were selected to represent a range of Ca^{2+} puff activities, ranging from least active (top) to most active (bottom). Frequency distributions of the estimated number of active channels contributing to Ca^{2+} puffs detected within the entire recording region. Dashed lines show the mean value for wild-type cells.

4.4 Conclusions

Previous analyses in cell lines in which different IP_3R subtypes predominate suggested that Ca^{2+} puffs are the building blocks of IP_3-evoked Ca^{2+} signals (Rooney et al., 1990, Kasai et al., 1993, Yao et al., 1995, Bootman et al., 1997a, Simpson et al., 1997, Smith and Parker, 2009, Nakamura et al., 2012, Keebler and Taylor, 2017). My aim was to determine whether all three IP_3R subtypes can generate Ca^{2+} puffs.

The only previous study to have used imaging techniques to examine the contribution of single IP_3Rs used genetically engineered DT40 cells to systematically compare the Ca^{2+} signalling patterns mediated by different IP_3R subtypes (Miyakawa et al., 1999). They showed that DT40 cells expressing single IP_3R subtypes generate different global Ca^{2+} signals. Activation of cell-surface receptors in DT40 WT, DT40-IP_3R1 and DT40-IP_3R2 cells evoked repeated Ca^{2+} oscillations, while the responses were monophasic in DT40-IP_3R3 cells. These cells, however, are not amenable to analysis by optical patch-clamp methods because they have so little cytoplasm and provide poor TIRF footprints. Ca^{2+} puffs have not, therefore, been examined in DT40 cells.

I used HEK cells in which CRISPR/Cas9 had been used to disrupt expression of IP_3R genes and so provide cell lines expressing single IP_3R subtypes (Alzayady et al., 2016). These were compared with the maternal WT cell line. I used identical high-resolution TIRF analyses and exactly the same stimulation regimes to compare the Ca^{2+} puffs evoked in each of these cell lines by photolysis of ci-IP_3.

Even though the cells were subjected to the same stimulus, global Ca^{2+} signals differed significantly between the cell lines. All HEK WT cells experienced global Ca^{2+} signals whereas, only ~20% of IP_3R1- or IP_3R2- expressing cells had a global increase in $[Ca^{2+}]_c$, at least within the 40s recording interval. A difference between HEK WT cells and cells expressing a single IP_3R subtype is that WT cells have approximately three times more IP_3Rs. The greater propensity of WT cells to initiate global changes in $[Ca^{2+}]_c$ may be due to them expressing more

IP_3Rs. Since there were also more Ca^{2+}-release sites in HEK WT cells, it may be that Ca^{2+} signals can spread more easily between sites by CICR in WT cells.

Overall the similarities between the Ca^{2+} signals evoked by different IP_3R subtypes are striking. Unitary channel amplitudes were indistinguishable between the different cell lines, consistent with each subtype having a similar single-channel conductance (Ramos-Franco et al., 1998b, Vais et al., 2010). This suggests that active channels are uniformly distributed in the TIRF field, but further analyses are required to strengthen this conclusion (Mataragka and Taylor, 2018). Additionally, and consistent with previous analyses (Smith et al., 2009a, Thillaiappan et al., 2017), my results suggest that IP_3Rs come close to the plasma membrane to mediate Ca^{2+} signals.

The results described in this chapter also show that the number of active IP_3Rs contributing to a Ca^{2+} event is similar in all cell lines. This finding suggests that across a wide range of IP_3R expression levels, IP_3Rs are assembled into similarly sized clusters, with more clusters in cells expressing more IP_3Rs. From this, I conclude that clusters from which Ca^{2+} puffs originate are not random associations, but instead there is a mechanism, common for all IP_3R subtypes, that ensures that similarly sized clusters are formed across a range of IP_3R expression levels (Mataragka and Taylor, 2018).

The kinetic properties of Ca^{2+} puffs in HEK WT cells and cells either expressing IP_3R1 or IP_3R3 are very similar. However, puffs evoked by IP_3R2 are significantly more long-lasting. Although the mechanisms contributing to this discrepancy are not known, it is plausible that differences in the kinetic properties are due to the greater affinity of IP_3R2 for IP_3 (Iwai et al., 2007). This may be of great importance, as it suggests that dissociation of IP_3 from the active channel may have an important role in the termination of IP_3-evoked Ca^{2+} signals, but additional studies are needed to validate this hypothesis.

In summary, this is the first clear demonstration that all IP_3R subtypes use Ca^{2+} puffs with strikingly similar characteristics as building blocks for IP_3-evoked Ca^{2+} signals (Mataragka and Taylor, 2018).

Chapter 5: Concluding remarks

In Chapter 2, I characterised a haploid (HAP1) cell line lacking IP_3Rs (generated by the Horizon Discovery Group). The HAP1 cells that I obtained, expressed either single IP_3R subtypes, a combination of subtypes, or were devoid of IP_3Rs. I initially validated that IP_3R2 KO and IP_3R3 KO HAP1 cells lacked their cognate IP_3R. I did, however, have concerns regarding the HAP1 IP_3R1 KO cell lines. In my screening, I used a C-terminal anti-IP_3R1 antibody (S1) that had been validated in DT-40 cells expressing single mammalian IP_3R subtypes (Saleem et al., 2012). Using this antibody, I detected a band that corresponded in size to IP_3R1. My concern was the presence of C-terminal IP_3R1 fragments, which was important to resolve as C-terminal IP_3R fragments can oligomerise with native IP_3Rs and render results uninterpretable. During my work, Prof. D. Yule's group was successful in generating a HEK 3-KO cell line. The results I obtained with the S1 antibody in HEK 3-KO cells were consistent with the results from HAP1 cells. After additional tests with S1 and a commercial C-terminal anti-IP_3R1 antibody (Ab1) and in collaboration with Prof. Yule, I concluded that HAP1 IP_3R1 cells and HEK 3-KO both lacked the IP_3R1 protein. In addition, I was able to verify that each cell line lacked its cognate subtype (HAP1 double and 3-KO). Hence, I was in possession of two mammalian systems lacking IP_3Rs that I could use to study IP_3-evoked Ca^{2+} events. The fact that IP_3-evoked Ca^{2+} events had been characterised in a different HEK WT cell line (Keebler and Taylor, 2017), their amenability to transfection and their morphology prompted me to continue my work with HEK cells.

In Chapter 3, I used the optical patch-clamp method (Smith et al., 2009a) to record IP_3-evoked Ca^{2+} signals at high temporal resolution. The large volume of data obtained using this method prohibited me from analysing my recordings manually. As a result, I optimised the use of Flika, a python-based program for the analysis of IP_3-evoked Ca^{2+} signals (Ellefsen et al., 2014), for my experiments and compared it to manual analysis. I showed that Flika is superior at detecting local Ca^{2+} signals compared to manual analysis. Flika has no user-bias, it quickly detects IP_3-evoked Ca^{2+} signals (even the faintest) and groups them into sites, it has an option in the end that allows further analysis of IP_3-evoked Ca^{2+} signals

and it automatically extracts puff properties. Users need to be careful, however, to not include any false-positives in their analysis.

In Chapter 4, I showed that all three IP_3R subtypes generate IP_3-evoked Ca^{2+} puffs. I used Flika to determine the properties of IP_3-evoked Ca^{2+} puffs mediated by different IP_3Rs (under the same stimulation regimes) and showed that they are similar across the three cell lines expressing a single IP_3R subtype. The unitary amplitudes of IP_3-evoked Ca^{2+} puffs mediated by different IP_3Rs were similar, suggesting that IP_3Rs in these cells are similarly distributed within the TIRF field (although this conclusion would be strengthened by immunostaining experiments using a common antibody). In comparison to IP_3R1- and IP_3R3-mediated Ca^{2+} signals, IP_3R2-mediated Ca^{2+} signals lasted longer and had higher mean amplitudes. The slower kinetics of IP_3R2-mediated Ca^{2+} signals might be due to the higher affinity of IP_3R2 for IP_3. This may point towards a mechanism of termination associated with dissociation of IP_3 from the receptor, but further experiments are needed to test this conclusion. Taking into account that HEK WT cells expressed three times more IP_3Rs that HEK cells expressing a single subtype, it is surprising that the mean amplitudes of IP_3-evoked Ca^{2+} puffs are similar. Based on that, I concluded that the IP_3R clusters that mediate IP_3-evoked Ca^{2+} puffs are assembled by a common mechanism, ensuring that similarly sized clusters are formed, independent of the level of IP_3R expression. I have shown, for the first time, that Ca^{2+} puffs are the universal building blocks for all IP_3-evoked Ca^{2+} signals.

Future work will attempt to identify which IP_3R features are most important in the termination of IP_3-evoked Ca^{2+} puffs. This can be done by manipulating the IP_3R structure in HEK 3-KO cells and assess the effects of mutations on the termination phase of IP_3-mediated Ca^{2+} events. Additionally, future work will attempt to determine the intracellular distribution of different IP_3Rs by gene-editing techniques. This has already been for IP_3R1 in HeLa cells, but the intracellular distribution of endogenously tagged IP_3R2 and IP_3R3 is not known.

References

ALBERTS, B. 2008. *Molecular biology of the cell,* New York, Garland Science.

ALZAYADY, K. J., WANG, L., CHANDRASEKHAR, R., WAGNER, L. E., 2ND, VAN PETEGEM, F. & YULE, D. I. 2016. Defining the stoichiometry of inositol 1,4,5-trisphosphate binding required to initiate Ca^{2+} release. *Science Signaling,* 9**,** ra35.

AXELROD, D. 2001. Total internal reflection fluorescence microscopy in cell biology. *Traffic,* 2**,** 764-74.

AXELROD, D., BURGHARDT, T. P. & THOMPSON, N. L. 1984. Total internal reflection microscopy. *Annual Review of Biophysics and Bioenergetics,* 13**,** 247-268.

BAKER, M. R., FAN, G. & SERYSHEVA, II 2017. Structure of IP_3R channel: high-resolution insights from cryo-EM. *Curr Opin Struct Biol,* 46**,** 38-47.

BARRANGOU, R., FREMAUX, C., DEVEAU, H., RICHARDS, M., BOYAVAL, P., MOINEAU, S., ROMERO, D. A. & HORVATH, P. 2007. CRISPR provides acquired resistance against viruses in prokaryotes. *Science,* 315**,** 1709-12.

BAUGHMAN, J. M., PEROCCHI, F., GIRGIS, H. S., PLOVANICH, M., BELCHER-TIMME, C. A., SANCAK, Y., BAO, X. R., STRITTMATTER, L., GOLDBERGER, O., BOGORAD, R. L., KOTELIANSKY, V. & MOOTHA, V. K. 2011. Integrative genomics identifies MCU as an essential component of the mitochondrial calcium uniporter. *Nature,* 476**,** 341-345.

BEDELL, V. M., WANG, Y., CAMPBELL, J. M., POSHUSTA, T. L., STARKER, C. G., KRUG, R. G., TAN, W. F., PENHEITER, S. G., MA, A. C., LEUNG, A. Y. H., FAHRENKRUG, S. C., CARLSON, D. F., VOYTAS, D. F., CLARK, K. J., ESSNER, J. J. & EKKER, S. C. 2012. In vivo genome editing using a high-efficiency TALEN system. *Nature,* 491**,** 114-U133.

BERRIDGE, M. J. 1993. Inositol trisphosphate and calcium signalling. *Nature (London),* 361**,** 315-325.

BERRIDGE, M. J. 2006. Calcium microdomains: organization and function. *Cell Calcium,* 40**,** 405-12.

BERRIDGE, M. J. 2016. The inositol trisphosphate/calcium signaling pathway in health and disease. *Physiological Reviews,* 96**,** 1261-1296.

BERRIDGE, M. J. & IRVINE, R. F. 1984. Inositol trisphosphate, a novel second messenger in cellular signal transduction. *Nature (London),* 312**,** 315-321.

BERRIDGE, M. J., LIPP, P. & BOOTMAN, M. D. 2000. The versatility and universality of calcium signalling. *Nature Reviews: Molecular Cell Biology,* 1**,** 11-21.

BETZENHAUSER, M. J., WAGNER, L. E., 2ND, PARK, H. S. & YULE, D. I. 2009. ATP regulation of type-1 inositol 1,4,5-trisphosphate receptor activity does not require walker A-type ATP-binding motifs. *Journal of Biological Chemistry,* 284**,** 16156-16163.

BHAYA, D., DAVISON, M. & BARRANGOU, R. 2011. CRISPR-Cas systems in bacteria and archaea: versatile small RNAs for adaptive defense and regulation. *Annu Rev Genet,* 45**,** 273-97.

BLAUSTEIN, M. P. & LEDERER, W. J. 1999. Sodium/calcium exchange: its physiological implications. *Physiological Reviews,* 79**,** 763-854.

BOEHNING, D. & JOSEPH, S. K. 2000. Direct association of ligand-binding and pore domains in homo- and heterotetrameric inositol 1,4,5-trisphosphate receptors. *European Molecular Biology Organisation Journal,* 19**,** 5450-5459.

BOEHNING, D., JOSEPH, S. K., MAK, D.-O., D. & FOSKETT, J. K. 2001. Single-channel recordings of recombinant inositol trisphosphate receptors in mammalian nuclear envelope. *Biophysical Journal,* 81**,** 117-124.

BOLOTIN, A., QUINQUIS, B., SOROKIN, A. & EHRLICH, S. D. 2005. Clustered regularly interspaced short palindrome repeats (CRISPRs) have spacers of extrachromosomal origin. *Microbiology,* 151**,** 2551-61.

BOOTMAN, M. D., BERRIDGE, M. J. & LIPP, P. 1997a. Cooking with calcium: the recipes for composing global signals from elementary events. *Cell,* 91**,** 367-373.

BOOTMAN, M. D., COLLINS, T. J., PEPPIATT, C. M., PROTHERO, L. S., MACKENZIE, L., DE SMET, P., TRAVERS, M., TOVEY, S. C., SEO, J. T., BERRIDGE, M. J., CICCOLINI, F. & LIPP, P. 2001. Calcium signalling--an overview. *Semin Cell Dev Biol,* 12**,** 3-10.

BOOTMAN, M. D., NIGGLI, E., BERRIDGE, M. J. & LIPP, P. 1997b. Imaging the hierarchical Ca^{2+} signalling system in HeLa cells. *Journal of Physiology,* 499**,** 307-314.

BOOTMAN, M. D., RIETDORF, K., COLLINS, T., WALKER, S. & SANDERSON, M. 2014. Ca^{2+}-sensitive fluorescent dyes and intracellular Ca^{2+} imaging. *Cold Spring Harbor Protocols.* Cold Spring Harbor Laboratory Press.

BOSANAC, I., MICHIKAWA, T., MIKOSHIBA, K. & IKURA, M. 2004. Structural insights into the regulatory mechanism of IP_3 receptor. *Biochimica et Biophysica Acta,* 1742**,** 89-102.

BRINI, M. & CARAFOLI, E. 2011. The plasma membrane Ca^{2+} ATPase and the plasma membrane sodium calcium exchanger cooperate in the regulation of cell calcium. *Cold Spring Harbor Perspectives in Biology,* 3.

BROOKER, G., SEKI, T., CROLL, D. & WAHLESTEDT, C. 1990. Calcium wave evoked by activation of endogenous or exogenously expressed receptors in Xenopus oocytes. *Proc Natl Acad Sci U S A,* 87**,** 2813-7.

CAI, L. Q., FISHER, A. L., HUANG, H. C. & XIE, Z. J. 2016. CRISPR-mediated genome editing and human diseases. *Genes & Diseases,* 3**,** 244-251.

CALLAMARAS, N. & PARKER, I. 2000. Phasic characteristics of elementary Ca^{2+} release sites underlies quantal responses to IP_3. *European Molecular Biology Organisation Journal,* 19**,** 3608-3617.

CARAFOLI, E. 1991. Calcium pump of the plasma membrane. *Physiological Reviews,* 71**,** 129-153.

CARDENAS, C., LIBERONA, J. L., MOLGO, J., COLASANTE, C., MIGNERY, G. A. & JAIMOVICH, E. 2005. Nuclear inositol 1,4,5-trisphosphate receptors regulate local Ca^{2+} transients and modulate cAMP response element binding protein phosphorylation. *Journal of Cell Science,* 118**,** 3131-3140.

CARDY, T. J. A., TRAYNOR, D. & TAYLOR, C. W. 1997. Differential regulation of types 1 and 3 inositol trisphosphate receptors by cytosolic Ca^{2+}. *Biochemical Journal,* 328**,** 785-793.

CARETTE, J. E., RAABEN, M., WONG, A. C., HERBERT, A. S., OBERNOSTERER, G., MULHERKAR, N., KUEHNE, A. I., KRANZUSCH, P. J., GRIFFIN, A. M., RUTHEL, G., DAL CIN, P., DYE, J. M., WHELAN, S. P., CHANDRAN, K. & BRUMMELKAMP, T. R. 2011. Ebola virus entry requires the cholesterol transporter Niemann-Pick C1. *Nature,* 477**,** 340-U115.

CATTERALL, W. A. 2011. Voltage-gated calcium channels. *Cold Spring Harbor Perspectives in Biology,* 3**,** a003947.

CEASAR, S. A., RAJAN, V., PRYKHOZHIJ, S. V., BERMAN, J. N. & IGNACIMUTHU, S. 2016. Insert, remove or replace: A highly advanced genome editing system using CRISPR/Cas9. *Biochim Biophys Acta,* 1863**,** 2333-44.

CHENG, H., LEDERER, W. J. & CANNELL, M. B. 1993. Calcium sparks. Elementary events underlying excitation-contraction coupling in heart muscle. *Science,* 262**,** 740-744.

CHOUDHARY, E., THAKUR, P., PAREEK, M. & AGARWAL, N. 2015. Gene silencing by CRISPR interference in mycobacteria. *Nat Commun,* 6**,** 6267.

CHRISTENSEN, K. A., MYERS, J. T. & SWANSON, J. A. 2002. pH-dependent regulation of lysosomal calcium in macrophages. *Journal of Cell Science,* 115**,** 599-607.

CHUA, J. J., SCHOB, C., REHBEIN, M., GKOGKAS, C. G., RICHTER, D. & KINDLER, S. 2012. Synthesis of two SAPAP3 isoforms from a single mRNA is mediated via alternative translational initiation. *Scientific Reports,* 2**,** 484.

CLAPHAM, D. E. 1995. Calcium signaling. *Cell,* 80**,** 259-268.

CLAPHAM, D. E. 2007. Calcium signaling. *Cell,* 131**,** 1047-1058.

CONG, L., RAN, F. A., COX, D., LIN, S., BARRETTO, R., HABIB, N., HSU, P. D., WU, X., JIANG, W., MARRAFFINI, L. A. & ZHANG, F. 2013. Multiplex genome engineering using CRISPR/Cas systems. *Science,* 339**,** 819-823.

CRADICK, T. J., FINE, E. J., ANTICO, C. J. & BAO, G. 2013. CRISPR/Cas9 systems targeting beta-globin and CCR5 genes have substantial off-target activity. *Nucleic Acids Res,* 41**,** 9584-92.

DAKIN, K. & LI, W. H. 2007. Cell membrane permeable esters of D-*myo*-inositol 1,4,5-trisphosphate. *Cell Calcium,* 42**,** 291-301.

DARGAN, S. L. & PARKER, I. 2003. Buffer kinetics shape the spatiotemporal patterns of IP_3-evoked Ca^{2+} signals. *Journal of Physiology,* 553**,** 775-788.

DELLIS, O., DEDOS, S., TOVEY, S. C., RAHMAN, T.-U.-., DUBEL, S. J. & TAYLOR, C. W. 2006. Ca^{2+} entry through plasma membrane IP_3 receptors. *Science,* 313**,** 229-233.

DEMURO, A. & PARKER, I. 2004. Imaging the activity and localization of single voltage-gated Ca^{2+} channels by total internal reflection fluorescence microscopy. *Biophysical Journal,* 86**,** 3250-3259.

DES GEORGES, A., CLARKE, O. B., ZALK, R., YUAN, Q., CONDON, K. J., GRASSUCCI, R. A., HENDRICKSON, W. A., MARKS, A. R. & FRANK, J. 2016. Structural Basis for Gating and Activation of RyR1. *Cell,* 167**,** 145-157 e17.

DEVEAU, H., BARRANGOU, R., GARNEAU, J. E., LABONTE, J., FREMAUX, C., BOYAVAL, P., ROMERO, D. A., HORVATH, P. & MOINEAU, S. 2008. Phage response to CRISPR-encoded resistance in Streptococcus thermophilus. *J Bacteriol,* 190**,** 1390-400.

DEVEAU, H., GARNEAU, J. E. & MOINEAU, S. 2010. CRISPR/Cas system and its role in phage-bacteria interactions. *Annu Rev Microbiol,* 64**,** 475-93.

DOLMAN, N. J. & TEPIKIN, A. V. 2006. Calcium gradients and the Golgi. *Cell Calcium,* 40**,** 505-12.

DOUDNA, J. A. & CHARPENTIER, E. 2014. Genome editing. The new frontier of genome engineering with CRISPR-Cas9. *Science,* 346**,** 1258096.

DRAWNEL, F. M., WACHTEN, D., MOLKENTIN, J. D., MAILLET, M., ARONSEN, J. M., SWIFT, F., SJAASTAD, I., LIU, N., CATALUCCI, D., MIKOSHIBA, K., HISATSUNE, C., OKKENHAUG, H., ANDREWS, S. R., BOOTMAN, M. D. & RODERICK, H. L. 2012. Mutual antagonism between IP_3RII and miRNA-133a
regulates calcium signals and cardiac hypertrophy. *Journal of Cell Biology,* 199**,** 783-798.

ECHEVARRIA, W., LEITE, M. F., GUERRA, M. T., ZIPFEL, W. R. & NATHANSON, M. H. 2003. Regulation of calcium signals in the nucleus by a nucleoplasmic reticulum. *Nature Cell Biology,* 5**,** 440-446.

EHRLICH, B. E. & WATRAS, J. 1988. Inositol 1,4,5-trisphosphate activates a channel from smooth muscle sarcoplasmic reticulum. *Nature (London),* 336**,** 583-586.

ELLEFSEN, K. L. & PARKER, I. 2018. Dynamic Ca^{2+} imaging with a simplified lattice light-sheet microscope: A sideways view of subcellular Ca^{2+} puffs. *Cell Calcium,* 71**,** 34-44.

ELLEFSEN, K. L., SETTLE, B., PARKER, I. & SMITH, I. F. 2014. An algorithm for automated detection, localization and measurement of local calcium signals from camera-based imaging. *Cell Calcium,* 56**,** 147-156.

ESSLETZBICHLER, P., KONOPKA, T., SANTORO, F., CHEN, D., GAPP, B. V., KRALOVICS, R., BRUMMELKAMP, T. R., NIJMAN, S. M. & BURCKSTUMMER, T. 2014. Megabase-scale deletion using CRISPR/Cas9 to generate a fully haploid human cell line. *Genome Research,* 24**,** 2059-2065.

FAN, G., BAKER, M. L., WANG, Z., BAKER, M. R., SINYAGOVSKIY, P. A., CHIU, W., LUDTKE, S. J. & SERYSHEVA, II 2015. Gating machinery of $InsP_3R$ channels revealed by electron cryomicroscopy. *Nature,* 527**,** 336-341.

FERRERI-JACOBIA, M., MAK, D.-O., D. & FOSKETT, J. K. 2005. Translational mobility of the type 3 inositol 1,4,5-trisphosphate receptor Ca^{2+} release channel in endoplasmic reticulum membrane. *Journal of Biological Chemistry,* 280**,** 3824-3831.

FILL, M. & COPELLO, J. A. 2002. Ryanodine receptor calcium release channels. *Physiological Reviews,* 82**,** 893-922.

FOREMAN, J. C., JOHANSEN, T. & GIBB, A. J. 2011. *Textbook of receptor pharmacology,* Boca Raton, FL, CRC Press.

FOSKETT, J. K., WHITE, C., CHEUNG, K. H. & MAK, D. O. 2007. Inositol trisphosphate receptor Ca^{2+} release channels. *Physiological Reviews,* 87**,** 593-658.

FRAIMAN, D. & DAWSON, S. P. 2004. A model of IP_3 receptor with a luminal calcium binding site: stochastic simulations and analysis. *Cell Calcium,* 35**,** 403-13.

FRISCHMEYER, P. A. & DIETZ, H. C. 1999. Nonsense-mediated mRNA decay in health and disease. *Hum Mol Genet,* 8**,** 1893-900.

FU, Y., FODEN, J. A., KHAYTER, C., MAEDER, M. L., REYON, D., JOUNG, J. K. & SANDER, J. D. 2013. High-frequency off-target mutagenesis induced by CRISPR-Cas nucleases in human cells. *Nat Biotechnol,* 31**,** 822-6.

FUJINO, I., YAMADA, N., MIYAWAKI, A., HASEGAWA, M., FURUICHI, T. & MIKOSHIBA, K. 1995. Differential expression of type 2 and type 3 inositol 1,4,5-trisphosphate receptor mRNAs in various mouse tissues: in situ hybridization study. *Cell and Tissue Research,* 280**,** 201-210.

FUKUDA, N., SHIRASU, M., SATO, K., EBISUI, E., TOUHARA, K. & MIKOSHIBA, K. 2008. Decreased olfactory mucus secretion and nasal abnormality in mice lacking type 2 and type 3 IP_3 receptors. *Eur J Neurosci,* 27**,** 2665-75.

FUKUSHIMA, M., TOMITA, T., JANOSHAZI, A. & PUTNEY, J. W. 2012. Alternative translation initiation gives rise to two isoforms of Orai1 with distinct plasma membrane mobilities. *Journal of Cell Science,* 125**,** 4354-4361.

FURUICHI, T., YOSHIKAWA, S., MIYAWAKI, A., WADA, K., MAEDA, M. & MIKOSHIBA, K. 1989. Primary structure and functional expression of the inositol 1,4,5-trisphosphate-binding protein P_{400}. *Nature (London),* 342**,** 32-38.

FUTATSUGI, A., NAKAMURA, T., YAMADA, M. K., EBISUI, E., NAKAMURA, K., UCHIDA, K., KITAGUCHI, T., TAKAHASHI-IWANAGA, H., NODA, T.,

ARUGA, J. & MIKOSHIBA, K. 2005. IP_3 receptor types 2 and 3 mediate exocrine secretion underlying energy metabolism. *Science,* 309**,** 2232-2234.

GALVAN, D. L., BORREGO-DIAZ, E., PEREZ, P. J. & MIGNERY, G. A. 1999. Subunit oligomerization, and topology of the inositol 1,4,5-trisphosphate receptor. *Journal of Biological Chemistry,* 274**,** 29483-29492.

GANDINI, M. A., SANDOVAL, A. & FELIX, R. 2014. Patch-clamp recording of voltage-sensitive Ca^{2+} channels. *Cold Spring Harb Protoc,* 2014**,** 329-5.

GARNEAU, J. E., DUPUIS, M. E., VILLION, M., ROMERO, D. A., BARRANGOU, R., BOYAVAL, P., FREMAUX, C., HORVATH, P., MAGADAN, A. H. & MOINEAU, S. 2010. The CRISPR/Cas bacterial immune system cleaves bacteriophage and plasmid DNA. *Nature,* 468**,** 67-71.

GASIUNAS, G., BARRANGOU, R., HORVATH, P. & SIKSNYS, V. 2012. Cas9-crRNA ribonucleoprotein complex mediates specific DNA cleavage for adaptive immunity in bacteria. *Proc Natl Acad Sci U S A,* 109**,** E2579-86.

GEES, M., OWSIANIK, G., NILIUS, B. & VOETS, T. 2012. TRP Channels. *Comprehensive Physiology,* 2**,** 563-608.

GERASIMENKO, O. V., GERASIMENKO, J. V., TEPIKIN, A. V. & PETERSEN, O. H. 1995. ATP-dependent accumulation and inositol trisphosphate- or cyclic ADP-ribose-mediated release of Ca^{2+} from the nuclear envelope. *Cell,* 80**,** 439-444.

GEYER, M., HUANG, F., SUN, Y., VOGEL, S. M., MALIK, A. B., TAYLOR, C. W. & KOMAROVA, Y. A. 2015. Microtubule-associated protein EB3 regulates IP_3 receptor clustering and Ca^{2+} signaling in endothelial cells. *Cell Reports,* 12**,** 79-89.

GILBERT, L. A., LARSON, M. H., MORSUT, L., LIU, Z., BRAR, G. A., TORRES, S. E., STERN-GINOSSAR, N., BRANDMAN, O., WHITEHEAD, E. H., DOUDNA, J. A., LIM, W. A., WEISSMAN, J. S. & QI, L. S. 2013. CRISPR-mediated modular RNA-guided regulation of transcription in eukaryotes. *Cell,* 154**,** 442-51.

GROFF, J. R. & SMITH, G. D. 2008. Ryanodine receptor allosteric coupling and the dynamics of calcium sparks. *Biophysical Journal,* 95**,** 135-154.

GROSCHE, J., MATYASH, V., MOLLER, T., VERKHRATSKY, A., REICHENBACH, A. & KETTENMANN, H. 1999. Microdomains for neuron-glia interaction: parallel fiber signaling to Bergmann glial cells. *Nat Neurosci,* 2**,** 139-43.

HAFT, D. H., SELENGUT, J., MONGODIN, E. F. & NELSON, K. E. 2005. A guild of 45 CRISPR-associated (Cas) protein families and multiple CRISPR/Cas subtypes exist in prokaryotic genomes. *Plos Computational Biology,* 1**,** 474-483.

HAGAR, R. E., BURGSTAHLER, A. D., NATHANSON, M. H. & EHRLICH, B. E. 1998. Type III $InsP_3$ receptor channel stays open in the presence of increased calcium. *Nature (London),* 296**,** 81-84.

HAGAR, R. E. & EHRLICH, B. E. 2000. Regulation of the Type III $InsP_3$ receptor by $InsP_3$ and ATP. *Biophysical Journal,* 79**,** 271-278.

HAMADA, K., MIYATAKE, H., TERAUCHI, A. & MIKOSHIBA, K. 2017. IP_3-mediated gating mechanism of the IP_3 receptor revealed by mutagenesis and X-ray crystallography. *Proceedings of the National Academy of Sciences USA,* 114**,** 4661-4666.

HATTORI, M., SUZUKI, A. Z., HIGO, T., MIYAUCHI, H., MICHIKAWA, T., NAKAMURA, T., INOUE, T. & MIKOSHIBA, K. 2004. Distinct roles of inositol 1,4,5-trisphosphate receptor types 1 and 3 in Ca^{2+} signaling. *Journal of Biological Chemistry,* 279**,** 11967-11975.

HINCH, R. 2004. A mathematical analysis of the generation and termination of calcium sparks. *Biophys J,* 86**,** 1293-307.

HISATSUNE, C., YASUMATSU, K., TAKAHASHI-IWANAGA, H., OGAWA, N., KURODA, Y., YOSHIDA, R., NINOMIYA, Y. & MIKOSHIBA, K. 2007. Abnormal taste perception in mice lacking the type 3 inositol 1,4,5-trisphosphate receptor. *J Biol Chem,* 282**,** 37225-31.

HORVATH, P. & BARRANGOU, R. 2010. CRISPR/Cas, the immune system of bacteria and archaea. *Science,* 327**,** 167-70.

HORVATH, P., COUTE-MONVOISIN, A. C., ROMERO, D. A., BOYAVAL, P., FREMAUX, C. & BARRANGOU, R. 2009. Comparative analysis of CRISPR loci in lactic acid bacteria genomes. *Int J Food Microbiol,* 131**,** 62-70.

HORVATH, P., ROMERO, D. A., COUTE-MONVOISIN, A. C., RICHARDS, M., DEVEAU, H., MOINEAU, S., BOYAVAL, P., FREMAUX, C. & BARRANGOU, R. 2008. Diversity, activity, and evolution of CRISPR loci in Streptococcus thermophilus. *J Bacteriol,* 190**,** 1401-12.

IINO, M. 1990. Biphasic Ca^{2+} dependence of inositol 1,4,5-trisphosphate-induced Ca^{2+} release in smooth muscle cells of the guinea pig taenia caeci. *Journal of General Physiology,* 95**,** 1103-1122.

ISHINO, Y., SHINAGAWA, H., MAKINO, K., AMEMURA, M. & NAKATA, A. 1987. Nucleotide sequence of the iap gene, responsible for alkaline phosphatase isozyme conversion in Escherichia coli, and identification of the gene product. *J Bacteriol,* 169**,** 5429-33.

IWAI, M., MICHIKAWA, T., BOSANAC, I., IKURA, M. & MIKOSHIBA, K. 2007. Molecular basis of the isoform-specific ligand-binding affinity of inositol 1,4,5-trisphosphate receptors. *J Biol Chem,* 282**,** 12755-64.

JAKOCIUNAS, T., BONDE, I., HERRGARD, M., HARRISON, S. J., KRISTENSEN, M., PEDERSEN, L. E., JENSEN, M. K. & KEASLING, J. D. 2015. Multiplex metabolic pathway engineering using CRISPR/Cas9 in Saccharomyces cerevisiae. *Metab Eng,* 28**,** 213-222.

JANSEN, R., EMBDEN, J. D., GAASTRA, W. & SCHOULS, L. M. 2002. Identification of genes that are associated with DNA repeats in prokaryotes. *Mol Microbiol,* 43**,** 1565-75.

JAYARAMAN, T. & MARKS, A. R. 1997. T cells deficient in inositol 1,4,5-trisphosphate receptor are resistant to apoptosis. *Molecular and Cellular Biology,* 17**,** 3005-3012.

JINEK, M., CHYLINSKI, K., FONFARA, I., HAUER, M., DOUDNA, J. A. & CHARPENTIER, E. 2012. A programmable dual-RNA-guided DNA endonuclease in adaptive bacterial immunity. *Science,* 337**,** 816-21.

JINEK, M., EAST, A., CHENG, A., LIN, S., MA, E. & DOUDNA, J. 2013. RNA-programmed genome editing in human cells. *Elife,* 2**,** e00471.

JOSEPH, S. K., BOEHNING, D., PIERSON, S. & NICCHITTA, C. V. 1997. Membrane insertion, glycosylation, and oligomerization of inositol trisphosphate receptors in a cell-free translation system. *Journal of Biological Chemistry,* 272**,** 1579-1588.

KAMER, K. J. & MOOTHA, V. K. 2015. The molecular era of the mitochondrial calcium uniporter. *Nature Reviews: Molecular Cell Biology,* 16**,** 545-553.

KASAI, H., LI, Y. X. & MIYASHITA, Y. 1993. Subcellular distribution of Ca^{2+} release channels underlying Ca^{2+} waves and oscillations in exocrine pancreas. *Cell,* 74**,** 669-677.

KEEBLER, M. V. 2015. *High-resolution analyses of inositol 1,4,5-trisphosphate receptor behaviour.* Doctor of Philosophy, University of Cambridge.

KEEBLER, M. V. & TAYLOR, C. W. 2017. Endogenous signalling pathways and caged IP_3 evoke Ca^{2+} puffs at the same abundant immobile intracellular sites. *J Cell Sci,* 130**,** 3728-3739.

KLEINSTIVER, B. P., PATTANAYAK, V., PREW, M. S., TSAI, S. Q., NGUYEN, N. T., ZHENG, Z. & JOUNG, J. K. 2016. High-fidelity CRISPR-Cas9 nucleases with no detectable genome-wide off-target effects. *Nature,* 529**,** 490-5.

KOCKSKAMPER, J., ZIMA, A. V., RODERICK, H. L., PIESKE, B., BLATTER, L. A. & BOOTMAN, M. D. 2008. Emerging roles of inositol 1,4,5-trisphosphate signaling in cardiac myocytes. *J Mol Cell Cardiol,* 45**,** 128-47.

KONERMANN, S., BRIGHAM, M. D., TREVINO, A. E., JOUNG, J., ABUDAYYEH, O. O., BARCENA, C., HSU, P. D., HABIB, N., GOOTENBERG, J. S., NISHIMASU, H., NUREKI, O. & ZHANG, F. 2015. Genome-scale transcriptional activation by an engineered CRISPR-Cas9 complex. *Nature,* 517**,** 583-8.

LARSON, M. H., GILBERT, L. A., WANG, X., LIM, W. A., WEISSMAN, J. S. & QI, L. S. 2013. CRISPR interference (CRISPRi) for sequence-specific control of gene expression. *Nat Protoc,* 8**,** 2180-96.

LAUDE, A. J., TOVEY, S. C., DEDOS, S., POTTER, B. V. L., LUMMIS, S. C. R. & TAYLOR, C. W. 2005. Rapid functional assays of recombinant IP_3 receptors. *Cell Calcium,* 38**,** 45-51.

LI, J. F., NORVILLE, J. E., AACH, J., MCCORMACK, M., ZHANG, D., BUSH, J., CHURCH, G. M. & SHEEN, J. 2013. Multiplex and homologous recombination-mediated genome editing in Arabidopsis and Nicotiana benthamiana using guide RNA and Cas9. *Nat Biotechnol,* 31**,** 688-91.

LI, W., SCHULTZ, C., LLOPIS, J. & TSIEN, R. Y. 1997. Membrane-permeant esters of inositol polyphosphates, chemical syntheses and biological applications. *Tetrahedron,* 53**,** 12017-12040.

LI, W.-H., LLOPIS, J., WHITNEY, M., ZLOKARNIK, G. & TSIEN, R. Y. 1998. Cell-permeant caged $InsP_3$ ester shows that Ca^{2+} spike frequency can optimize gene expression. *Nature (London),* 392**,** 936-941.

LI, X., ZIMA, A. V., SHEIKH, F., BLATTER, L. A. & CHEN, J. 2005. Endothelin-1-induced arrhythmogenic Ca^{2+} signaling is abolished in atrial myocytes of inositol-1,4,5-trisphosphate (IP_3)-receptor type 2-deficient mice. *Circulation Research,* 96**,** 1274-1281.

LILLESTØL, R. K., REDDER, P., GARRETT, R. A. & BRÜGGER, K. 2006. A putative viral defence mechanism in archaeal cells. *Archaea,* 2**,** 59-72.

LIOU, J., KIM, M. L., HEO, W. D., JONES, J. T., MYERS, J. W., FERRELL, J. E., JR. & MEYER, T. 2005. STIM is a Ca^{2+} sensor essential for Ca^{2+}-store-depletion-triggered Ca^{2+} influx. *Current Biology,* 15**,** 1235-1241.

LIPP, P. & NIGGLI, E. 1998. Fundamental calcium release events revealed by two-photon excitation photolysis of caged calcium in Guinea-pig cardiac myocytes. *J Physiol,* 508 (Pt 3)**,** 801-9.

LOCK, J. T., ELLEFSEN, K. L., SETTLE, B., PARKER, I. & SMITH, I. F. 2015a. Imaging local Ca^{2+} signals in cultured mammalian cells. *Journal of Visualized Experiments*.

LOCK, J. T., PARKER, I. & SMITH, I. F. 2015b. A comparison of fluorescent Ca^{2+} indicators for imaging local Ca^{2+} signals in cultured cells. *Cell Calcium,* 58**,** 638-648.

LOCK, J. T., SMITH, I. F. & PARKER, I. 2017. Comparison of Ca^{2+} puffs evoked by extracellular agonists and photoreleased IP_3. *Cell Calcium,* 63**,** 43-47.

MAEDA, N., KAWASAKI, T., NAKADE, S., YOKOTA, N., TAGUCHI, T., KASAI, M. & MIKOSHIBA, K. 1991. Structural and functional characterization of inositol 1,4,5-trisphosphate receptor channel from mouse cerebellum. *Journal of Biological Chemistry,* 266**,** 1109-1116.

MAK, D.-O., D. & FOSKETT, J. K. 1998. Effects of divalent cations on single-channel conduction properties of *Xenopus* IP_3 receptor. *American Journal of Physiology,* 275**,** C179-C188.

MAK, D.-O., D., MCBRIDE, S., RAGHIRAM, V., YUE, Y., JOSEPH, S. K. & FOSKETT, J. K. 2000. Single-channel properties in endoplasmic reticulum membrane of recombinant type 3 inositol trisphosphate receptor. *Journal of General Physiology,* 115**,** 241-255.

MAK, D. O. & FOSKETT, J. K. 2015. Inositol 1,4,5-trisphosphate receptors in the endoplasmic reticulum: A single-channel point of view. *Cell Calcium,* 58**,** 67-78.

MAKAROVA, K. S., ARAVIND, L., GRISHIN, N. V., ROGOZIN, I. B. & KOONIN, E. V. 2002. A DNA repair system specific for thermophilic Archaea and bacteria predicted by genomic context analysis. *Nucleic Acids Res,* 30**,** 482-96.

MAKAROVA, K. S., GRISHIN, N. V., SHABALINA, S. A., WOLF, Y. I. & KOONIN, E. V. 2006. A putative RNA-interference-based immune system in prokaryotes: computational analysis of the predicted enzymatic machinery, functional analogies with eukaryotic RNAi, and hypothetical mechanisms of action. *Biol Direct,* 1**,** 7.

MALI, P., YANG, L., ESVELT, K. M., AACH, J., GUELL, M., DICARLO, J. E., NORVILLE, J. E. & CHURCH, G. M. 2013. RNA-guided human genome engineering via Cas9. *Science,* 339**,** 823-6.

MANDEGAR, M. A., HUEBSCH, N., FROLOV, E. B., SHIN, E., TRUONG, A., OLVERA, M. P., CHAN, A. H., MIYAOKA, Y., HOLMES, K., SPENCER, C. I., JUDGE, L. M., GORDON, D. E., ESKILDSEN, T. V., VILLALTA, J. E., HORLBECK, M. A., GILBERT, L. A., KROGAN, N. J., SHEIKH, S. P., WEISSMAN, J. S., QI, L. S., SO, P. L. & CONKLIN, B. R. 2016. CRISPR Interference Efficiently Induces Specific and Reversible Gene Silencing in Human iPSCs. *Cell Stem Cell,* 18**,** 541-53.

MAQUAT, L. E. 2004. Nonsense-mediated mRNA decay: splicing, translation and mRNP dynamics. *Nat Rev Mol Cell Biol,* 5**,** 89-99.

MARCHANT, J. S. & PARKER, I. 2001. Role of elementary Ca^{2+} puffs in generating repetitive Ca^{2+} oscillations. *European Molecular Biology Organisation Journal,* 20**,** 65-76.

MARSHALL, I. C. B. & TAYLOR, C. W. 1993. Biphasic effects of cytosolic calcium on Ins(1,4,5)P_3-stimulated Ca^{2+} mobilization in hepatocytes. *Journal of Biological Chemistry,* 268**,** 13214-13220.

MATARAGKA, S. & TAYLOR, C. W. 2018. All three IP_3 receptor subtypes generate Ca^{2+} puffs, the universal building blocks of IP_3-evoked Ca^{2+} signals. *J Cell Sci* 131 (16).

MATSUMOTO, M., NAKAGAWA, T., INOUE, T., NAGATA, E., TANAKA, K., TAKANO, H., MINOWA, O., KUNO, J., SAKAKIBARA, S., YAMADA, M., YONESHIMA, H., MIYAWAKI, A., FUKUUCHI, Y., FURUICHI, T., OKANO, H., MIKOSHIBA, K. & NODA, T. 1996. Ataxia and epileptic seizures in mice lacking type 1 inositol 1,4,5-trisphosphate receptor. *Nature (London),* 379**,** 168-171.

MATTHEYSES, A. L., SIMON, S. M. & RAPPOPORT, J. Z. 2010. Imaging with total internal reflection fluorescence microscopy for the cell biologist. *J Cell Sci,* 123**,** 3621-8.

MENDES, C. C., GOMES, D. A., THOMPSON, M., SOUTO, N. C., GOES, T. S., GOES, A. M., RODRIGUES, M. A., GOMEZ, M. V., NATHANSON, M. H. & LEITE, M. F. 2005. The type III inositol 1,4,5-trisphosphate receptor preferentially transmits apoptotic Ca^{2+} signals into mitochondria. *Journal of Biological Chemistry,* 280**,** 40892-40900.

MIYAKAWA, T., MAEDA, A., YAMAZAWA, T., HIROSE, K., KUROSAKI, T. & IINO, M. 1999. Encoding of Ca^{2+} signals by differential expression of IP_3 receptor subtypes. *European Molecular Biology Organisation Journal,* 18**,** 1303-1308.

MIYAZAKI, S., YUZAKI, M., NAKADA, K., SHIRAKAWA, H., NAKANISHI, S., NAKADE, S. & MIKOSHIBA, K. 1992. Block of Ca^{2+} wave and Ca^{2+} oscillation by antibody to inositol 1,4,5-trisphosphate receptor in fertilized hamster eggs. *Science,* 257**,** 251-255.

MOJICA, F. J., DIEZ-VILLASENOR, C., GARCIA-MARTINEZ, J. & SORIA, E. 2005. Intervening sequences of regularly spaced prokaryotic repeats derive from foreign genetic elements. *J Mol Evol,* 60**,** 174-82.

MOJICA, F. J., DIEZ-VILLASENOR, C., SORIA, E. & JUEZ, G. 2000. Biological significance of a family of regularly spaced repeats in the genomes of Archaea, Bacteria and mitochondria. *Mol Microbiol,* 36**,** 244-6.

MONKAWA, T., MIYAWAKI, A., SUGIYAMA, T., YONESHIMA, H., YAMAMOTO-HINO, M., FURUICHI, T., SARUTA, T., HASAGAWA, M. & MIKOSHIBA, K. 1995. Heterotetrameric complex formation of inositol 1,4,5-trisphosphate receptor subunits. *Journal of Biological Chemistry,* 270**,** 14700-14704.

MOSCHELLA, M. C. & MARKS, A. R. 1993. Inositol 1,4,5-trisphosphate receptor expression in cardiac myocytes. *Journal of Cell Biology,* 120**,** 1137-1146.

NAKAMURA, H., BANNAI, H., INOUE, T., MICHIKAWA, T., SANO, M. & MIKOSHIBA, K. 2012. Cooperative and stochastic calcium releases from multiple calcium puff sites generate calcium microdomains in intact Hela cells. *Journal of Biological Chemistry,* 287**,** 24563-24572.

NAKAYAMA, H., BODI, I., MAILLET, M., DESANTIAGO, J., DOMEIER, T. L., MIKOSHIBA, K., LORENZ, J. N., BLATTER, L. A., BERS, D. M. & MOLKENTIN, J. D. 2010. The IP_3 receptor regulates cardiac hypertrophy in response to select stimuli. *Circulation Research,* 107**,** 659-666.

NEWTON, A. C., BOOTMAN, M. D. & SCOTT, J. D. 2016. Second Messengers. *Cold Spring Harb Perspect Biol,* 8.

NEWTON, C. L., MIGNERY, G. A. & SÜDHOF, T. C. 1994. Co-expression in vertebrate tissues and cell lines of multiple inositol 1,4,5-trisphosphate ($InsP_3$) receptors with distinct affinities for $InsP_3$. *Journal of Biological Chemistry,* 269**,** 28613-28619.

NUCIFORA, F. C., SHARP, A. H., MILGRAM, S. L. & ROSS, C. A. 1996. Inositol 1,4,5-trisphosphate receptors in endocrine cells: localization and association in hetero- and homotetramers. *Molecular Biology of the Cell,* 7**,** 949-960.

OGURA, H., MATSUMOTO, M. & MIKOSHIBA, K. 2001. Motor discoordination in mutant mice heterozygous for the type 1 inositol 1,4,5-trisphosphate receptor. *Behav Brain Res,* 122**,** 215-9.

PAKNEJAD, N. & HITE, R. K. 2018. Structural basis for the regulation of inositol trisphosphate receptors by Ca^{2+} and IP_3. *Nat Struct Mol Biol,* 25**,** 660-668.

PANTAZAKA, E. & TAYLOR, C. W. 2011. Differential distribution, clustering and lateral diffusion of subtypes of inositol 1,4,5-trisphosphate receptor. *Journal of Biological Chemistry,* 286**,** 23378-23387.

PAREDES, R. M., ETZLER, J. C., WATTS, L. T., ZHENG, W. & LECHLEITER, J. D. 2008. Chemical calcium indicators. *Methods,* 46**,** 143-151.

PAREKH, A. B. 2008. Ca^{2+} microdomains near plasma membrane Ca^{2+} channels: impact on cell function. *J Physiol,* 586**,** 3043-54.

PARKER, I., CHOI, J. & YAO, Y. 1996. Elementary events of $InsP_3$-induced Ca^{2+} liberation in *Xenopus* oocytes: hot spots, puffs and blips. *Cell Calcium,* 20**,** 105-121.

PARKER, I. & SMITH, I. F. 2010. Recording single-channel activity of inositol trisphosphate receptors in intact cells with a microscope, not a patch clamp. *Journal of General Physiology,* 136**,** 119-127.

PARKER, I. & YAO, Y. 1991. Regenerative release of calcium from functionally discrete subcellular stores by inositol trisphosphate. *Proceedings of The Royal Society of London, Series B,* 246**,** 269-274.

PARKER, I. & YAO, Y. 1996. Ca^{2+} transients associated with openings of inositol trisphosphate-gated channels in *Xenopus* oocytes. *Journal of Physiology,* 491.3**,** 663-668.

PATTERSON, R. L., BOEHNING, D. & SNYDER, S. H. 2004. Inositol 1,4,5-trisphosphate receptors as signal integrators. *Annual Review of Biochemistry,* 73**,** 437-465.

PINTON, P., POZZAN, T. & RIZZUTO, R. 1998. The Golgi apparatus is an inositol 1,4,5-trisphosphate-sensitive Ca^{2+} store, with functional properties distinct from those of the endoplasmic reticulum. *European Molecular Biology Organisation Journal,* 17**,** 5298-5308.

POURCEL, C., SALVIGNOL, G. & VERGNAUD, G. 2005. CRISPR elements in Yersinia pestis acquire new repeats by preferential uptake of bacteriophage

DNA, and provide additional tools for evolutionary studies. *Microbiology,* 151**,** 653-63.

POZZAN, T., RIZZUTO, R., VOLPE, P. & MELDOLESI, J. 1994. Molecular and cellular physiology of intracellular calcium stores. *Physiological Reviews,* 74**,** 595-636.

PRAKRIYA, M. & LEWIS, R. S. 2015. Store-operated calcium channels. *Physiological Reviews,* 95**,** 1383-1436.

PROLE, D. L. & TAYLOR, C. W. 2016. Inositol 1,4,5-trisphosphate receptors and their protein partners as signalling hubs. *Journal of Physiology,* 594**,** 2849-2866.

QI, L. S., LARSON, M. H., GILBERT, L. A., DOUDNA, J. A., WEISSMAN, J. S., ARKIN, A. P. & LIM, W. A. 2013. Repurposing CRISPR as an RNA-Guided Platform for Sequence-Specific Control of Gene Expression. *Cell,* 152**,** 1173-1183.

RAHMAN, T. & TAYLOR, C. W. 2009. Dynamic regulation of IP_3 receptor clustering and activity by IP_3. *Channels,* 3**,** 226-232.

RAHMAN, T. U., SKUPIN, A., FALCKE, M. & TAYLOR, C. W. 2009. Clustering of IP_3 receptors by IP_3 retunes their regulation by IP_3 and Ca^{2+}. *Nature (London),* 458**,** 655-659.

RAMOS-FRANCO, J., FILL, M. & MIGNERY, G. A. 1998a. Isoform-specific function of single inositol 1,4,5-trisphosphate receptor channels. *Biophysical Journal,* 75**,** 834-839.

RAMOS-FRANCO, J., PEREZ, P., CAENEPEEL, S., MIGNERY, G. & FILL, M. 1998b. Distinct calcium regulation patterns of type 1 and type 2 inositol 1,4,5-trisphosphate receptors channels. *Biophysical Journal,* 74**,** A61.

RAN, F. A., HSU, P. D., LIN, C. Y., GOOTENBERG, J. S., KONERMANN, S., TREVINO, A. E., SCOTT, D. A., INOUE, A., MATOBA, S., ZHANG, Y. & ZHANG, F. 2013a. Double nicking by RNA-guided CRISPR Cas9 for enhanced genome editing specificity. *Cell,* 154**,** 1380-9.

RAN, F. A., HSU, P. D., WRIGHT, J., AGARWALA, V., SCOTT, D. A. & ZHANG, F. 2013b. Genome engineering using the CRISPR-Cas9 system. *Nature Protocols,* 8**,** 2281-2308.

RIZZUTO, R., MARCHI, S., BONORA, M., AGUIARI, P., BONONI, A., DE STEFANI, D., GIORGI, C., LEO, S., RIMESSI, A., SIVIERO, R., ZECCHINI, E. & PINTON, P. 2009. Ca^{2+} transfer from the ER to mitochondria: when, how and why. *Biochimica et Biophysica Acta,* 1787**,** 1342-1351.

RODRIGUEZ, A. & LAIO, A. 2014. Machine learning. Clustering by fast search and find of density peaks. *Science,* 344**,** 1492-6.

RONDA, C., MAURY, J., JAKOCIUNAS, T., JACOBSEN, S. A. B., GERMANN, S. M., HARRISON, S. J., BORODINA, I., KEASLING, J. D., JENSEN, M. K. & NIELSEN, A. T. 2015. CrEdit: CRISPR mediated multi-loci gene integration in Saccharomyces cerevisiae. *Microb Cell Fact,* 14.

ROONEY, T. A., SASS, E. J. & THOMAS, A. P. 1990. Agonist-induced cytosolic calcium oscillations originate from a specific locus in single hepatocytes. *Journal of Biological Chemistry,* 265**,** 10792-10796.

ROOS, J., DIGREGORIO, P. J., YEROMIN, A. V., OHLSEN, K., LIOUDYNO, M., ZHANG, S., SAFRINA, O., KOZAK, J. A., WAGNER, S. L., CAHALAN, M. D., VELICELEBI, G. & STAUDERMAN, K. A. 2005. STIM1, an essential and conserved component of store-operated Ca^{2+} channel function. *Journal of Cell Biology,* 169**,** 435-445.

ROSSI, A. M., RILEY, A. M., TOVEY, S. C., RAHMAN, T., DELLIS, O., TAYLOR, E. J. A., VERESOV, V. G., POTTER, B. V. L. & TAYLOR, C. W. 2009. Synthetic partial agonists reveal key steps in IP_3 receptor activation. *Nature Chemical Biology,* 5**,** 631-639.

SACKIN, H. 1995. Stretch-activated ion channels. *Kidney Int,* 48**,** 1134-47.

SALEEM, H., TOVEY, S. C., RAHMAN, T., RILEY, A. M., POTTER, B. V. L. & TAYLOR, C. W. 2012. Stimulation of inositol 1,4,5-trisphosphate (IP_3) receptor subtypes by analogues of IP_3. *PLoS One,* 8**,** e54877.

SALEEM, H., TOVEY, S. C., RILEY, A. M., POTTER, B. V. L. & TAYLOR, C. W. 2013. Stimulation of inositol 1,4,5-trisphosphate (IP_3) receptor subtypes by adenophostin A and its analogues. *PLoS One,* 8**,** e58027.

SANDER, J. D. & JOUNG, J. K. 2014. CRISPR-Cas systems for editing, regulating and targeting genomes. *Nature Biotechnology,* In press.

SANDERSON, M. J., SMITH, I., PARKER, I. & BOOTMAN, M. D. 2014. Fluorescence microscopy. *Cold Spring Harb Protoc,* 2014**,** 65-76.

SAPRANAUSKAS, R., GASIUNAS, G., FREMAUX, C., BARRANGOU, R., HORVATH, P. & SIKSNYS, V. 2011. The Streptococcus thermophilus CRISPR/Cas system provides immunity in Escherichia coli. *Nucleic Acids Res,* 39**,** 9275-82.

SASSE, P., ZHANG, J., CLEEMANN, L., MORAD, M., HESCHELER, J. & FLEISCHMANN, B. K. 2007. Intracellular Ca^{2+} oscillations, a potential

pacemaking mechanism in early embryonic heart cells. *J Gen Physiol,* 130**,** 133-44.

SCHINDELIN, J., ARGANDA-CARRERAS, I., FRISE, E., KAYNIG, V., LONGAIR, M., PIETZSCH, T., PREIBISCH, S., RUEDEN, C., SAALFELD, S., SCHMID, B., TINEVEZ, J. Y., WHITE, D. J., HARTENSTEIN, V., ELICEIRI, K., TOMANCAK, P. & CARDONA, A. 2012. Fiji: an open-source platform for biological-image analysis. *Nature Methods,* 9**,** 676-682.

SEO, M.-D., VELAMAKANNI, S., ISHIYAMA, N., STATHOPULOS, P. B., ROSSI, A. M., KHAN, S. A., DALE, P., LI, C., AMES, J. B., IKURA, M. & TAYLOR, C. W. 2012. Structural and functional conservation of key domains in $InsP_3$ and ryanodine receptors. *Nature,* 483**,** 108-112.

SHARP, A. H., NUCIFORA, F. C., BLONDEL, O., SHEPPARD, C. A., ZHANG, C., SNYDER, S. H., RUSSELL, J. T., RYUGO, D. K. & ROSS, C. A. 1999. Differential cellular expression of isoforms of inositol 1,4,5-trisphosphate receptors in neurons and glia in brain. *Journal of Comparative Neurology,* 406**,** 207-220.

SHUAI, J. & PARKER, I. 2005. Optical single-channel recording by imaging Ca^{2+} flux through individual ion channels: theoretical considerations and limits to resolution. *Cell Calcium,* 37**,** 283-299.

SIMPSON, P. B., MEHOTRA, S., LANGE, G. D. & RUSSELL, J. T. 1997. High density distribution of endoplasmic reticulum proteins and mitochondria at specialised Ca^{2+} release sites in oligodendrocyte. *Journal of Biological Chemistry,* 272**,** 22654-22661.

SLAYMAKER, I. M., GAO, L., ZETSCHE, B., SCOTT, D. A., YAN, W. X. & ZHANG, F. 2016. Rationally engineered Cas9 nucleases with improved specificity. *Science,* 351**,** 84-8.

SMITH, I. F. & PARKER, I. 2009. Imaging the quantal substructure of single IP_3R channel activity during Ca^{2+} puffs in intact mammalian cells. *Proceedings of the National Academy of Sciences USA,* 106**,** 6404-6409.

SMITH, I. F., WILTGEN, S. M. & PARKER, I. 2009a. Localization of puff sites adjacent to the plasma membrane: functional and spatial characterization of Ca^{2+} signaling in SH-SY5Y cells utilizing membrane-permeant caged IP_3. *Cell Calcium,* 45**,** 65-76.

SMITH, I. F., WILTGEN, S. M., SHUAI, J. & PARKER, I. 2009b. Ca^{2+} puffs originate from preestablished stable clusters of inositol trisphosphate receptors. *Science Signaling,* 2**,** ra77.

SOLOVYOVA, N. & VERKHRATSKY, A. 2002. Monitoring of free calcium in the neuronal endoplasmic reticulum: an overview of modern approaches. *J Neurosci Methods,* 122**,** 1-12.

STEELE, E. M. & STEELE, D. S. 2014. Automated detection and analysis of Ca^{2+} sparks in x-y image stacks using a thresholding algorithm implemented within the open-source image analysis platform ImageJ. *Biophysical Journal,* 106**,** 566-576.

STERNBERG, S. H., REDDING, S., JINEK, M., GREENE, E. C. & DOUDNA, J. A. 2014. DNA interrogation by the CRISPR RNA-guided endonuclease Cas9. *Nature,* 507**,** 62-7.

STOJILKOVIC, S. S., KUKULJAN, M., IIDA, T., ROJAS, E. & CATT, K. J. 1992. Integration of Cytoplasmic Calcium and Membrane-Potential Oscillations Maintains Calcium Signaling in Pituitary Gonadotrophs. *Proceedings of the National Academy of Sciences of the United States of America,* 89**,** 4081-4085.

STREET, V. A., BOSMA, M. M., DEMAS, V. P., REGAN, M. R., LIN, D. D., ROBINSON, L. C., AGNEW, W. S. & TEMPEL, B. L. 1997. The type 1 inositol 1,4,5-trisphosphate receptor gene is altered in the *opisthotonos* mouse. *Journal of Neuroscience,* 17**,** 635-645.

STRIESSNIG, J., PINGGERA, A., KAUR, G., BOCK, G. & TULUC, P. 2014. L-type Ca^{2+} channels in heart and brain. *Wiley Interdiscip Rev Membr Transp Signal,* 3**,** 15-38.

SÜDHOF, T. C., NEWTON, C. L., ARCHER, B. T., USHKARYOV, Y. A. & MIGNERY, G. A. 1991. Structure of a novel $InsP_3$ receptor. *European Molecular Biology Organisation Journal,* 10**,** 3199-3206.

SUGAWARA, H., KUROSAKI, M., TAKATA, M. & KUROSAKI, T. 1997. Genetic evidence for involvement of type 1, type 2 and type 3 inositol 1,4,5-trisphosphate receptors in signal transduction through the B-cell antigen receptor. *EMBO J,* 16**,** 3078-3088.

SUGAWARA, T., HISATSUNE, C., LE, T. D., HASHIKAWA, T., HIRONO, M., HATTORI, M., NAGAO, S. & MIKOSHIBA, K. 2013. Type 1 inositol trisphosphate receptor regulates cerebellar circuits by maintaining the spine morphology of purkinje cells in adult mice. *J Neurosci,* 33**,** 12186-96.

SUN, X.-P., CALLAMARAS, N., MARCHANT, J. S. & PARKER, I. 1998. A continuum of InsP_3-mediated elementary Ca^{2+} signalling events in *Xenopus* oocytes. *Journal of Physiology,* 509**,** 67-80.

SWATTON, J. E., MORRIS, S. A., CARDY, T. J. A. & TAYLOR, C. W. 1999. Type 3 inositol trisphosphate receptors in RINm5F cells are biphasically

regulated by cytosolic Ca^{2+} and mediate quantal Ca^{2+} mobilization. *Biochemical Journal,* 344**,** 55-60.

SWATTON, J. E. & TAYLOR, C. W. 2002. Fast biphasic regulation of type 3 inositol trisphosphate receptors by cytosolic calcium. *Journal of Biological Chemistry,* 277**,** 17571-17579.

SWILLENS, S., DUPONT, G., COMBETTES, L. & CHAMPEIL, P. 1999. From calcium blips to calcium puffs: Theoretical analysis of the requirements for interchannel communication. *Proceedings of the National Academy of Sciences USA,* 96**,** 13750-13755.

TAKEI, K., SHIN, R. M., INOUE, T., KATO, K. & MIKOSHIBA, K. 1998. Regulation of nerve growth mediated by inositol 1,4,5-trisphosphate receptors in growth cones. *Science,* 282**,** 1705-1708.

TAKESHIMA, H., KOMAZAKI, S., HIROSE, K., NISHI, M., NODA, T. & IINO, M. 1998. Embryonic lethality and abnormal cardiac myocytes in mice lacking ryanodine receptor type 2. *EMBO J,* 17**,** 3309-16.

TATEISHI, Y., HATTORI, M., NAKAYAMA, T., IWAI, M., BANNAI, H., NAKAMURA, T., MICHIKAWA, T., INOUE, T. & MIKOSHIBA, K. 2005. Cluster formation of inositol 1,4,5-trisphosphate receptor requires its transition to open state. *J Biol Chem,* 280**,** 6816-22.

TAYLOR, C. W., DA FONSECA, P. C. A. & MORRIS, E. P. 2004. IP_3 receptors: the search for structure. *Trends in Biochemical Sciences,* 29**,** 210-219.

TAYLOR, C. W., GENAZZANI, A. A. & MORRIS, S. A. 1999. Expression of inositol trisphosphate receptors. *Cell Calcium,* 26**,** 237-251.

TAYLOR, C. W. & LAUDE, A. J. 2002. IP_3 receptors and their regulation by calmodulin and cytosolic Ca^{2+}. *Cell Calcium,* 32**,** 321-334.

TAYLOR, C. W. & TOVEY, S. C. 2012. IP_3 receptors: toward understanding their activation. *Cold Spring Harbor Perspectives in Biology,* 2**,** a004010.

THILLAIAPPAN, N. B., CHAVDA, A. P., TOVEY, S. C., PROLE, D. L. & TAYLOR, C. W. 2017. Ca^{2+} signals initiate at immobile IP_3 receptors adjacent to ER-plasma membrane junctions. *Nature Communications,* 8**,** 1505.

THOMAS, D., LIPP, P., BERRIDGE, M. J. & BOOTMAN, M. D. 1998. Hormone-evoked elementary Ca^{2+} signals are not stereotypic, but reflect activation of different size channel clusters and variable recruitment of channels within a cluster. *Journal of Biological Chemistry,* 273**,** 27130-27136.

THOMPSON, J. L. & SHUTTLEWORTH, T. J. 2013. Exploring the unique features of the ARC channel, a Store-independent Orai channel. *Channels,* 7**,** 364-373.

THURLEY, K., SMITH, I. F., TOVEY, S. C., TAYLOR, C. W., PARKER, I. & FALCKE, M. 2011. Timescales of IP_3-evoked Ca^{2+} spikes emerge from Ca^{2+} puffs only at the cellular level. *Biophysical Journal,* 101**,** 2638-2644.

THURTLE-SCHMIDT, D. M. & LO, T. W. 2018. Molecular biology at the cutting edge: A review on CRISPR/CAS9 gene editing for undergraduates. *Biochemistry and Molecular Biology Education,* 46**,** 195-205.

TONG, X., SHIGETOMI, E., LOOGER, L. L. & KHAKH, B. S. 2012. Genetically encoded calcium indicators and astrocyte calcium microdomains. *Neuroscientist,* 19**,** 274-291.

TOVEY, S. C., DEDOS, S. G., TAYLOR, E. J. A., CHURCH, J. E. & TAYLOR, C. W. 2008. Selective coupling of type 6 adenylyl cyclase with type 2 IP_3 receptors mediates a direct sensitization of IP_3 receptors by cAMP. *Journal of Cell Biology,* 183**,** 297-311.

TOVEY, S. C., SUN, Y. & TAYLOR, C. W. 2006. Rapid functional assays of intracellular Ca^{2+} channels. *Nature Protocols,* 1**,** 259-263.

TSIEN, R. Y. 1980. New calcium indicators and buffers with high selectivity against magnesium and protons: design, synthesis, and properties of prototype structures. *Biochemistry,* 19**,** 2396-2404.

TU, H., WANG, Z. & BEZPROZVANNY, I. 2005. Modulation of mammalian inositol 1,4,5-trisphosphate receptor isoforms by calcium: a role of calcium sensor region. *Biophysical Journal,* 88**,** 1056-1069.

UCHIDA, K., ARAMAKI, M., NAKAZAWA, M., YAMAGISHI, C., MAKINO, S., FUKUDA, K., NAKAMURA, T., TAKAHASHI, T., MIKOSHIBA, K. & YAMAGISHI, H. 2010. Gene knock-outs of inositol 1,4,5-trisphosphate receptors types 1 and 2 result in perturbation of cardiogenesis. *PLoS One,* 5**,** e12500.

UCHIDA, K., MIYAUCHI, H., FURUICHI, T., MICHIKAWA, T. & MIKOSHIBA, K. 2003. Critical regions for activation gating of the inositol 1,4,5-trisphosphate receptor. *Journal of Biological Chemistry,* 278**,** 16551-16560.

ULLAH, G., PARKER, I., MAK, D. O. & PEARSON, J. E. 2012. Multi-scale data-driven modeling and observation of calcium puffs. *Cell Calcium,* 52**,** 152-60.

URNOV, F. D., REBAR, E. J., HOLMES, M. C., ZHANG, H. S. & GREGORY, P. D. 2010. Genome editing with engineered zinc finger nucleases. *Nat Rev Genet,* 11**,** 636-46.

VAIS, H., FOSKETT, J. K. & MAK, D. O. 2010. Unitary Ca^{2+} current through recombinant type 3 $InsP_3$ receptor channels under physiological ionic conditions. *Journal of General Physiology,* 136**,** 687-700.

VAN DER PLOEG, J. R. 2009. Analysis of CRISPR in Streptococcus mutans suggests frequent occurrence of acquired immunity against infection by M102-like bacteriophages. *Microbiology,* 155**,** 1966-76.

VERMASSEN, E., PARYS, J. B. & MAUGER, J.-P. 2004. Subcellular distribution of the inositol 1,4,5-trisphosphate receptors: functional relevance and molecular determinants. *Biology of the Cell,* 96**,** 3-17.

WAGNER, L. E., 2ND & YULE, D. I. 2012. Differential regulation of the $InsP_3$ receptor type-1 and -2 single channel properties by $InsP_3$, Ca^{2+} and ATP. *Journal of Physiology,* 590**,** 3245-3259.

WANG, X., WANG, Y., ZHOU, Y., HENDRON, E., MANCARELLA, S., ANDRAKE, M. D., ROTHBERG, B. S., SOBOLOFF, J. & GILL, D. L. 2014. Distinct Orai-coupling domains in STIM1 and STIM2 define the Orai-activating site. *Nature Communications,* 5**,** 3183.

WEI, C., WANG, X., CHEN, M., OUYANG, K., SONG, L. S. & CHENG, H. 2009. Calcium flickers steer cell migration. *Nature,* 457**,** 901-5.

WILLIAMS, A. J., WEST, D. J. & SITSAPESAN, R. 2001. Light at the end of the Ca^{2+}-release channel tunnel: structures and mechanisms involved in ion translocation in ryanodine receptor channels. *Quarterly Reviews of Biophysics,* 34**,** 61-104.

WILSON, B. S., PFEIFFER, J. R., SMITH, A. J., OLIVER, J. M., OBERDORF, J. A. & WOJCIKIEWICZ, R. J. H. 1998. Calcium-dependent clustering of inositol 1,4,5-trisphosphate receptors. *Molecular Biology of the Cell,* 9**,** 1465-1478.

WILTGEN, S. M., DICKINSON, G. D., SWAMINATHAN, D. & PARKER, I. 2014. Termination of calcium puffs and coupled closings of inositol trisphosphate receptor channels. *Cell Calcium,* 56**,** 157-168.

WILTGEN, S. M., SMITH, I. F. & PARKER, I. 2010. Superresolution localization of single functional IP_3R channels utilizing Ca^{2+} flux as a readout. *Biophysical Journal,* 99**,** 437-446.

WOJCIKIEWICZ, R. J. H. 1995. Type I, II and III inositol 1,4,5-trisphosphate receptors are unequally susceptible to down-regulation and are expressed in markedly different proportions in different cell types. *Journal of Biological Chemistry,* 270**,** 11678-11683.

WOJCIKIEWICZ, R. J. H. & HE, Y. 1995. Type I, II and III inositol 1,4,5-trisphosphate receptor co-immunoprecipitation as evidence for the existence heterotetrameric receptor complexes. *Biochemical and Biophysical Research Communications,* 213**,** 334-341.

WRIGHT, D. A., LI, T., YANG, B. & SPALDING, M. H. 2014. TALEN-mediated genome editing: prospects and perspectives. *Biochemical Journal,* 462**,** 15-24.

WU, X., ZHANG, T., BOSSUYT, J., LI, X., MCKINSEY, T. A., DEDMAN, J. R., OLSON, E. N., CHEN, J., BROWN, J. H. & BERS, D. M. 2006. Local $InsP_3$-dependent perinuclear Ca^{2+} signaling in cardiac myocyte excitation-transcription coupling. *Journal of Clinical Investigation,* 116**,** 675-682.

YAO, Y., CHOI, J. & PARKER, I. 1995. Quantal puffs of intracellular Ca^{2+} evoked by inositol trisphosphate in *Xenopus* oocytes. *Journal of Physiology,* 482**,** 533-553.

YOO, S. H. 2011. Role of secretory granules in inositol 1,4,5-trisphosphate-dependent Ca^{2+} signaling: From phytoplankton to mammals. *Cell Calcium,* 50**,** 175-183.

YOSHIKAWA, F., IWASAKI, H., MICHIKAWA, T., FURUICHI, T. & MIKOSHIBA, K. 1999. Trypsinized cerebellar inositol 1,4,5-trisphosphate receptor. Structural and functional coupling of cleaved ligand binding and channel domains. *Journal of Biological Chemistry,* 274**,** 316-327.

ZETSCHE, B., GOOTENBERG, J. S., ABUDAYYEH, O. O., SLAYMAKER, I. M., MAKAROVA, K. S., ESSLETZBICHLER, P., VOLZ, S. E., JOUNG, J., VAN DER OOST, J., REGEV, A., KOONIN, E. V. & ZHANG, F. 2015. Cpf1 is a single RNA-guided endonuclease of a class 2 CRISPR-Cas system. *Cell,* 163**,** 759-71.

ZWEIFACH, A. & LEWIS, R. S. 1995. Rapid inactivation of depletion-activated calcium current (I_{CRAC}) due to local calcium feedback. *Journal of General Physiology,* 105**,** 209-226.